FH AACHEN
UNIVERSITY OF APPLIED SCIENCES

universiteit hasselt
KNOWLEDGE IN ACTION

2014 | Faculty of Sciences

DOCTORAL DISSERTATION

Multi-parameter physico-chemical sensing principles for biogas-process monitoring

Doctoral dissertation submitted to obtain the degree of doctor of Science, to be defended by:

Christina Huck

Promoter: Prof. Dr Patrick Wagner | UHasselt
Co-promoter: Prof. Dr-Ing Michael J. Schöning | FH Aachen

D/2014/2451/37

universiteit hasselt | imec
IMO - IMOMEC
INSTITUUT VOOR MATERIAALONDERZOEK

Jury

Chairman:	Prof. Dr. K. Coninx Hasselt University Expertise centre for Digital Media (EDM)
Promoter:	Prof. Dr. P. Wagner Hasselt University Institute for Materials Research (IMO)
Co-promoter:	Prof. Dr.-Ing. M. J. Schöning FH Aachen Institute of Nano- and Biotechnologies (INB)
Members of the jury:	Prof. Dr. C. Bartic K.U. Leuven Laboratory of Solid State Physics and Magnetism
	Prof. Dr. H.-G. Boyen Hasselt University Institute for Materials Research (IMO)
	Prof. Dr. A. Poghossian FH Aachen Institute of Nano- and Biotechnologies (INB)
	Prof. Dr. ir. R. Thoelen Hasselt University Institute for Materials Research (IMO)
	Dr. T. Wagner FH Aachen Institute of Nano- and Biotechnologies (INB)

Abstract

Renewable energies such as biogas are gaining steadily in importance. The use of methane gas obtained from fermentation processes in biogas plants takes on an added interest for energy supply. Overloading such biogas plants with excessive biomass may have considerable economic consequences including inactivation of the biomass resulting in a cost-intensive restart. On the other hand, adding too little biomass to the biogas reactor results in the generation of less electricity and heat and revenue is lost. All plant operators have therefore a crucial interest in running their biogas plant as efficiently as possible. To do this, reliable online analysis is needed, since better monitoring and control can improve process stability and enhance process performance for higher yield in terms of energy. The fundamentals of the biogas production process with the focus on monitoring and control are given in **Chapter 1**.

The present thesis focuses on the design and characterization of miniaturized multi-parameter sensor chips for applications in biogas process monitoring. Within the frame of this work, sensors for the detection of five physico-chemical quantities were developed employing different transducer principles. These quantities included the dissolved hydrogen concentration, the metabolic activity, the electrolyte conductivity, the pH value and the temperature. General information of the sensing principles of the sensors used in this work are described in **Chapter 2**.

An one-chip combined amperometric/field-effect sensor for the detection of the dissolved hydrogen concentration was developed. Two transduction principles were integrated at the microscale, enabling new electrochemical detection opportunities. Special emphasis was devoted to the independent functionality of the two transducers proving the indirect measurement of dissolved hydrogen (see **Chapter 3**).

A cell-based sensor for monitoring the metabolic activity and thus, the vitality of relevant organisms was utilized. Metabolic responses of the model bacterium *Escherichia coli* in suspension as well as immobilized by gel entrapment on a capacitive field-effect structure were studied to pulses of glucose and acetate. Correlations between cell number, glucose and acetate concentration, acidification rate, and time of the acidification period due to the consumption of the carbon source were examined (see **Chapter 4**).

An extensive study of the high-k material barium strontium titanate (BST) as passivation and protection layer of a miniaturized electrolyte-conductivity sensor, which is referred to a capacitively coupled contactless conductivity detection (C^4D) sensor in the following, was examined. For better understanding, an equivalent circuit model of the C^4D sensor chip was developed and discussed. For comparison, contact-mode electrolyte-conductivity (EC) sensors were addition-

ally fabricated. Both sensors (EC and C^4D) were characterized in electrolyte solutions with various conductivities using two- and four-electrode operation modes to study the influence of the protective BST layer. The obtained results clearly demonstrate the benefits of the use of the BST-based C^4D sensor in a four-electrode configuration for contactless conductivity measurements: A linear dependence between the measured conductance and the electrolyte conductivity was obtained in a wide range of electrolyte conductivity from 0.3 mS/cm to 50 mS/cm; in addition, no negative influence of the protective BST layer on the conductivity sensor performance was identified (see **Chapter 5**).

A multi-parameter sensor chip using BST as multi-purpose material was developed to monitor electrolyte conductivity, pH value and temperature in buffer solutions and biogas slurry. This sensor united the capacitively coupled four-electrode electrolyte conductivity sensor with a capacitive field-effect pH sensor and a thin-film Pt-temperature sensor. Here, BST was utilized due to its multi-functional properties as final outermost coating layer of the processed multi-parameter sensor chip. It served as passivation and protection layer as well as pH-sensitive transducer material at the same time. Multi-parameter characterizations of the sensor chip in buffer solutions with different pH value and electrolyte conductivity were conducted. Finally, the sensor chip was exemplarily examined in biogas slurry to evaluate the sensor and the suitability of BST as multi-functional material under harsh environmental conditions. The experiments demonstrated that all three sensor parts exhibited a very stable sensor signal (see **Chapter 6**).

Chapter 7 closes the current thesis with a final summary of the results, new experiences gained throughout this work and an outlook including potential ongoing strategies.

Nederlandse samenvatting

Hernieuwbare energieën zoals biogas staan in toenemende mate in de openbare belangstelling. Hierbij gaat het in het bijzonder om methaangas dat door fermentatieprocessen in biogasreactoren ontstaat en een hoge energetische waarde bezit. Er zijn echter een aantal randvoorwaarden in acht te nemen zoals het feit dat een overlading van bioreactoren met biomassa het proces onbeheersbaar maakt zodat een prijzige heropstart nodig wordt. Anderzijds leidt een te geringe aanvoer van biomassa tot een verminderde opbrengst aan warmte- en elektrische energie wat uit economisch oogpunt evenmin wenselijk is. Het uitbaten van dergelijke reactoren is daarom erbij gebaat om de processen gecontroleerd en zo efficiënt mogelijk te doen aflopen. Hieruit ontstaat de noodzaak om bio-processen op een betrouwbare manier "online" te monitoren zodanig dat de processen stabiel kunnen verlopen en een zo hoog mogelijk energierendement

opleveren. De basisprincipes van de biogasproductie en het monitoren van de onderliggende processen worden samengevat in **Hoofdstuk 1**.

Dit doctoraatswerk richt zich op het ontwerp en de karakterisering van geminiaturiseerde multiparameter sensorchips voor toepassingen in verband met de monitoring van biogas-processen. In het kader van dit onderzoek werden dan ook sensoren ontwikkeld voor de bepaling van vijf relevante, fysicochemische parameters zijnde de concentratie van waterstof in oplossing, de metabolische activiteit, de elektrolytische geleidbaarheid, de pH-waarde en de temperatuur. Hierbij kwamen verschillende meetprincipes ("transducers") aan te pas, al dan geïntegreerd op ene sensorchip voor de gelijktijdige bepaling van verschillende analytische grootheden. De fysicochemische aspecten van deze meetprincipes worden in **Hoofdstuk 2** uiteen gezet.

Als een eerste voorbeeld voor deze aanpak werd een gecombineerde sensor ontwikkeld voor de kwantitatieve bepaling van opgeloste waterstofconcentraties door middel van amperometrie en elektrische veldeffecten. De twee detectieprincipes werden hierbij op microschaal geïntegreerd wat nieuwe elektrochemische analysemethoden mogelijk maakt. Een speciale uitdaging was de correcte, onafhankelijke werking van de twee transducer-principes en finaal werden daadwerkelijk concentraties van opgeloste waterstof bepaald. Deze resultaten zijn beschreven in **Hoofdstuk 3**.

Met het oog op de metabolische activiteit en de vitale parameters van cellen in biogas-reactoren werd een cel-gebaseerde sensor ontwikkeld met *Escherichia coli* cellen als modelorganisme. De *E. coli* cellen werden hierbij met en capacitieve veld-effect sensor onderzocht waarbij de cellen zich ofwel in suspensie bevonden ofwel door middel van een gel rechtstreeks op de sensorstructuur werden geïmmobiliseerd. De metabolische response werd geanalyseerd na toediening van geijkte hoeveelheden van de nutriënten glucose en acetaat. Hiermee werden correlaties verkregen tussen het aantal cellen, de glucose- en acetaat-concentraties, de snelheid van verzuring en de blootstellingsduur, zie **Hoofdstuk 4**.

Vervolgens werd een nieuw, geminiaturiseerd sensortype ontwikkeld voor de bepaling van de elektrolytische geleidbaarheid: Bij deze sensor dient het "high-k" materiaal barium strontium titanaat (BST) als passivering en beschermende laag op de sensorchip en het werkingsprincipe kan omschreven worden als "C^4D sensor". Dit staat voor "capacitively coupled contactless conductivity detection" ofwel de "capacitieve, contactvrije geleidbaarheidsmeting". Voor de nauwkeurige analyse van het werkingsmechanisme werd een elektronisch-equivalent model opgesteld. Voorts werden de C^4D sensoren uitgebreid vergeleken met geleidbaarheids-sensoren met een rechtstreeks contact tussen de elektrolyt en de sensorchip (electrolyte-conductivity "EC" sensors).

Beide sensortypes (EC en C^4D) werden in elektrolytoplossingen met verschil-

lende geleidbaarheidswaarden gekarakteriseerd en, door metingen in twee-elektroden- en vier-elektroden configuratie, werd de invloed van de beschermende BST lagen in detail geëvalueerd. De behaalde resultaten tonen duidelijk de voordelen van de BST-gebaseerde C^4D sensor voor contactvrije geleidbaarheidsmetingen aan: Enerzijds bestaat er een lineair verband tussen de gemeten geleidbaarheidswaarden en de nominale geleidbaarheid van de elektrolyten in een breed geleidbaarheidsgebied van 0.3 tot 50 mS/cm. Anderzijds is er geen enkel aantoonbaar effect dat de beschermende BST-laag nadelig zou zijn voor de gevoeligheid en precisie van de ontwikkelde sensor. Deze bevindingen worden in detail uitgelegd in **Hoofdstuk 5**.

Hoofdstuk 6 beschrijft de integratie van de ontwikkelde technologieën in een multiparameter sensorchip om de toestandsvariabelen geleidbaarheid, pH-waarde en temperatuur simultaan te meten. BST deed hierbij dienst als een multifunctioneel materiaal. De sensorchip zelf omvatte een capacitief gekoppelde vier-elektroden geleidbaarheidssensor, een capacitieve veldeffect pH-sensor, en een platina-temperatuur-sensor in dunschichttechnologie. Het BST zelf vormde de bovenste, beschermende laag op de sensorchip en diende tegelijkertijd als een pH-sensitief transducermateriaal. Deze multiparameter chip werd in bufferoplossingen gekarakteriseerd voor een reeks van verschillende pH- en geleidbaarheidswaarden. Tenslotte werd de werking van de sensorchip rechtstreeks gevalideerd in vloeistoffen uit biogasreactoren om zodoende ook uitsluitsel te verkrijgen over de stabiliteit van de BST-deklagen in een scheikundig agressieve omgeving. De experimenten toonden twijfelvrij aan dat de drie deelsensoren van de chip stabiele uitputsignalen geven en daarmee is inderdaad voldaan aan alle voorwaarden voor monitoring-toepassingen in fermentatie-reactoren.

De thesis wordt afgerond met **Hoofdstuk 7** dat een afsluitende samenvatting van de behaalde resultaten geeft samen met nieuwe inzichten op de basis van het voorliggende werk en mogelijke strategieën beschrijft met het oog op toepassingen in de praktijk.

Contents

1 Introduction

The global energy demand is growing rapidly, and about 86% of this demand is currently met by fossil fuels [1]. At the same time, concentrations of greenhouse gasses in the atmosphere are rising increasingly. The most important contributor are fossil fuel-derived carbon dioxide emissions, which must be reduced to minimize global warming [2]. An important challenge is the security of energy supply due to the fact that conventional oil and gas reserves are limited and are concentrated in politically unstable regions [3]. In this context, biogas from waste products has risen attention and will play a vital role in future [3].

In principle, any material of organic origin counts as biomass. Not just plants and animals but also animal excrements or plant components such as straw, paper and cellulose, abattoir waste, organic waste from households and industry can be used as biomass. Biogas forms in any place where organic matter decomposes in a moist environment without light and air [4]. Its potential for utilization and commercialization is outstanding for the production of electricity and heat from its direct combustion in co-generation plants and for the production of biomethane as a natural gas substitute. When produced and used on a sustainable basis, it is a carbon-neutral carrier and can make a large contribution to reducing greenhouse gas emissions [3]. Among the renewables (e.g., wind and solar energy) biogas is arguably the most versatile energy due to its determinate energy value and ease of storage. Hence, potential utilization is significantly independent of factors such as geographical location and season [5].

1.1 The biogas production process

Anaerobic digestion is a biological process where organic matter such as energy crops, organic residues and manure is converted by subsequent oxidations and reductions mainly to carbon dioxide and methane. Minor quantities of nitrogen, hydrogen, ammonia and hydrogen sulfide (usually less than 1% of the total gas volume) are also generated [6]. The individual degradation steps are carried out by different consortia of microorganisms, which partly stand in syntrophic interrelation (complex interaction) and place different requirements on the environment [7].

Figure 1.1 shows the degradation pathway in anaerobic digestion of organic matter. The important processes in anaerobic digestion are hydrolysis, fermentation, acetogenesis and methanogenesis. While hydrolysis is subject to the

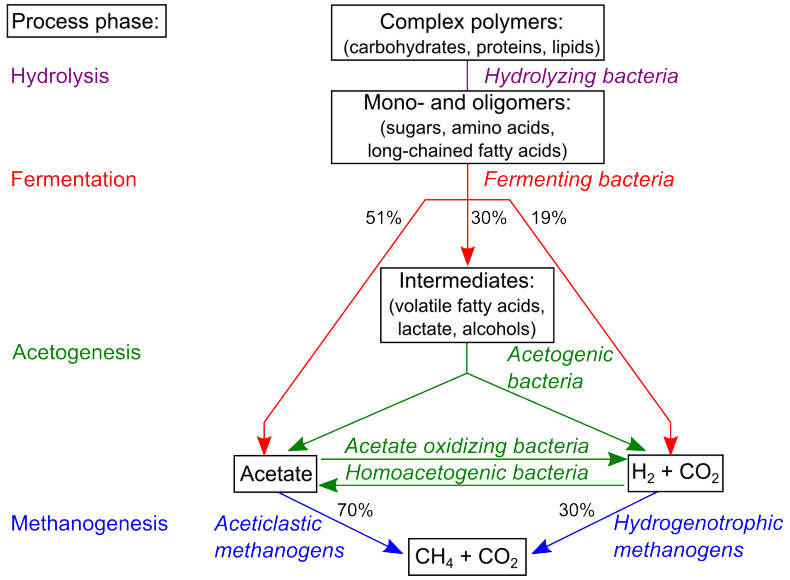

Figure 1.1: Degradation pathways of the biogas production process (adapted from [6, 8, 9]).

fermentation process, acetogenesis, and methanogenesis are linked to each other. Three major groups of microorganisms[1] have been identified comprising different functions in the overall degradation process:

1. *Hydrolyzing* and *fermenting bacteria*[2] are responsible for the initial attack on polymers and monomers found in the waste material. They produce mainly acetate and hydrogen and varying amounts of volatile fatty acids (VFA) such as propionate and butyrate.

2. *Acetogenic bacteria*[3] convert the more reduced intermediate products such as alcohols and volatile fatty acids (VFA) into acetate and hydrogen.

3. Two groups of *methanogens*[4] produce methane from acetate or hydrogen, respectively [6].

[1] A brief overview of the main microorganisms participating in the process of degradation can be found in [4].

[2] The genera *Clostridium*, *Paenibacillus* and *Ruminococcus* appear in all phases of the fermentation process but are dominant in the fermentation phase.

[3] The genera *Desulfovibrio*, *Aminobacterium* and *Acidaminococcus* are examples for *acetogenic bacteria*.

[4] Active methanogens appear in the second phase of fermentation, but the number of methanogens increases in the last phase. The main genera are *Methanobacterium*, *Methanosaeta* and *Methanosarcina*.

In well-operating anaerobic digesters, the major part of the carbon flow occurs between the *fermenting microorganisms* and the *methanogens*. Only 30% of the carbon is transformed into intermediate products before these are metabolized to methane and carbon dioxide [10].

A balanced anaerobic digestion process demands that the products of the *hydrolyzing* and *fermenting bacteria* responsible for the production of acetate and hydrogen are simultaneously used by the two groups of *methanogens* responsible for the production of methane and carbon dioxide. *Hydrolyzing* and *fermenting bacteria* can survive without the presence of *methanogens*. Under these conditions, *hydrolyzing* and *fermenting* bacteria will form an increased amount of the more reduced intermediate products. The *acetogenic bacteria*, however, rely on the activity of *methanogens* to make their metabolism thermodynamically favorable. This will be explained in further detail in Section 1.2.1.

1.2 Monitoring and control of the biogas production process

The anaerobic digestion process is influenced by numerous microbiological, chemical and physical quantities which makes it due to its complexity a valid subject for control and optimization. Process control requires therefore the acquisition of a variety of measures to gain information on the different stages. A reliable operation of biogas plants can only be achieved if the entire process chain beginning from the fed substrate up to the products is controlled and monitored by suitable measurement devices. Due to the diversity of used substrates and their mixtures process monitoring is difficult. On the other hand, process disturbances and process failures can have plenty of causes eventually ending up to a digester break down. Process disturbances known to occur can be due to overload or lack of macro- and micro-nutrients as well as entry of inhibitors (e.g., antibiotics, heavy metals, high ammonia concentration). As depicted in Fig. 1.2, several parameters from the gas phase and liquid phase have been proposed to characterize the anaerobic digestion process. These include among others gas production and gas composition [11], chemical (e.g., pH, alkalinity, VFA, H_2) [12–15] and physical quantities (e.g., temperature and pressure), microbial communities (populations, diversity) [16] as well as metabolic activities [9, 17]. In considering of the most important parameters for process control of biogas digesters a distinction can be made between early warning parameters and state variables [18]. The parameters highlighted in red (see Fig. 1.2) will be discussed in more detail in the following sections, since these parameters are the measurands of the designed and developed miniaturized solid-state sensors of the present thesis.

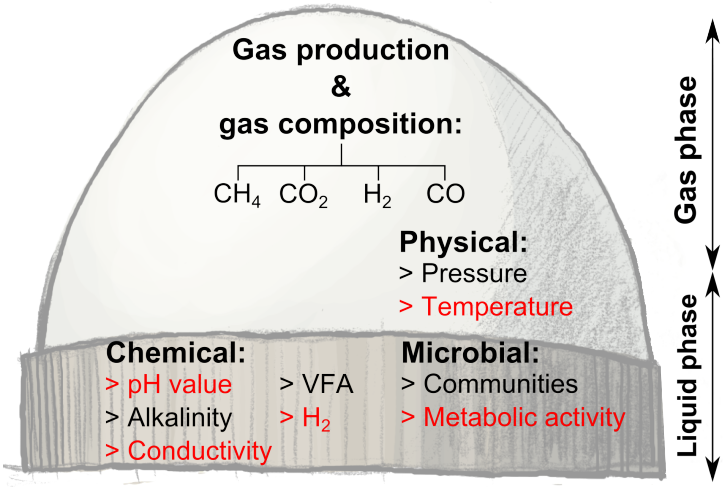

Figure 1.2: Monitoring parameters of the biogas production process from liquid phase and gas phase. The parameters highlighted in red are the measurands of the designed and developed solid-state sensors of the present thesis.

1.2.1 Early warning parameters

To detect changes in the process flow before a drop in performance or digester breakdown happens, early warning parameters are required. Therefore, these indicators seek to improve effectiveness and economic efficiency of the biogas process.

Hydrogen and dissolved hydrogen The concentration of hydrogen affects the thermodynamics and degradation pathways of the anaerobic digestion process. As depicted in Fig. 1.1, hydrogen is a significant intermediate compound for methanogenesis and electron carrier in the digestion process [19]. It is produced during fermentation of carbohydrates and other substrates by the *fermenting bacteria* and in the subsequent degradation of intermediate products such as propionate and butyrate to acetate by the *acetogenic bacteria*. On the contrary, hydrogen is consumed by *hydrogenotrophic methanogens* to reduce carbon dioxide to methane gas [20].

In properly operating anaerobic digesters the hydrogen concentration is normally low. An imbalance between the *acetogenic bacteria* and *hydrogenotrophic methanogens* can, however, lead to hydrogen accumulation. A build-up of hydrogen partial pressure above a critical concentration higher than 10 Pa [21] or a dissolved hydrogen concentration higher than 40 nM [22] has been reported as initial stage of digester overloading. Higher hydrogen concentrations will

direct the electron flow from methane production resulting in the formation of VFAs such as butyrate, propionate, lactate, or ethanol [23]. These more reduced products cannot be used directly as substrates in methanogenic fermentation. A further degradation step by the *acetogenic bacteria* is hydrogen-dependent and will be inhibited at elevated hydrogen concentrations. An increased hydrogen concentration will also favor the production of acetate from hydrogen by the *homoacetogenic bacteria* [21]. If hydrogen production exceeds the maximum ability of the methanogenic biomass to degrade hydrogen, there will be a rapid and large hydrogen consumption prior to digester failures. Thus, hydrogen is a key factor in the intricate balance between microbial species involved in the multi-step degradation during anaerobic digestion and has been reported to present one of the most important parameters for biogas process monitoring [12, 23–25].

Intensive studies of hydrogen concentrations in both the gaseous and liquid phase have found that the hydrogen concentration in the headspace does not correspond to the actual concentration in the aqueous phase in which the microorganisms are exposed to. This is due to a highly dynamic and non-linear gas-liquid transfer of hydrogen and biological reasons, such as direct interspecies hydrogen transfer in the liquid. Thus, the measurement of *dissolved hydrogen* is suggested as a more reliable index [22, 26–28].

Metabolic activity of microorganisms Sufficient nutrients and trace elements are important to microbial growth and metabolic activity, otherwise cells stop proliferating. As a consequence, quality and diversity of microbes will reduce in digesters. The monitoring of microbial communities and their specific metabolic activity is therefore a useful tool for describing the behavior of the biogas process [20, 29]. In fact, all suggested monitoring parameters so far, such as pH, hydrogen concentration, VFA, alkalinity and gas consumption, are "external" parameters or products excreted by cell activity. The actual activity of microorganisms is not necessary proportional to these measures [9]. If we could assess the vital parameters of the microorganisms, this would be the most reliable way of monitoring the biogas production process.

1.2.2 State variables

For maintaining constant operation conditions and for a continuous diagnosis of process performance a number of process parameters have to be captured regularly. Those state variables include, for instance, total solids' content, biogas production and composition, temperature, pH value as well as buffer capacity. These parameters often do not allow adequate time for corrective action (e.g., stopping or decreasing of feed rate) to prevent digester failures as explained on the basis of the pH value in the following.

Temperature Thermodynamics and kinetics of biological processes such as survival and growth of microorganisms as well as their metabolic activity are affected by temperature [7, 30]. Temperature fluctuations are various including fluctuations determined by season and weather, addition of new feedstock, formation of temperature gradients due to insufficient insulation, inadequately placed heating elements and mixers. Thus, temperature is one of the most important variables in controlling the rate of microbial metabolism in anaerobic environments [31].

Biogas plants commonly operate either at mesophilic (32 °C to 42 °C) or thermophilic temperature (48 °C to 55 °C) conditions as methanogens grow optimally at those temperatures [3, 4]. Thermophilic bacteria are more sensitive to temperature fluctuations and require a longer time to adapt to a new temperature, in order to reach the maximum methane production. Mesophilic bacteria are less sensitive and temperature fluctuations of ±3 °C are tolerated, without significant reduction in methane production [32]. Additionally, it is important to keep in mind that physico-chemical properties (such as pH value, conductivity, viscosity and solubility) are as well influenced by temperature. Therefore, only temperature-dependent readings can be considered reliably.

pH value Enzymatic activity of bacteria is affected by the pH level, since each enzyme is active only in a specific pH range and has maximum activity at its optimal pH. The physiological pH value of the anaerobic digestion process occurs in the pH interval of approximately pH 6 – pH 8.5 [6]. Most methanogens have an optimum between pH 7 and pH 8, while the acid-forming bacteria often have a lower pH optimum of about pH 5 – pH 7 [33]. Typically, the pH value is kept constant by natural processes. However, there are many factors in digesters as well as in the feedstock that can affect the overall level of pH in the digester. Especially, organic acids and carbon dioxide can lower the pH, while ammonia will contribute to an increase of pH. In a reactor with low buffering capacity, the pH value can be a useful indicator based on the fact that a pH drop corresponds to VFA accumulation [8, 9]. On the other hand, the pH response has low sensitivity in well-buffered systems, as an unintentionally large input of organic acids does not necessarily result in a drop in pH [34]. The high buffering capacity due to strong buffers such as bicarbonate, ammonia and VFAs will resist pH changes and the pH drop will often only occur just after the process is severely imbalanced. Therefore, the pH value cannot be used as a "primary" process indicator. Nevertheless, the pH value should be used as a significant additional information that describes the actual state of the digester [35].

Electrolyte conductivity Ionic conductivity of an electrolyte solution is a measure of its ability to conduct (ionic) electricity. It is a sum parameter of conductivity contributions from all cations and anions in the mixture, and depends on many chemical components including organic acids and bases. The electrolyte conductivity of biogas digestate correlates also with the content of free ammonia and the total alkalinity [36]. Thus, electrolyte-conductivity measurements can be applied as an extra process variable. In particular, if buffering substances such as bicarbonate are added to the digester content, the electrolyte conductivity is used as additional indicator for control purposes.

1.3 State of the art of biogas process monitoring

An increasing variety and number of sensing devices are used both in academia and industry for the monitoring and control of the biogas process. An overview of sensors and devices for the detection of the previously introduced parameters (dissolved hydrogen concentration, metabolic activity of microorganisms, temperature, pH value and electrolyte conductivity) will be given in the following.

1.3.1 Sensors for the detection of hydrogen and dissolved hydrogen

The hydrogen content in the *headspace* can be measured on-line using a manifold of hydrogen gas sensors. A review about hydrogen sensors in general has been given by Hübert *et al.* recently [37]. The hydrogen fraction in the headspace is commonly determined by gas chromatography followed by a specific detector cell. A thermal conductivity detector was applied for the detection of hydrogen gas, giving a detection limit of about 1 Pa [38–40]. With the GMI Exhaled Hydrogen Monitor (Gas Measurement Instruments Ltd., Renfrew, Scotland), originally designed for measuring the hydrogen content of exhaled breath standards, hydrogen was measured accurately down to 0.1 Pa [23, 35, 41]. Lundström has developed a palladium metal-oxide-semiconductor (Pd-MOS) hydrogen gas sensor [42]. With this sensor, H_2-producing *Escherichia coli* fermentation were followed on-line [43, 44]. Sakthivel *et al.* proposed a polymer-based limiting-current hydrogen sensor. With this sensor arrangement, the catalytic electrode poisoning of carbon dioxide gas mixture along with hydrogen was eliminated by means of a palladium diffusion barrier on top of the sensing platinum electrode [45].

Several researchers have recognized the importance of hydrogen monitoring in the *liquid phase*. Off-line dissolved hydrogen measurements of anaerobic systems have been reported in [46–48]. Herein, methods were proposed consisting of the measurement of hydrogen in the gas phase after its quantitative extraction from the liquid phase. These extraction techniques involve several steps and cannot

be automated or used where on-line and real-time analysis is required. Methods for on-line monitoring include the transfer of hydrogen from the liquid through a gas-permeable membrane, followed by gas-phase quantification. These quantification techniques involve mass spectrometry [25, 49–53] or gas chromatography equipped with specific detectors [54, 55]. However, the sophistication and high costs restrict these techniques to laboratory use. Recently, a novel approach for the on-line measurement of dissolved gases in a biogas production plant was reported by Schelter *et al.* [56]. This technique combines a membrane-free extraction of dissolved gases with gas chromatography followed by a coulometrically operated high-temperature solid-electrolyte cell. Low-cost methods to detect the dissolved hydrogen concentration more directly include the hydrogen/air fuel cell detector [22, 26], the hydrogen-sensitive Pd-MOS sensor combined with a liquid-to-gas membrane extraction procedure [13, 57], membrane-covered amperometric electrodes for the direct liquid-phase measurement of hydrogen [19, 58, 59] and a trace-reduction gas analyzer [60]. These techniques exhibit high sensitivity with a detection limit in the nanomolar range.

Also, two amperometric hydrogen sensors for the in-situ determination of hydrogen containing aqueous solutions have been launched on the bioanalytical market. This includes the H_2 microsensor-500 from the company Unisense (Aarhus, Denmark), which has a 500 micron tip diameter and a detection limitation of 0.3 µM in water as well as a H_2 measuring instrument with an amperometric microsensor from the company AMT Analysenmesstechnik GmbH (Rostock, Germany). The life time of these sensors is restricted to approximately six months due to the formation of biofilms or other adherent layers on the membrane. In addition, cross-sensitivities towards hydrogen sulfide lead to errors and/or a reduced life time.

1.3.2 Methods for assessing of the metabolic activity

Monitoring of the metabolic activity is focused on the status of relevant organisms of the biogas process [17]. Much is known about the basic metabolisms in different types of anaerobic digestion processes, but little is known about the microorganisms responsible for these processes. Only a few percent of bacteria and methanogens have been isolated so far [3]. Thus, monitoring of metabolic activity takes the identification of organisms relating to environmental conditions and performance for granted [61]. A number of methods have been exploited concerning the screening of the microbial community and their specific activity, populations and identification of organisms. Directly counting the number of methanogenic population has shown to be related to methane production [62]. Near-infrared spectroscopy (NIR) has been reported as an attempt to measure biomass density on-line [63, 64]. A simple and rapid technique suitable for identification

of microorganisms can be applied by using fluorescence *in-situ* hybridization (FISH) [16]. Measurement of microbial diversity and community structure can be conducted by genetic fingerprinting techniques such as denaturing gradient gel electrophoresis (DGGE) [65], temperature gradient gel electrophoresis (TGGE) [66] and terminal restriction fragment length polymorphism (T-RFLP) [67]. The direct measurement of the metabolic activity can be performed by batch tests such as specific methanogenic activity (SMA) [17]. The level of specific co-enzymes relating to cell metabolism such as F_{420} and NADH (nicotinamide adenine dinucleotide hybrid) have been used to correlate with microbial activities or the number of active organisms in the digester [68]. Most of the above-mentioned methodologies are only available off-line and require expensive instrumentation and tremendous amount of laboratory work and expertise [8, 9].

A relatively new approach is to analyze the metabolic activity of relevant microorganisms of the biogas process by determining the uptake of nutrients and/or release of metabolic end products by means of (bio-)chemical sensors [69, 70]. More precisely, living microorganisms are applied to a pH-sensitive sensor surface. Due to their metabolism, cells excrete acidic byproducts and thus acidify their environment, which can be detected by the sensor. The aim of this approach is to develop a tool sensitive enough for the detection of slightest changes in activity of the microorganisms, which can be seen as overall indicator of the biogas process.

The coupling of cells on field-effect-based semiconductor sensors was first proposed by Hafeman *et al.* in 1988 [71]. In this arrangement, a so-called light-addressable potentiometric sensor (LAPS) was used, wherein the surface potential of the sensor is determined via a photo-current measurement. In the 1990s, the company Molecular Devices Cooperation (USA) launched a device "Cytosensor® Microphysiometer" on the market, which is based on the LAPS principle. With this system, it was possible for the first time to monitor physiological processes of cells under non-invasive environments, in particular, with respect to their metabolic activity [72]. In recent years, various research groups studied the development of such LAPS sensors to realize, for instance, a "chemical imaging" using a scanning laser unit [73, 74], to build up multi-LAPS arrangements for the simultaneous detection of several analyte molecules to perform studies on single cells [69, 70, 72, 75–77] or to achieve improved spatial resolution of the LAPS system [78, 79]. The results achieved by LAPS have in principle proven the feasibility of cultivation of microorganisms such as cells and bacteria on field-effect devices.

1.3.3 Sensing of process temperature

In practice, the operation temperature is chosen with consideration to the feedstock used. In order to maintain a constant process temperature and to compensate eventual heat losses, digesters are isolated and heated by external heating sources such as floor- or wall-heating systems. To avoid temperature fluctuations inside the digester, pre-heating of the feedstock is additionally applied [4]. Reactor temperature control is achieved preferentially in high-rate digesters by PID (proportional-integral-derivative) control and temperature sensors available in industrialized standards such as Pt100 or thermocouples.

1.3.4 Sensing of the pH value

In-situ or in-line pH monitoring of an anaerobic digester is more representative of the pH contents than off-line due to the loss of CO_2 between sample drawing and analysis. If the sample is allowed to stand exposed to the air for a few minutes the dissolved CO_2 will be liberated, causing a pH change. Hence, the pH value is usually measured in the liquid state [11]. The pH value is relative straightforward to determine with conventional pH-glass electrodes. Due to drift and fouling problems of the diaphragm of the internal reference electrode, pH-glass electrodes require frequent re-calibration as well as washing and other cleaning (e.g., ultrasonic) systems, respectively [80]. Polymer-filled electrodes with a Ag/AgCl reference electrodes isolated by a Xerolyte® solid-electrolyte sample interface are typically less susceptible to fouling and retain calibrations for longer. These electrodes exhibit an open port, instead of the conventional ceramic junction between the sample and the reference electrolyte, which substantially reduces the risk of clogging.

1.3.5 Sensing the electrolyte conductivity

Electrolyte-conductivity measurements are routinely used as a fast, inexpensive and reliable way of measuring the ionic salt content in the biogas broth as a sum parameter. Especially, if buffering substances such as sodium bicarbonate are used to prevent economic costs of loss of efficiency caused by acidification, the measurement of electrolyte conductivity can be a useful supplementary process variable. Depending on the demanded size and geometry, macroscopic and miniaturized sensor cells with two or more electrodes (e.g., four-electrode conductivity meter) are commercially available as conductometric sensors. Nevertheless, none of these are developed for monitoring biogas processes.

1.4 Outline of the thesis

This thesis is focusing on the design and development of miniaturized solid-state transducers and their use as physico-chemical sensors to be applied for the monitoring of several parameters in biogas digesters. The parameters of interest are the dissolved hydrogen concentration, metabolic activity, electrolyte conductivity, pH value and temperature. For this, sensor structures based on different transducer principles, namely amperometry, potentiometry and conductometry have been designed and developed. The fabrication of these sensors was based on standard silicon technology.

After an introduction to the main sensing principles of the sensors used in the thesis in **Chapter 2**, the content of this thesis was split into scopes corresponding to peer-reviewed publications, referring to Chapters 3 to 6:

Chapter 3 describes the study of a combined amperometric/ field-effect sensor for the detection of the dissolved hydrogen concentration. The most important difference of this sensor compared to other macro- and miniaturized amperometric hydrogen sensors reported in literature, is the implementation of a pH-sensitive capacitive (electrolyte-insulator-semiconductor) EIS sensor in addition to the amperometric H_2 sensor. The field-effect based pH sensor is capable for an indirect detection of dissolved hydrogen. The output signal of the combined sensor is considered as "hydrogen signal" only, if the signal changes of both transducers are nearly simultaneous (with a small delay time necessary for the diffusion of H^+ ions generated at the amperometric electrode to the gate of the field-effect sensor). In this way, the selectivity of the combined sensor can be achieved. In contrast to macroscopic amperometric dissolved hydrogen sensors, a miniaturized sensor could eventually produced more cost effective, combined with other sensing principles and placed at different positions in the biogas reactor. In Chapter 3, special emphasis is devoted to the feasibility of the integration of two transducer principles on one chip, the study of their independent functionality as well as, the direct and indirect measurement of dissolved hydrogen.

In **Chapter 4**, a cell-based sensor for monitoring the metabolic activity by determining their extracellular acidification rate is presented. This new approach represents a straightforward way to study the "vitality" of relevant organisms of the biogas process. Metabolic responses of the model bacterium *Escherichia coli* in suspension as well as immobilized by gel entrapment on a capacitive field-effect structure were studied to pulses of glucose and acetate. Correlations between cell number, glucose and acetate concentration, acidification rate, and time of acidification period are examined. Advantageously a differential measurement is applied, which might give additional information of the pH value of the analyte.

Chapter 5 deals with the intensified study of the high-k[5] material barium strontium titanate (BST) as passivation and protection layer of a miniaturized electrolyte-conductivity sensor, which is referred to a capacitively coupled contactless conductivity detection (C^4D) sensor in the following. The choice of the insulating material that covers the electrodes in C^4D sensors is of primary importance. For optimal working and accurate measurements of the electrolyte conductivity with the C^4D sensor, the permittivity-to-thickness ratio of the protective layer should be larger than $0.4\,\mathrm{nm}^{-1}$. Due to the high dielectric constant of BST (e.g., ten-fold higher than Ta_2O_5) and the possibility to deposit this material via thin-film technology, this requirement can be met very well for the high-k BST films used in this study as protective material. An equivalent circuit model of the C^4D sensor chip is developed and discussed. The platinum electrodes were buried into the substrate material to obtain a planar structure for the protective coating with a thin but homogeneous coverage. For comparison, contact-mode electrolyte-conductivity (EC) sensors were also fabricated. Both sensors (EC and C^4D) were characterized in electrolyte solutions with various conductivities using two- and four-electrode operation modes to study the influence of the protective BST layer.

In a continuing study, presented in **Chapter 6**, a sensor chip for the multi-parameter detection of three physico-chemical parameters such as electrolyte conductivity, pH value and temperature is investigated using BST as multi-purpose material (e.g., high permittivity and pH-sensitive properties). This chip combines the capacitively coupled four-electrode electrolyte conductivity sensor introduced in Chapter 5 with a capacitive field-effect pH sensor and a thin-film Pt-temperature sensor. Here, BST is used due to its multi-functional properties as final outermost coating layer of the processed multi-parameter sensor chip. It serves as pH-sensitive transducer material for a field-effect pH sensor, as an insulation layer due to the high-k of BST for developing the contactless-conductivity sensor, and as passivation layer, which protects the metal electrodes of the conductivity and temperature sensors from corrosion, contamination and fouling. Multi-parameter characterization of the sensor chip in buffer solutions with different pH value and electrolyte conductivity are conducted. Finally, the sensor chip is exemplarily examined in biogas slurry to evaluate the sensor and the suitability of BST as multi-functional material under harsh environmental conditions.

Chapter 7 closes the current thesis with a final summary. The main findings of this work and potential future actions and challenges are discussed.

[5] The term high-k dielectric applies to a material with a high relative permittivity later on denoted as ϵ_i for barium strontium titanate.

1.5 Bibliography

[1] Soetaert, W.; Vandamme, E. J.: The impact of industrial biotechnology. *Biotechnology Journal* 1 (2006), No. 7-8, p. 756–769

[2] Soetaert, W.; Vandamme, E. J.: *Biofuels*. Hoboken / N.J.: Wiley, (2009). – ISBN 9780470754092

[3] Weiland, P.: Biogas production: Current state and perspectives. *Applied Microbiology and Biotechnology* 85 (2010), No. 4, p. 849–860

[4] Deublein, D.; Steinhauser, A.: *Biogas from waste and renewable resources: An introduction*. Weinheim: Wiley-VCH, (2011). – ISBN 978–3–527–32798–0

[5] Pöschl, M.; Ward, S.; Owende, P.: Evaluation of energy efficiency of various biogas production and utilization pathways. *Applied Energy* 87 (2010), No. 11, p. 3305–3321

[6] Ahring, B. K.: Perspectives for anaerobic digestion. Ahring, B. K. (Eds.): *Biomethanation I* 81. Berlin / Heidelberg: Springer, (2003). – ISBN 9783540443223, p. 1–30

[7] Angelidaki, I.; Ellegaard, L.; Ahring, B. K.: A mathematical model for dynamic simulation of anaerobic digestion of complex substrates: Focusing on ammonia inhibition. *Biotechnology and Bioengineering* 42 (1993), No. 2, p. 159–166

[8] Boe, K.: *Online monitoring and control of the biogas process*. Lyngby, Technical University of Denmark, Diss., (2006)

[9] Pind, P. F.; Angelidaki, I.; Ahring, B. K.; Stamatelatou, K.; Lyberatos, G.: Monitoring and control of anaerobic reactors. Scheper, T. (Eds.): *Advances in Biochemical Engineering/ Biotechnology* 82. Berlin / Heidelberg: Springer, (2003), p. 135–182

[10] Mackie, R.; Bryant, M. P.: Metabolic activity of fatty acid-oxidizing bacteria and contribution of acetate, propionate, butyrate and CO_2 to methanogenesis in cattle waste at 40 and 60 °C. *Applied and Environmental Microbiology* 41 (1981), No. 6, p. 1363–1373

[11] Boe, K.; Batstone, D. J.; Steyer, J.-P.; Angelidaki, I.: State indicators for monitoring the anaerobic digestion process. *Water Research* 44 (2010), No. 20, p. 5973–5980

[12] Molina, F.; Castellano, M.; García, C.; Roca, E.; Lema, J. M.: Selection of variables for on-line monitoring, diagnosis, and control of anaerobic digestion processes. *Water Science and Technology* 60 (2009), No. 3, p. 615–622

[13] Björnsson, L.; Murto, M.; Jantsch, T. G.; Mattiasson, B.: Evaluation of new methods for the monitoring of alkalinity, dissolved hydrogen and the microbial community in anaerobic digestion. *Water Research* 35 (2001), No. 12, p. 2833–2840

[14] Hickey, R. F.; Switzenbaum, M. S.: The response and utility of hydrogen and carbon monoxide as process indicators of anaerobic digesters subject to organic and hydraulic overloads. *Research Journal of the Water Pollution* 63 (1991), No. 2, p. 129–140

[15] Ahring, B. K.; Sandberg, M.; Angelidaki, I.: Volatile fatty acids as indicators of process imbalance in anaerobic digestors. *Applied Microbiology and Biotechnology* 43 (1995), p. 559–565

[16] Schmidt, J. E.; Mladenovska, Z.; Lange, M.; Ahring, B. K.: Acetate conversion in anaerobic biogas reactors: Traditional and molecular tools for studying this important group of anaerobic microorganisms. *Biodegradation* 11 (2000), p. 359–364

[17] Sørensen, A. H.; Ahring, B. K.: Measurements of the specific methanogenic activity of anaerobic digestor biomass. *Applied Microbiology and Biotechnology* 40 (1993), p. 427–431

[18] Weiland, P.: Wichtige Messdaten für den Prozessablauf und Stand der Technik in der Praxis. *Gülzower Fachgespräche* 27. Gülzow: Fachagentur für Nachwachsende Rohstoffe (FNR), (2007), p. 17–31

[19] Strong, G. E.; Cord-Ruwisch, R.: An in situ dissolved-hydrogen probe for monitoring anaerobic digesters under overload conditions. *Biotechnology and Bioengineering* 45 (1995), No. 1, p. 63–68

[20] Switzenbaum, M. S.; Giraldo-Gomez, E.; Hickey, R. F.: Monitoring of the anaerobic methane fermentation process. *Enzyme and Microbial Technology* 12 (1990), No. 10, p. 722–730

[21] Harper, S. R.; Pohland, F. G.: Recent developments in hydrogen management during anaerobic biological wastewater treatment. *Biotechnology and Bioengineering* 28 (1986), No. 4, p. 585–602

[22] Pauss, A.; Samson, R.; Guiot, S. R.; Beauchemin, C.: Continuous measurement of dissolved H_2 in an anaerobic reactor using a new hydrogen/air fuel cell detector. *Biotechnology and Bioengineering* 35 (1990), No. 5, p. 492–501

[23] Archer, D. B.; Hilton, M. G.; Adams, P.; Wiecko, H.: Hydrogen as a process control index in a pilot scale anaerobic digester. *Biotechnology Letters* 8 (1986), No. 3, p. 197–202

[24] McCarty, P. L.; Smith, D. P.: Anaerobic wastewater treatment. *Environmental Science and Technology* 20 (1986), No. 12, p. 1200–1206

[25] Lloyd, D.; Whitmore, T. N.: Hydrogen-dependent control of the continuous thermophilic anaerobic digestion process using membrane inlet mass spectrometry. *Letters in Applied Microbiology* 6 (1988), No. 1, p. 5–10

[26] Pauss, A.; Guiot, S. R.: Hydrogen monitoring in anaerobic sludge bed reactors at various hydraulic regimes and loading rates. *Water Environment Research* 65 (1993), No. 3, p. 276–280

[27] Frigon, J.-C.; Guiot, S. R.: Impact of liquid-to-gas hydrogen mass transfer on substrate conversion efficiency of an upflow anaerobic sludge bed and filter reactor. *Enzyme and Microbial Technology* 17 (1995), No. 12, p. 1080–1086

[28] Guwy, A. J.; Hawkes, F. R.; Rozzi, A. G.: Hydrogen production in a high rate fluidised bed anaerobic digester. *Water Research* 31 (1997), No. 6, p. 1291–1298

[29] Amann, R.; Lemmer, H.; Wagner, M.: Monitoring the community structure of wastewater treatment plants: A comparison of old and new techniques. *FEMS Microbiology Ecology* 25 (1998), No. 3, p. 205–215

[30] Angelidaki, I.; Sanders, W.: Assessment of the anaerobic biodegradability of macropollutants. *Reviews in Environmental Science and Biotechnology* 3 (2004), No. 2, p. 117–129

[31] Westermann, P.; Ahring, B. K.; Mah, R.: Temperature compensation in *Methanosarcina barkeri* by modulation of hydrogen and acetate affinity. *Applied and Environmental Microbiology* 55 (1989), No. 5, p. 1262–1266

[32] Levén, L.; Eriksson, Anders R. B.; Schnürer, A.: Effect of process temperature on bacterial and archaeal communities in two methanogenic bioreactors treating organic household waste. *FEMS Microbiology Ecology* 59 (2007), No. 3, p. 683–693

[33] Angelidaki, I.; Ahring, B. K.: Anaerobic thermophilic digestion of manure at different ammonia loads: Effect of temperature. *Water Research* 28 (1994), No. 3, p. 727–731

[34] Björnsson, L.; Murto, M.; Mattiasson, B.: Evaluation of parameters for monitoring an anaerobic co-digestion process. *Applied Microbiology and Biotechnology* 54 (2000), p. 844–849

[35] Guwy, A. J.; Hawkes, F. R.; Wilcox, S. J.: Neural network and on-off control of bicarbonate alkalinity in a fluidised-bed anaerobic digester. *Water Research* 31 (1997), No. 8, p. 2019–2025

[36] Hölker, U.; Lenz, J.: *Publikationsreihe: Daten- und modellbasierte Praxisempfehlungen*. `www.biogas-wissen.de`, (March 2014)

[37] Hübert, T.; Boon-Brett, L.; Black, G.; Banach, U.: Hydrogen sensors – A review. *Sensors and Actuators B: Chemical* 157 (2011), No. 2, p. 329–352

[38] Zheng, H.; O'Sullivan, C.; Mereddy, R.; Zeng, R. J.; Duke, M.; Clarke, W. P.: Experimental and theoretical investigation of diffusion processes in a membrane anaerobic reactor for bio-hydrogen production. *International Journal of Hydrogen Energy* 35 (2010), No. 11, p. 5301–5311

[39] Lee, M. J.; Zinder, S.: Hydrogen partial pressure in a thermophilic acetate-oxidizing methanogenic coculture. *Applied and Environmental Microbiology* 54 (1988), No. 6, p. 1457–1461

[40] Logan, B. E.; Oh, S.-E.; Kim, I. S.; van Ginkel, S.: Biological hydrogen production measured in batch anaerobic respirometers. *Environmental Science and Technology* 36 (2002), No. 11, p. 2530–2535

[41] Collins, L. J.; Paskins, A. R.: Measurement of trace concentrations of hydrogen in biogas from anaerobic digesters using an exhaled hydrogen monitor. *Water Research* 21 (1987), No. 12, p. 1567–1572

[42] Lundström, I.: Hydrogen sensitive MOS-structures: Part 1. Principles and applications. *Sensors and Actuators* 1 (1981), p. 403–426

[43] Hörnsten, E. G.; Lundström, I.; Nordberg, B.; Mathisen, B.: The use of palladium metal oxide semicondcutor structures in quantitative studies of H_2 and H_2S in processes related to biogas production. *Bioprocess Engineering* 6 (1991), p. 235–240

[44] Hörnsten, E. G.: On culturing *Escherichia coli* on a mineral salts medium during anaerobic conditions. *Bioprocess Engineering* 12 (1995), p. 157–162

[45] Sakthivel, M.: A portable limiting current solid-state electrochemical diffusion hole type hydrogen sensor device for biomass fuel reactors: Engineering aspect. *International Journal of Hydrogen Energy* 33 (2008), No. 2, p. 905–911

[46] Conrad, R.; Aragno, M.; Seiler, W.: Production and consumtion of hydrogen in a eutrophic lake. *Applied and Environmental Microbiology* 45 (1983), No. 2, p. 502–510

[47] Conrad, R.; Phelps, T. J.; Zeikus, J. G.: Gas metabolism evidence in support of the juxtaposition of hydrogen-producing and methanogenic bacteria in sewage sludge and lake sediments. *Applied and Environmental Microbiology* 50 (1985), No. 3, p. 595–601

[48] Robinson, J. A.; Tiedje, J. M.: Kinetics of hydrogen consumption by rumen fluid, anaerobic digester sludge, and sediment. *Applied and Environmental Microbiology* 44 (1984), No. 6, p. 1374–1384

[49] Heinzle, E.; Lafferty, R. M.: Continuous mass spectrometric measurement of dissolved H_2, O_2, and CO_2 during chemolithoautotrophic growth of Alcaligenes eutrophus strain H 16. *European Journal of Applied Microbiology and Biotechnology* 11 (1980), No. 1, p. 17–22

[50] Degn, H.; Cox, R. P.; Lloyd, D.: Continuous Measurement of Dissolved Gases in Biochemical Systems with the Quadrupole Mass Spectrometer. Glick, D. (Eds.): *Methods of Biochemical Analysis* 31. Hoboken / N.J.: Wiley, (1985). – ISBN 9780470110522

[51] Whitmore, T. N.; Lloyd, D.: Mass spectrometric control of the thermophilic anaerobic digestion process based on levels of dissolved hydrogen. *Biotechnology Letters* 8 (1986), No. 3, p. 203–208

[52] Whitmore, T. N.; Lloyd, D.; Jones, G.; Williams, T. N.: Hydrogen-dependent control of the continuous anaerobic digestion process. *Applied Microbiology and Biotechnology* 26 (1987), No. 4, p. 383–388

[53] Meyer, B.; Heinzle, E.: Dynamic determination of anaerobic acetate kinetics using membrane mass spectrometry. *Biotechnology and Bioengineering* 57 (1998), No. 2, p. 127–135

[54] Krämer, H.; Conrad, R.: Measurement of dissolved H_2 concentrations in methanogenic environments with a gas diffusion probe. *FEMS Microbiology Ecology* 12 (1993), No. 3, p. 149–158

[55] Smolenski, W. J.: In situ rumen hydrogen concentrations in steers fed eight times daily, measured using a mercury reduction detector. *FEMS Microbiology Letters* 53 (1988), No. 2, p. 95–100

[56] Schelter, M.; Zosel, J.; Oelßner, W.; Mertig, M.: A novel method for measuring dissolved gases in liquids. *Sensors and Actuators B: Chemical* 193 (2014), p. 113–120

[57] Björnsson, L.; Hörnsten, E. G.; Mattiasson, B.: Utilization of a palladium-metal oxide semiconductor (Pd-MOS) sensor for on-line monitoring of dissolved hydrogen in anaerobic digestion. *Biotechnology and Bioengineering* 73 (2001), No. 1, p. 35–43

[58] Kuroda, K.; Gaiger Silveira, R.; Nishio, N.; Sunahara, H.; Nagai, S.: Measurement of dissolved hydrogen in an anaerobic digestion process by a membrane-covered electrode. *Journal of Fermentation and Bioengineering* 71 (1991), No. 6, p. 418–423

[59] Takeshita, T.; Tanaka, K.; Ishizaki, A.; Stanbury, P. F.: Development of a dissolved hydrogen sensor and its application to evaluation of hydrogen mass transfer. *Journal of Fermentation and Bioengineering* 76 (1993), No. 2, p. 148–150

[60] Cord-Ruwisch, R.; Mercz, T. I.; Hoh, C.-Y.; Strong, G. E.: Dissolved hydrogen concentration as an on-line control parameter for the automated operation and optimization of anaerobic digesters. *Biotechnology and Bioengineering* 56 (1997), No. 6, p. 626–634

[61] Dearman, B.; Marschner, P.; Bentham, R. H.: Methane production and microbial community structure in single-stage batch and sequential batch systems anaerobically co-digesting food waste and biosolids. *Applied Microbiology and Biotechnology* 69 (2006), No. 5, p. 589–596

[62] Solera, R.; Romero, L. I.; Sales, D.: Analysis of the methane production in thermophilic anaerobic reactors: Use of autofluorescence microscopy. *Biotechnology Letters* 23 (2001), p. 1889–1892

[63] Nordberg, A.; Hansson M.; Sundh, I.; Nordkvist, E.; Carisson H.; Mathisen, B.: Monitoring of a biogas process using electronic gas sensors and near-infrared spectroscopy (NIR). *Water Science and Technology* 41 (2000), No. 3, p. 1–8

[64] Zhang, Y.; Zhang, Z.; Sugiura, N.; Maekawa, T.: Monitoring of methanogen density using near-infrared spectroscopy. *Biomass and Bioenergy* 22 (2002), No. 6, p. 489–495

[65] Silvey, P.; Pullummanappallil P. C; Blackall, L. L.; Nichols, P.: Microbial ecology of the leach bed anaerobic digestion of unsorted municipal solid waste. *Water Science and Technology* 41 (2000), No. 3, p. 9–16

[66] Muyzer, G.; Smalla, K.: Application of denaturing gradient gel electrophoresis (DGGE) and temperature gradient gel electrophoresis (TGGE) in microbial ecology. *Antonie van Leeuwenhoek* 73 (1998), No. 1, p. 127–141

[67] Collins, G.; Woods, A.; McHugh, S.; Carton, M. W.; O'Flaherty, V.: Microbial community structure and methanogenic activity during start-up of psychrophilic anaerobic digesters treating synthetic industrial wastewaters. *FEMS Microbiology Ecology* 46 (2003), No. 2, p. 159–170

[68] Peck, M. W.; Chynoweth, D. P.: On-line fluorescence-monitoring of the methanogenic fermentation. *Biotechnology and Bioengineering* 39 (1992), No. 11, p. 1151–1160

[69] Werner, C. F.; Krumbe, C.; Schumacher, K.; Groebel, S.; Spelthahn, H.; Stellberg, M.; Wagner, T.; Yoshinobu, T.; Selmer, T.; Keusgen, M.; Baumann, Marcus E. M.; Schöning, M. J.: Determination of the extracellular acidification of *Escherichia coli* by a light-addressable potentiometric sensor. *Physica Status Solidi A* 208 (2011), No. 6, p. 1340–1344

[70] Werner, C. F.; Groebel, S.; Krumbe, C.; Wagner, T.; Selmer, T.; Yoshinobu, T.; Baumann, Marcus E. M.; Keusgen, M.; Schöning, M. J.: Nutrient concentration-sensitive microorganism-based biosensor. *Physica Status Solidi A* 209 (2012), No. 5, p. 900–904

[71] Hafeman, D. G.; Parce, J. W.; McConnell, H.: Light-addressable potentiometric sensor for biochemical systems. *Science* 240 (1988), No. 4856, p. 1182–1185

[72] Hafner, F.: Cytosensor® Microphysiometer: Technology and recent applications. *Biosensors and Bioelectronics* 15 (2000), No. 3-4, p. 149–158

[73] Yoshinobu, T.; Ecken, H.; Md. Ismail, A.; Iwasaki, H.; Lüth, H.; Schöning, M.: Chemical imaging sensor and its application to biological systems. *Electrochimica Acta* 47 (2001), No. 1-2, p. 259–263

[74] Miyamoto, K.; Ichimura, H.; Wagner, T.; Schöning, M. J.; Yoshinobu, T.: Chemical imaging of the concentration profile of ion diffusion in a microfluidic channel. *Sensors and Actuators B: Chemical* 189 (2013), p. 240–245

[75] Mestres, P.; Morguet, A.: The Bionas technology for anticancer drug screening. *Expert Opinion on Drug Discovery* 4 (2009), No. 7, p. 785–797

[76] Solé, M.; Rius, N.; Lorén, J. G.: Rapid extracellular acidification induced by glucose metabolism in non-proliferating cells of *Serratia marcescens*. *International Microbiology* 3 (2000), No. 1, p. 39–43

[77] Owicki, J. C.; Parce, J. W.: Biosensors based on the energy metabolism of living cells: The physical chemistry and cell biology of extracellular acidification. *Biosensors and Bioelectronics* 7 (1992), No. 4, p. 255–272

[78] George, M.; Parak, W. J.; Gerhardt, I.; Moritz, W.; Kaesen, F.; Geiger, H.; Eisele, I.; Gaub, H. E.: Investigation of the spatial resolution of the light-addressable potentiometric sensor. *Sensors and Actuators A: Physical* 86 (2000), No. 3, p. 187–196

[79] Nakao, M.; Inoue, S.; Yoshinobu, T.; Iwasaki, H.: High-resolution pH imaging sensor for microscopic observation of microorganisms. *Sensors and Actuators B: Chemical* 34 (1996), No. 1-3, p. 234–239

[80] Zosel, J.; Schwarz, J.; Vonau, W.; Hoffmann, M.; Schewtschenko, O.; Gerlach, M.; Schickram, K.; Woratz, M.: Long-term stable pH measurement in the rumen of ruminants. *ITG-Fachbericht: Sensoren und Messsysteme 2014*. Berlin / Offenbach: VDE-Verlag, (2014). – ISBN 9783800736225, p. 1–5

2 Theory

This section provides general information on the physics and chemistry of the sensing principles of the sensors used in the present thesis.

2.1 Amperometric gas sensors

An combined amperometric/field-effect sensor for the detection of dissolved hydrogen is introduced in Chapter 3. The basic concept of the amperometric sensing part is explained in the following on the basis of amperometric hydrogen gas sensors. Amperometric gas sensors work at a constant applied voltage, which allows conversion of the electro-active analyte and the sensor signal is a concentration-dependent *limited current*. A review of amperometric gas sensors is given by Stetter and Li [2] and the state of the art in electrochemical hydrogen

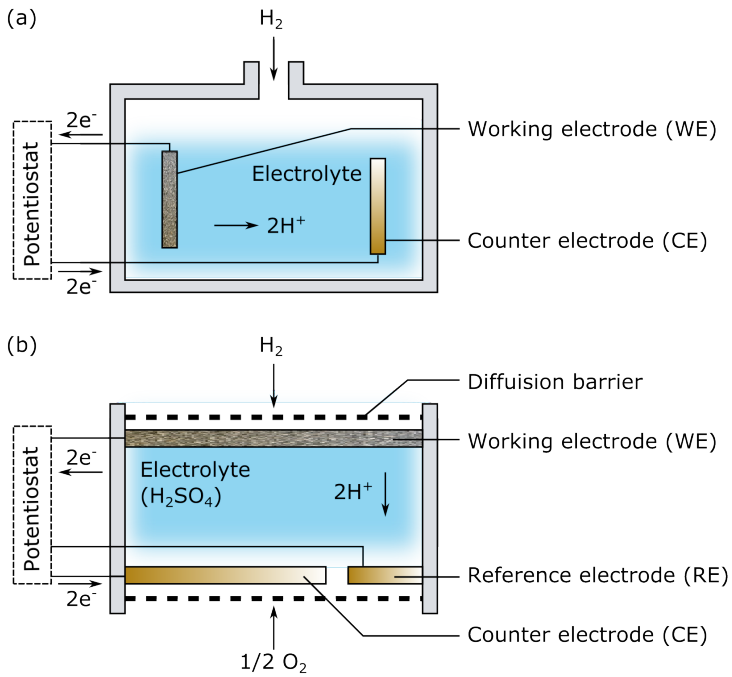

Figure 2.1: Illustration of amperometric gas sensors in (a) two- and (b) three-electrode configuration (adapted from [1]).

sensing has been reviewed by Korotcenkov et al. [1]. As depicted in Fig. 2.1, an amperometric gas sensor consists of three major constituents:

- The first of these are the electrodes, at which the electron transfer occurs. According to Fig. 2.1a, the simplest amperometric cell requires at least two electrodes, namely the working and the counter electrode. Commonly, a potentiostat is used to maintain a constant potential. The two-electrode detection principle implies that the potential of the counter electrode remains constant. In reality, the surface reactions at each electrode cause them to polarize and significantly limit the concentrations of reactant gas they are able to measure. In practice, most sensors include therefore also a third electrode, as depicted in Fig. 2.1b. In three-electrode designs, a potential is applied between a reference and working electrode and the current is measured between the latter and the counter electrode. Since the reference electrode is often shielded from reactions, it remains the thermodynamic potential of the working electrode constant during sensing. The electrodes are usually composed of noble metals, mostly in porous or high surface area designs. Often, platinum is applied, which acts as a catalyst for the hydrogen oxidation reaction.

- Secondly, the amperometric gas detector consists of a solid or liquid electrolyte to allow the transport of ions between the electrodes. The electrolyte is usually a proton-conducting material and in hydrogen sensing the most commonly used liquid electrolyte is sulphuric acid [3–5]. Solid electrolytes have some advantages over liquid electrolytes as they prevent leakage, corrosion and volatilization. The most commonly used proton-conducting solid polymer electrolyte is Nafion® [6–9], while ceramic materials are employed for high-temperature applications [10–12].

- Finally, a gas-permeable barrier may cover the inlet to the working electrode. It determines the rate of mass transport and controls the limiting current. In addition, the layer prevents leakage or drying out the electrolyte. If an appropriate material is utilized, it allows selective passage of the analyte and thereby preventing interference from other gases. In many cases, the membrane is composed of polytetrafluoroethylene (PTFE), which is well known by the trade name of Teflon® by DuPont.

Hydrogen participating in the electrochemical reaction diffuses through the porous layers (if present), dissolves in the electrolyte and is oxidized at the working electrode as follows:

$$H_2 \rightarrow 2e^- + 2H^+ \tag{2.1}$$

This results in a change of the working electrode potential. At the counter electrode the reduction of oxygen takes place according to the following equation:

$$1/2O_2 + 2H_2 + 2e^- \rightarrow H_2O \tag{2.2}$$

This process results in a flow of electrons from the working to the counter electrode and constitutes an electric current. Depending on the sensor design, the observed current can be either limited by the *rate of reaction at the electrode surface* or the *rate of diffusion* including the mass transport of the reactant to the electrode surface.

In the first case, if the rates of diffusion processes are much faster than the rate of reaction at the electrode, the current is controlled by the analyte reaction kinetics. The analyte reaches the surface much faster than it is reacted. The concentration is almost the same in the bulk of the solution and at the electrode surface. The expression for the current will take the form of:

$$i = n_e \cdot F \cdot k \cdot A \cdot c \cdot exp(\frac{\alpha_t n_e F E}{RT}) \tag{2.3}$$

where n_e represents the number of electrons per molecule reacting, F is the Faraday constant, k is the standard rate constant, A is the area of the electrode, c is the concentration, R is the universal gas constant and T is the absolute temperature in Kelvin, α_t and E are the transfer coefficient and the overpotential of the electrode reactions, respectively. If all conditions are held constant, the rate-limited current is proportional to the concentration c of the analyte with an exponential temperature coefficient. Equation 2.3 and derivation of this expression can be found in many textbooks [13, 14]. Due to degradation of the electrode's catalytic activity the limited current that is obtained in this kinetically controlled electrochemical region is not always stable.

This drawback can be overcome by operating the amperometric gas sensor in the region of *diffusion control* rather than the electrode's kinetic control. If the current is limited by a mass transport, e.g., by diffusion, the analyte is much slower than its consumption by reaction at the electrode surface. The analyte concentration at the electrode surface virtually falls to zero and each molecule of analyte that reaches the surface is immediately reacted. Under these conditions, the rate of the electrode reaction may be limited by the rate of diffusion through a gas-permeable membrane that is placed somewhere between the bulk analyte sample and the catalyst layer of the electrode. On the basis of *Fick's first law*, the limited current i_{lim} should now be governed by the rate at which the analyte transports to the surface of the electrode. This can usually be written as shown by Eq. 2.5:

$$i_{lim} = \frac{n_e \cdot F \cdot A \cdot D}{\delta} \cdot c \tag{2.4}$$

where A is the effective area of the membrane, D is the diffusion constant for the gaseous analyte in the medium of the membrane and δ is the thickness of the membrane.

The current can also be limited by the rate of diffusion across the diffusion layer in solution, and an expression similar to Eq. 2.5 can be used to calculate the current. However in this case, A in Eq. 2.5 is the effective surface area of the electrode, D is for diffusion of the analyte in solution and δ is the thickness of the diffusion layer in solution at the electrode surface [14, 15].

In these two cases, the limited current i_{lim} can be expressed as:

$$i_{lim} = k[H_2]_{gas} \tag{2.5}$$

where the measured current is directly proportional to the gaseous concentration - here H_2 - in convenient units such as part per million by volume (ppm (v/v))[2].

2.2 Field-effect-based potentiometric sensors

Potentiometric sensors differ from amperometric sensors in that they ideally operate at zero current conditions, i. e., in equilibrium. The measured quantity is the potential difference between the ion-selective electrode (ISE) and the reference electrode delivering a constant potential. The exchange of the analyte between the electrode and the electrolyte generates an interface potential at the electrode surface, which is given by the *Nernst equation* as:

$$E = E^0 + \frac{R \cdot T}{z_i \cdot F} ln(a_i) \tag{2.6}$$

where E^0 is the standard electrode potential and z_i and a_i are the ionic charge and activity, respectively, of the ion. Equation 2.6 predicts that the electrode potential is proportional to the logarithm of the activity of the ion monitored. For example, at room temperature a 59.1 mV change in the electrode potential should result from a tenfold change in the activity of a monovalent ion (z_i). Similar changes in the activity of a divalent ion should result in a 29.6 mV change of the potential.

In conjunction with the light-addressable potentiometric sensor (LAPS), the ion-sensitive field-effect transistor (ISFET) and the electrolyte-insulator-semiconductor (EIS) structure belong to the group of *field-effect-based* potentiometric sensing devices. These structures feature most of the advantages over the conventional ISE including properties such as small size, solid-state nature, mass fabrication, short response time [16]. The structural composition of an EIS structure as a capacitive layer sequence resembles the basic gate region of an ISFET, which was initially introduced by Bergveld [17]. In this work, pH-sensitive EIS structures

were examined within three aspects: (i) for the indirect measurement of dissolved hydrogen in Chapter 3, (ii) for the measurement of metabolic activity of microorganisms in Chapter 4, and (iii) as a pH sensor modified with barium strontium titanate as alternative pH-sensitive material for biogas monitoring applications in Chapter 6.

The EIS structure consists of an electrolyte-insulator-semiconductor structure as shown in Fig. 2.2a. The general sensing principle comprises two effects: The effect of the concentration-dependent surface potential and the field effect used to read out the surface potential. The field effect can be explained on the basis of the electric analogue, being a metal-insulator-semiconductor (MIS) structure. Therein, the electrolyte-transducer layer is replaced by a metal gate contact (see Fig. 2.2b). The MIS structure can be described as a parallel-plate capacitor. The difference and useful property of the MIS structure is, however, that the applied voltage on the gate modulates the space-charge distribution in the semiconductor and thus, the capacitance of the MIS structure.

Figure 2.3 depicts a theoretical C-V curve for an ideal MIS structure. The procedure for obtaining such a C-V curve includes the application of a DC bias voltage across the capacitor while superimposing a small AC signal. Depending on the magnitude and polarity of the applied gate voltage, the C-V curve shows three distinct regions comprising accumulation, depletion and inversion. These three states are usually clarified by means of energy-band diagrams and can be found in detail in many textbooks [18]. Qualitatively, the theory is explained on the basis of a p-type[1] semiconductor in the following and a schematic representation of the charge distribution is given in Fig. 2.4:

[1] An n-type semiconductor shows an identical behavior but the polarity of the voltage and the charge sign of the charge carriers are reversed.

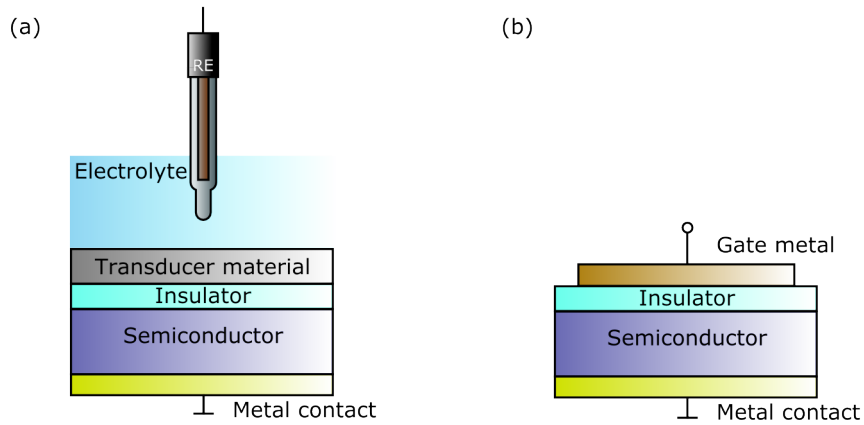

Figure 2.2: Schematic illustration of an EIS structure (a) and a MIS structure (b).

- *Accumulation* ($V_G < V_{FB}$): The application of a negative potential on the gate electrode attracts positive mobile charge carriers (holes) from the substrate to the insulator-semiconductor interface (Fig. 2.4a). The MIS capacitor behaves like a conventional parallel-plate capacitor. Thus, the total capacitance of the structure is solely defined by the capacitance of the insulator ($C = C_i$).

- *Depletion* ($V_{FB} < V_G < V_T$): By applying a small positive voltage to the gate electrode, the electric field pushes the mobile holes from the interface insulator/semiconductor into the substrate, thereby depleting the semiconductor of the mobile charge carriers and leaving a negative charge in the space-charge region, which is due to the ionized acceptor ions (Fig. 2.4b). The width of the depletion region (ω_d) depends on the applied voltage, the doping concentration, the dielectric constant and the insulator thickness [19]. The transition between accumulation and depletion condition is referred to as flat-band condition and occurs at the gate voltage (V_{FB}) by which the energy bands in the silicon continue horizontally up to the surface . This condition is met when there is no electric field in the

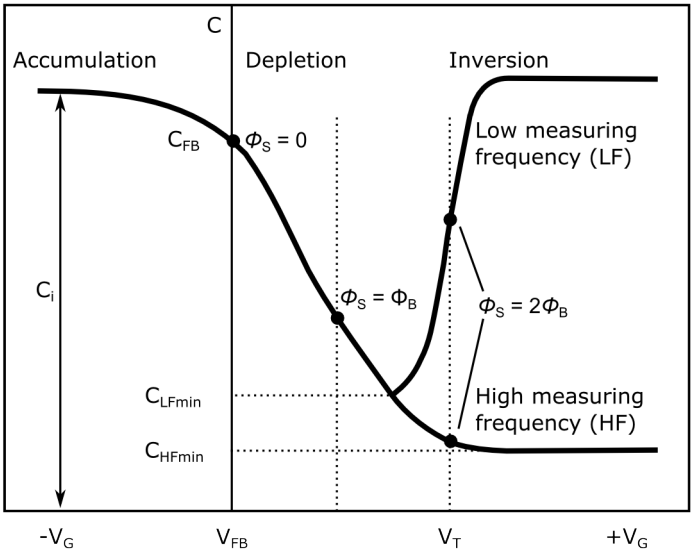

Figure 2.3: Theoretical C-V curve of an ideal p-type MIS structure at high and low measuring frequency. ϕ_S: semiconductor-surface potential, ϕ_B: potential difference between the Fermi level in the bulk semiconductor E_F and the intrinsic Fermi level E_i, C_i: insulator capacitance, C_{FB}: flat-band capacitance, C_{LFmin}: low-frequency minimum capacitance, C_{HFmin}: high-frequency minimum capacitance, V_G: gate voltage, V_T: threshold voltage (adopted from [19]).

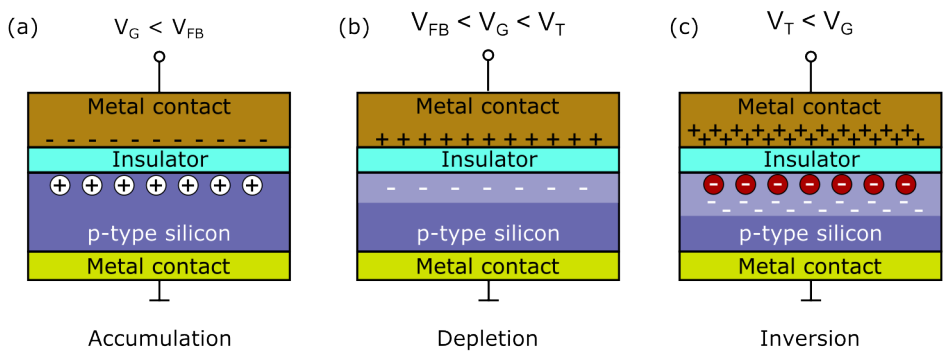

Figure 2.4: Schematic representation of accumulation, depletion and inversion of an ideal MIS structure (adopted from [18, 19]).

silicon, and the net-charge density in the silicon is zero.

- *Inversion* ($V_T < V_G$): If a more positive voltage, which is larger than the threshold voltage (V_T), is applied, the electron concentration on the interface exceeds the hole concentration and an inversion layer is formed (Fig. 2.4c). In other words, a thin n-type layer is created within the p-type semiconductor. The width of the space-charge region has reached its maximum. In the inversion region, the measured capacitance is strongly dependent on the measurement frequency. In the low-frequency regime, an increase of capacitance occurs as the gate-charge fluctuations are slowly enough that the inversion charge can follow the variation directly. At higher frequencies, the supply of charge carriers to the inversion layer is not sufficiently rapid to attain an equilibrium. As a result, C-V curves measured at high frequencies do not show the increase of capacitance in the inversion region [18, 19].

2.3 Solid/liquid interface

2.3.1 Electrical-double layer

If a solid surface (electrode) and a liquid are brought into contact, the charges of the solid surface cause an electric field at the solid/liquid interface. This electric field attracts counter ions from the electrolyte. The region which contains surface charges and counter ions is termed *electrical-double layer*. This arrangement creates an electrical potential difference between the bulk of the metal electrode and the bulk of the solution. In general, there are three models for the description of the electrical-double layer.

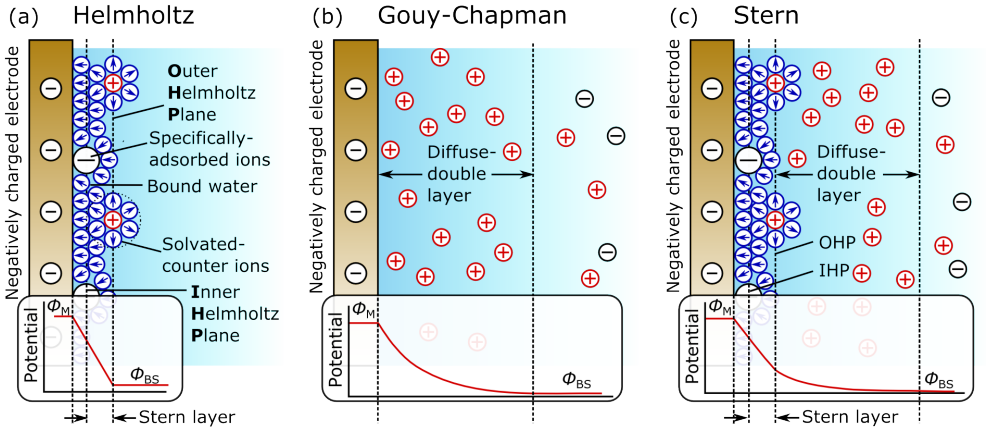

Figure 2.5: Schematic representation of the double-layer according to the Helmholtz model (a), the Gouy-Chapman model (b) and the Stern model (c) to describe the electrode-solution interface and the electrical-potential difference between electrode and bulk solution (potential of the metal ϕ_M and the bulk solution ϕ_{BS}) adapted from [21, 22].

The simplest model of an electrical-double layer was defined by von Helmholtz as schematically depicted in Fig. 2.5a for a negatively charged electrode. In the *Helmholtz layer model* solvated-counter ions arrange themselves along the surface of the electrode but are held away from it by their hydration shell. The location of the layer of ionic charge, which is called *outer Helmholtz plane* (OHP), is identified as the layer through the centers of the solvated ions. In this simple model, the electrical potential changes linearly within the layer bounded by the electrode surface on the one side and the OHP on the other side. The *inner Helmholtz plane* (IHP) is formed by specifically-adsorbed ions that have discarded their solvating water molecules and have become attached tightly to the electrode surface by chemical bonds. Inner and outer Helmholtz layers form the *compact* or *Stern layer* [20]. One drawback of the Helmholtz model is that it ignores disrupting factors such as diffusion and mixing in the solution. As a result of these influences, counter ions loosen from the Stern layer and the excess charge is smeared out in the direction of the electrolyte bulk to form a rather *diffuse-double layer* [20, 21].

This diffuse-double layer is also referred as *Gouy-Chapman layer*, which takes the disordering effect due to thermal motion into account. As shown in Fig. 2.5b, the local concentrations of cations and anions differ in the Gouy-Chapman model from their bulk concentrations. Ions of opposite charge cluster close to the electrode reflecting the counterbalance of ordering forces of the electrical field, whereas ions of the same charge are repelled from it due to the random thermal

motion. The Gouy-Chapman theory considers ions as point charges that can approach the surface arbitrarily close. As a result, the Gouy-Chapman model is not a very good representation of the structure of highly charged double-layers causing unrealistic high concentrations of ions near the surface [21].

The Gouy-Chapman model overemphasizes the rigidity of the local solution, whereas the Helmholtz model underemphasizes its structure [21]. In order to resolve this problem, the two models are combined in the *Stern model*. A schematic representation of the Stern model is shown in Fig. 2.5c. In the Stern model, the ions closest to the electrode are constrained into a rigid Helmholtz plane while outside that plane the ions are dispersed as in the Gouy-Chapman model.

2.3.2 Site-binding model

If the metal layer of the MIS structure is replaced by the electrolyte-insulating layer (see Fig. 2.2), an additional potential is formed at the interface between electrolyte and transducer which in turn depends on the analyte concentration. This potential modulates the flat-band voltage and thus, the width of the space-charge region of the semiconductor. The mechanism of the interface potential on the pH-sensitive gate insulators such as SiO_2, Ta_2O_5 or Si_3N_4[2] can be explained by the site-binding model. The surface of any metal-oxide layer comprises neutral amphoteric hydroxyl groups (MOH). The neutral surface hydroxyl sites of oxides are either able to bind (MOH_2^+) or release (MO^-) a proton according to the following reactions:

$$MOH \rightleftharpoons MO^- + H_B^+ \tag{2.7}$$

$$MOH_2^+ \rightleftharpoons MOH + H_B^+ \tag{2.8}$$

Herein, H_B^+ represents the protons in the bulk of the solution. As illustrated in Fig. 2.6, at a material-specific pH value, the so-called point of zero charge pH_{pzc}[3], the surface potential is equal to zero. At higher pH values ($pH > pH_{pzc}$), the oxide surface is negatively charged and at a smaller pH value ($pH < pH_{pzc}$) the surface is positively charged. A change in pH value changes the oxide-surface potential. The resulting pH-dependent electrical surface charge of the gate insulator will lead to a modulation of the capacitance of the EIS structure and thus, shifts the C-V curve along the voltage axis (see Section 4.3.1, Fig. 4.1b). The pH sensitivity of the capacitive EIS structure at the interface electrode/electrolyte in

[2] In contrast to oxides, the pH sensitivity of Si_3N_4 is explained by a modified site-binding model, which is based on the presence of two types of sites (amine, SiNH, and silanol, SiOH) on the surface [19].

[3] The pH_{pzc} is 2.5 ± 0.3 for SiO_2, 2.8 ± 0.3 for Ta_2O_5 and 3-3.5 for Si_3N_4 [23].

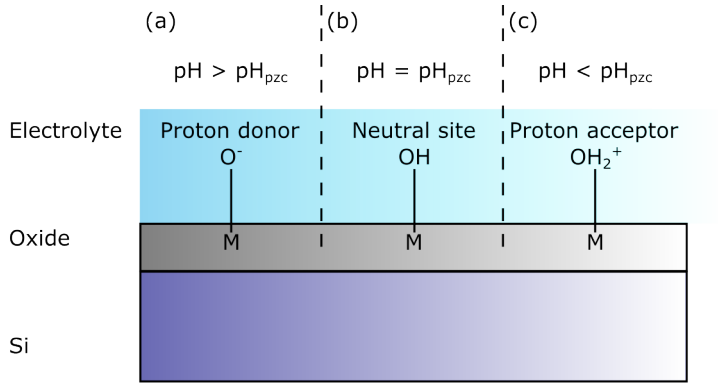

Figure 2.6: Schematic of the electrolyte-oxide interface with respective surface groups. Depending on the pH value of the electrolyte solution, the surface groups can be proton donors (a), neutral sites (b) or proton acceptors (c). The pH value for neutrality of the surface groups is the point of zero charge (pH_{pzc}) modified from [19].

response to a change of the surface potential is given by:

$$\frac{\delta\phi}{\delta pH_B} = -2.3\frac{kT}{e}\cdot\alpha_S \tag{2.9}$$

with

$$\alpha_S = \frac{1}{(2.3\cdot k_B T/e^2)(C_{dl}/\beta_{int})+1} \tag{2.10}$$

wherein k_B is the Boltzmann constant, T is the absolute temperature and e is the elementary charge. The parameter α_S describes a dimensionless sensitivity parameter, which varies between 0 and 1. The value α_S depends on the intrinsic surface-buffer capacity β_{int} as well as the differential-double layer capacitance C_{dl}. The surface-buffer capacity β_{int} characterizes the ability of the oxide surface to accept or donate protons, whereas the double-layer capacitance C_{dl} describes the ability of the electrolyte solution to adjust the amount of stored charge as a consequence of a small change in the electrostatic potential. Thus, it can be concluded from Eq. 2.9 and Eq. 2.10 that the maximum theoretical Nernstian sensitivity of 59.1 mV/pH for an univalent ion at 25 °C is achieved only if the parameter α_S approaches 1. This is the case for oxides with a high value for the surface buffer capacity β_{int} (high density of surface-active sites) and a low value of the differential double-layer capacity C_{dl} (mainly determined by the ion concentration). Due to the large surface-site density of Ta_2O_5 ($\sim 10^{15}$ cm^{-2}), this oxide possesses higher pH sensitivity than for instance SiO_2 with less surface sites of $\sim 5\times 10^{14}$ cm^{-2} [24, 25]. As a result, a nearly Nernstian pH sensitivity for the material TaO_5 is obtained in a pH range from pH 2 to pH 12 [26].

2.4 Conductometric sensors

Electrical conductivity is a measure for the ability of a solution to pass electric current. In contrast to metal conductors that pass electrons, in electrolyte solutions this current flow is carried out by positively and negatively charged ions. All ions present in the solution contribute to the current flow through the sensor and therefore, contribute to the conductivity measurement. The electrolyte conductivity σ depends on three main factors: (i) the concentration of ions c, (ii) the ability of ions to move in an electric field referred to as molar conductivity Λ_{m} and (iii) the valency z of ions in solution (Eq. 2.11):

$$\sigma = \sum_i (\Lambda_{m,i} \cdot z_i \cdot c_i) \tag{2.11}$$

Conductivity cannot be applied for the selective determination of a single type of ion, unless the sample solution consists of a single salt or the concentrations of all other ions are known. The molar conductivity Λ_{m} is mainly influenced by inter-ionic effects for strong electrolytes and the degree of dissociation for weak electrolytes. More concentrated salt solutions are expected to exhibit higher conductivities. This expectation is generally true and fails only at very high salt concentrations (strong electrolytes) near the solubility limit where the properties of the electrolyte drastically change mainly due to the limited availability of solvent. In addition, the viscosity of strong electrolytes can be large, which limits the ion mobility and yield diminished conductivity. For strong electrolytes, the relation between the concentration and the molar conductivity follows Kohlrausch's law (Eq. 2.12):

$$\Lambda_m = \Lambda_m^0 - A\sqrt{c} \tag{2.12}$$

Here, Λ_{m}^0 represents the limiting molar conductivity and A is a constant considering the inter-ionic effects that occur at finite dilution. A linear relationship is found for low concentrations if the molar conductivity is plotted as a function of the square root of the concentration. At infinite solutions, the graphical extrapolation for diluted solutions of strong electrolytes defines the limiting molar conductivity Λ_{m}^0. In this case, no inter-ionic effects can occur arising in an independent migration of cations and anions within the electric field. The limiting molar conductivity is defined as (Eq. 2.13):

$$\Lambda_m^0 = \lambda_+^0 + \lambda_-^0 \tag{2.13}$$

where λ_+^0 and λ_-^0 are the limiting ionic conductivities of the cations and anions, respectively. Due to the non-linear relationship between the molar conductivity and the concentration for weak electrolytes, a linear extrapolation cannot be executed. Weak electrolytes normally exist in a partially dissociated state such that some portion of the dissolved electrolyte exists in an uncharged form. This

fact makes the conductivity of a weak electrolyte much less than would be predicted [27–29].

The basic equipment needed to perform a conductivity measurement includes a conductivity meter, the analyte solution and a conductivity cell, as schematically depicted in Fig. 2.7. The conductivity meter applies a small alternating electrical

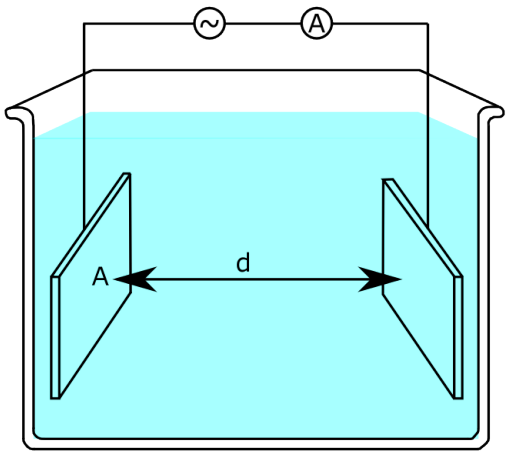

Figure 2.7: Schematic illustration of a basic conductivity cell.

current to a pair of electrodes immersed in a solution and the voltage drop is recorded. If the current and voltage are not shifted in phase, the electrolyte conductivity is inversely proportional to the solution resistance multiplied by the cell constant K_c according to (Eq. 2.14):

$$\frac{U}{I} = R_{el} = \frac{K_c}{\sigma} \tag{2.14}$$

The basic parameter of all conductivity cells is the cell constant, which is a scale factor dependent on the geometry of the sensor and the current path (often influenced by the overall geometry and volume of the sample). Considering a solution volume defined by two plane-parallel electrodes, the cell constant is equivalent to the distance d between the electrodes in relation to their surface area A (Eq. 2.15):

$$K_c = \frac{d}{A} \tag{2.15}$$

Due to variations in manufacturing tolerances, variations in surface area of the electrodes as well as Fringe effects on the electric field, the calculation in Eq. 2.15 is rather imprecise. For high-accuracy measurements, the cell constant has to be evaluated experimentally by calibration measurements in standard solutions having a specific conductivity [30]. Once the cell constant is assigned, the

conductivity can be calculated from the measured resistance R according to (Eq. 2.16):

$$\sigma = \frac{1}{R_{el}} \cdot \frac{d}{A} = G \cdot \frac{d}{A} \tag{2.16}$$

Ionic movement and therefore, conductivity measurement is directly proportional to temperature. In order to compare conductivity values at different temperatures, these are commonly related to a reference temperature T_{Ref} of 25 °C. Typically, a linear temperature compensation is immediately performed by the transmitter according to (Eq. 2.17):

$$\sigma_{Ref} = \frac{\sigma}{1 + \frac{\alpha_T}{100\%} \cdot (T - T_{Ref})} \tag{2.17}$$

$$\alpha_T = \frac{\Delta\sigma \cdot 100\%}{\Delta T \cdot \sigma_{Ref}} \tag{2.18}$$

where σ_{Ref} represents the conductivity for the reference temperature T_{Ref}, σ corresponds to the conductivity measured at the present temperature T and α_T is the temperature coefficient of the solution. This temperature coefficient α_T can be experimentally derived or can be found in textbooks for certain salt solutions [31].

2.5 Bibliography

[1] Korotcenkov, G.; Han, S. D.; Stetter, J. R.: Review of electrochemical hydrogen sensors. *Chemical Reviews* 109 (2009), No. 3, p. 1402–1433

[2] Stetter, J. R.; Li, J.: Amperometric gas sensors – A review. *Chemical Reviews* 108 (2008), No. 2, p. 352–366

[3] Chao, Y.; Yao, S.; Buttner, W. J.; Stetter, J. R.: Amperometric sensor for selective and stable hydrogen measurement. *Sensors and Actuators B: Chemical* 106 (2005), No. 2, p. 784–790

[4] Weng, Y.-C.; Hung, K.-C.: Amperometric hydrogen sensor based on Pt_xPd_y/Nafion electrode prepared by Takenata–Torikai method. *Sensors and Actuators B: Chemical* 141 (2009), No. 1, p. 161–167

[5] Weng, Y.-C.; Hung, K.-C.; Wang, J.-C.; Lee, Y.-G.; Su, Y.-F.; Lin, C.-Y.: Binary platinum–ruthenium/Nafion electrodes for the detection of hydrogen. *Sensors and Actuators B: Chemical* 150 (2010), No. 1, p. 264–270

[6] Lu, X.; Wu, S.; Wang, L.; Su, Z.: Solid-state amperometric hydrogen sensor based on polymer electrolyte membrane fuel cell. *Sensors and Actuators B: Chemical* 107 (2005), No. 2, p. 812–817

[7] Sakthivel, M.: A portable limiting current solid-state electrochemical diffusion hole type hydrogen sensor device for biomass fuel reactors: Engineering aspect. *International Journal of Hydrogen Energy* 33 (2008), No. 2, p. 905–911

[8] Liu, Y.-C.; Hwang, B.-J.; Tzeng, I.-J.: Solid-state amperometric hydrogen Sensor Using Pt/C/Nafion composite electrodes prepared by a hot-pressed method. *Journal of the Electrochemical Society* 149 (2002), No. 11, p. H173–H178

[9] Ramesh, C.; Murugesan, N.; Krishnaiah, M. V.; Ganesan, V.; Periaswami, G.: Improved Nafion-based amperometric sensor for hydrogen in argon. *Journal of Solid State Electrochemistry* 12 (2008), No. 9, p. 1109–1116

[10] Kriksunov, L. B.; Macdonald, D. D.: Amperometric hydrogen sensor for high-temperature water. *Sensors and Actuators B: Chemical* 32 (1996), No. 1, p. 57–60

[11] Taniguchi, N.; Kuroha, T.; Nishimura, K.; Iijima, K.: Characteristics of novel $BaZr_{0.4}Ce_{0.4}In_{0.2}O_3$ proton conducting ceramics and their application to hydrogen sensors. *Solid State Ionics* 176 (2005), p. 2979–2983

[12] Zhiykov, S.: Hydrogen sensor based on a new type of proton conductive ceramic. *International Journal of Hydrogen Energy* 21 (1996), No. 9, p. 749–759

[13] Bard, A. J.; Faulkner, L. R.: *Electrochemical Methods: Fundamentals and Applications*. New York: Wiley, (2001). – ISBN 0471043729

[14] Cao, J. R. Z. abd Stetter S. Z. abd Stetter: Amperometric gas sensors. Madou, M. (Eds.); Joseph, J. J. (Eds.): *Opportunities for Innovation: Chemical and Biological Sensors*. Gaithersburg, (MD): U. S. Department of Commerce, (1991). – ISBN NIST GCR 915931, p. (43–57)

[15] Chang, S. C.; Stetter, J. R.; Cha, C. S.: Amperometric gas sensors. *Talanta* 40 (1993), No. 4, p. 461–477

[16] Jimenez-Jorquera, C.; Orozco, J.; Baldi, A.: ISFET based microsensors for environmental monitoring. *Sensors* 10 (2010), No. 1, p. 61–83

[17] Bergveld, P.: Development, operation, and application of the ion-sensitive field-effect transistor as a tool for electrophysiology. *IEEE Transactions on Bio-Medical Engineering* 19 (1972), No. 5, p. 342–351

[18] Sze, S. M.; Ng, K. K.: *Physics of Semiconductor Devices*. Hoboken / N.J: Wiley, (2007). – ISBN 9780471143239

[19] Poghossian, A.; Schöning, M.: Silicon-based Chemical and Biological Field-effect Sensors. Grimes, C. (Eds.); Dickey, E. (Eds.); Pishko, M. (Eds.): *Encyclopedia of Sensors 10*. Stevenson Ranch (CA): American Scientific Publishers, (2006), p. 1–71

[20] Wang, J.: *Analytical Electrochemistry*. Hoboken / N.J: Wiley, (2006). – ISBN 9780471678793

[21] Atkins, P. W.: *Atkins' Physical Chemistry*. Oxford: Oxford University Press, (2014). – ISBN 9780199697403

[22] Butt, H.-J.; Graf, K.; Kappl, M.: *Physics and Chemistry of Interfaces*. Weinheim: Wiley-VCH, (2013). – ISBN 9783527412167

[23] Poghossian, A.: Determination of the pH_{pzc} of insulators surface from capacitance-voltage characteristics of MIS and EIS structures. *Sensors and Actuators B: Chemical* 44 (1997), No. 1-3, p. 551–553

[24] van Hal, R.; Eijkel, J.; Bergveld, P.: A novel description of ISFET sensitivity with the buffer capacity and double-layer capacitance as key parameters. *Sensors and Actuators B: Chemical* 24 (1995), No. 1-3, p. 201–205

[25] van Hal, R.; Eijkel, J.; Bergveld, P.: A general model to describe the electrostatic potential at electrolyte oxide interfaces. *Advances in Colloid and Interface Science* 69 (1996), No. 1-3, p. 31–62

[26] Bergveld, P.: Thirty years of ISFETOLOGY. *Sensors and Actuators B: Chemical* 88 (2003), No. 1, p. 1–20

[27] Schöning, M. J.; Glück, O.; Thust, M.: Electrochemical Composition Measurement. Webster, J. G. (Eds.): *The Measurement, Instrumentation, and Sensors Handbook*. Boca Raton (Fl): CRC Press published in cooperation with IEEE Press, (1999). – ISBN 3540648305, p. 70(1–49)

[28] Zoski, C. G.: *Handbook of Electrochemistry*. Amsterdam and Boston: Elsevier, (2007). – ISBN 9780444519580

[29] Hamann, C. H.; Hamnett, A.; Vielstich, W.: *Electrochemistry*. Weinheim: Wiley-VCH, (2007). – ISBN 9783527310692

[30] Bevilacqua, A. C.: The effect of temperature, temperature error, and impurities on compensated resistivity measurements. *Proceedings of the 16th Annual Semiconductor Pure Water and Chemicals Conference* (1997), p. 1–16

[31] Dobos, D.: *Electrochemical Data: A Handbook for Electrochemists in Industry and Universities*. Amsterdam / New York: Elsevier Scientific Pub. Co., (1975). – ISBN 9780444998637

3 Combined amperometric/field-effect sensor for the detection of dissolved hydrogen

Christina Huck[a,b], Arshak Poghossian[a,b], Patrick Wagner[c], Michael J. Schöning[a,b]

[a] *Institute of Nano- and Biotechnologies (INB), FH Aachen, Jülich, Germany*
[b] *Peter Grünberg Institute (PGI-8), Forschungszentrum Jülich GmbH, Jülich, Germany*
[c] *Institute for Materials Research (IMO), Hasselt University, Diepenbeek, Belgium*

Published in: *Sensors and Actuators B: Chemical*, Vol. 187, pp. 168–173, 2013, DOI: org/10.1016/j.snb.2012.10.050

Submitted: 2012-07-14; Accepted: 2012-10-09; Published: 2012-10-17

3.1 Abstract

Real-time and reliable monitoring of the biogas process is crucial for a stable and efficient operation of biogas production in order to avoid digester breakdowns. The concentration of dissolved hydrogen (H_2) represents one of the key parameters for biogas process control. In this work, a one-chip integrated combined amperometric/field-effect sensor for monitoring the dissolved H_2 concentration has been developed for biogas applications. The combination of two different transducer principles might allow a more accurate and reliable measurement of dissolved H_2 as an early warning indicator of digester failures. The feasibility of the approach has been demonstrated by simultaneous amperometric/field-effect measurements of dissolved H_2 concentrations in electrolyte solutions. Both, the amperometric and the field-effect transducer show a linear response behavior in the H_2 concentration range from 0.1 to 3 % (v/v) with a slope of (198.4 ± 13.7) nA/% (v/v) and (14.9 ± 0.5) mV/% (v/v), respectively.

3.2 Introduction

A stable and efficient operation of the biogas production has the potential to replace some of the limited fossil fuels [1]. The use of biogas as energy source is currently establishing in the group of alternative energies. In general, the natural process of anaerobic digestion is a relative stable system that occurs in

nature without the need for precise process control. However, under high loading conditions, process failures such as disadvantageous biogas yield or stoppage of the biogas production due to acidification of the medium are known to occur [2–4]. Therefore, real-time and reliable controlling and monitoring of the biogas process is crucial for a stable and efficient operation of biogas production in order to avoid digester breakdowns.

The concentration of dissolved hydrogen (H_2) represents one of the most important parameters for biogas process control in anaerobic digesters [5, 6]. Accumulated H_2 strongly inhibits the degradation of volatile fatty acids, such as propionate and butyrate, resulting in a consequent deterioration of normal operation [7]. A build-up of hydrogen above a critical concentration of higher than 0.04 µM has been reported as initial stage of digester overloading [7, 8]. If hydrogen production exceeds the maximum ability of the methanogenic biomass to degrade hydrogen, there will be a rapid and large increase in the hydrogen concentration prior to digester failures. Thus, dissolved hydrogen is a key factor in the intricate balance between microbial species involved in the multi-step degradation during anaerobic digestion, making it a useful parameter for biogas process monitoring and early warning of process disturbances [2, 3, 9–12].

Most of hydrogen sensors, used for monitoring the anaerobic biogas production, are based on the detection of H_2 in the gas phase of the digester [5, 13–15]. Dissolved H_2 in the liquid medium is thus calculated from the gas fraction, assuming that the hydrogen-transfer rate between the gas and the liquid phase is not limited. However, H_2 mass-transfer coefficients in anaerobic digesters are much smaller than those typically found in aerobic fermentation digesters [16]. That is because the culture broth of anaerobic digestion consists of a complex physico-chemical composition with respect to the H_2 solubility [17, 18]. This limits the rapidity with which an increase in H_2 concentration in the biomass can be detected in the gas phase of the digester. As a consequence, serious overloading of the digester may occur before the raised H_2 concentration in the gas phase is detected. Therefore, having a practical, reliable and low-cost instrumentation that provides a continuous and in-situ measurement of dissolved hydrogen in anaerobic digesters would be highly advantageous.

In this work, a Si-based combined chemosensor capable for the simultaneous amperometric/field-effect detection of the concentration of dissolved H_2 has been developed for biogas applications. Such a combination of two different transducer principles for the detection of the same parameter might allow a more accurate, selective and reliable measurement of dissolved H_2 as an early warning indicator of digester failures. The functioning of the developed one-chip integrated dual amperometric/field-effect chemosensor has been tested in electrolyte solutions with different concentrations of dissolved H_2.

3.3 Experimental

3.3.1 Structure and functioning principle of the combined H_2 sensor

The schematic layer structure of the combined dissolved H_2 sensor and the measurement setup for the simultaneous amperometric/field-effect detection of dissolved H_2 in electrolyte solutions is shown in Fig. 3.1. The developed sensor combines a pH-sensitive capacitive EIS (electrolyte-insulator-semiconductor) sensor consisting of an Al-p-Si-SiO_2-Ta_2O_5 structure and two circular-type thin-film Pt electrodes. The specific feature of the combined H_2-sensor chip is the implementation of the field-effect pH sensor in addition to well-known amperometric measurements. The field-effect pH sensor is a basic structural element of current chemical sensors and biosensors [19–25] and is used in this approach for an indirect detection of the dissolved H_2 gas. This new approach has been introduced by the authors for the first time in [26]. Thus, two transduction principles are closely combined at the microscale, enabling new electrochemical detection opportunities.

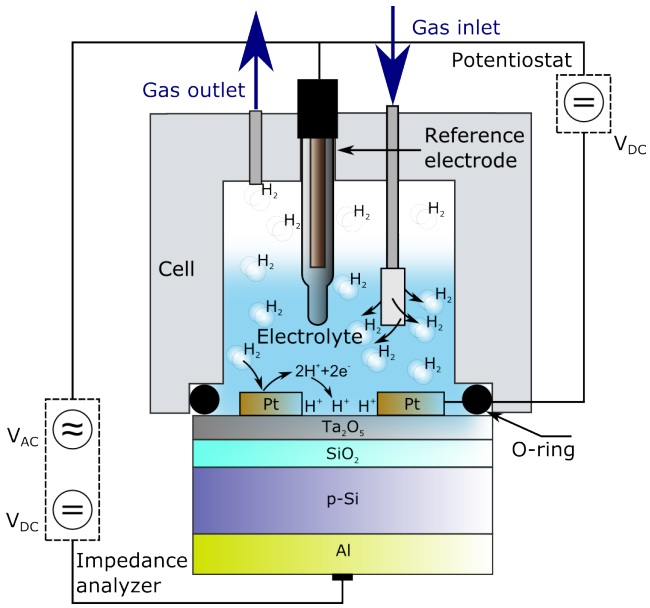

Figure 3.1: Schematic structure and measurement setup of the combined amperometric/field-effect dissolved H_2 sensor.

The operation principle of the combined sensor structure is assumed to be as follows. Dissolved H_2 diffuses to the polarized Pt working electrode and is electrochemically oxidized according to the following reaction [27, 28]:

$$H_2 \rightarrow 2e^- + 2H^+ \tag{3.1}$$

This causes a current depending on the dissolved hydrogen concentration. If the potential of the working electrode is adjusted (usually +0.55 mV *vs.* Ag/AgCl reference electrode) that any hydrogen molecule reaching the electrode surface is immediately oxidized, then the current will be controlled solely by the diffusion rate of hydrogen to the electrode surface. The most important difference of our H_2-sensor chip and other macro- or miniaturized amperometric H_2 sensors reported in literature [15, 27, 29, 30], is the existence of the one-chip integrated field-effect sensor, capable for an indirect detection of dissolved H_2. The product of H_2 oxidation, i.e., H^+ ions generated at the working electrode (see Eq. 3.1), will diffuse to the pH-sensitive gate-insulator surface (in this study, Ta_2O_5) and will be detected there. A resulting local pH decrease near the surface of the pH-sensitive layer leads to a change in the surface charge and thus, modulates the space-charge capacitance in the Si and consequently, the flatband voltage and capacitance of the EIS structure. In previous experiments, field-effect devices have been successfully used for the detection of H^+ ions that have been electrochemically generated via electrolysis of water [31, 32]. The output signal of the combined sensor is considered as "H_2 signal" only, if the signal changes of both the amperometric and the field-effect sensor are nearly simultaneous (with a small delay time necessary for the diffusion of H^+ ions generated at the amperometric electrode to the gate region of the field-effect sensor) and if the signal of the field-effect sensor is shifted towards more negative potentials that corresponds to an increase of the H^+ concentration. In this way, the selectivity of the combined sensor to H_2 detection can be achieved.

3.3.2 Fabrication of the combined sensor structure

The flowchart for the fabrication of the combined amperometric/field-effect H_2 sensor is shown in Fig. 3.2. For the realization of the field-effect sensor, capacitive Al-Si-SiO_2-Ta_2O_5 (p-Si, $\rho = 10\,\Omega\,\mathrm{cm}$; 30 nm thermally grown SiO_2 (Fig. 3.2a)) structures with a Ta_2O_5 layer as pH-sensitive gate insulator material have been fabricated. Ta_2O_5 is widely used for field-effect pH sensing, due to its high pH sensitivity [33] as well as high corrosion-resistance properties in a wide pH range [34]. The Ta_2O_5 films were prepared by means of thermal oxidation of an electron-beam deposited, 30 nm thick tantalum layer in dry oxygen atmosphere at 517 °C for about 30 min, yielding a ∼60 nm thick Ta_2O_5 layer (Fig. 3.2b). After etching the SiO_2 from the rear side of the wafer, a 300 nm Al film was deposited as a contact layer for the field-effect sensor (Fig. 3.2c).

For the preparation of the amperometric transducer, a Pt layer with a thickness of 200 nm was deposited together with an adhesion layer of 20 nm Ti by means of electron-beam evaporation and patterned as circular electrodes via photolithography and lift-off technique, respectively (see Fig. 3.2d). Platinum has an excellent

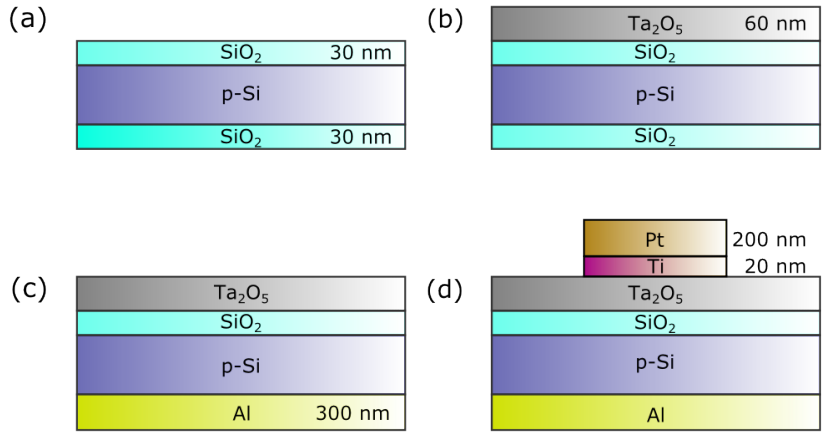

Figure 3.2: Flowchart for the fabrication of the combined dissolved H_2 sensor: (a) p-Si wafer with thermally grown SiO_2; (b) deposition of tantalum and thermal oxidation to Ta_2O_5; (c) etching of SiO_2 on the rear side and deposition of the Al back side contact; (d) deposition and patterning of the circular Pt thin-film electrodes.

electro-catalytic activity for hydrogen oxidation as compared to other metals [35, 36]. In a following step, the wafer was separated into single sensor chips with a size of 10 mm x 14 mm and assembled onto a printed circuit board (PCB). For electrical connection of the field-effect sensor, the Al rear-side contact of the EIS structure was glued with electrically conductive adhesive onto the PCB substrate. The front-side contacts to the platinum electrodes were provided by means of an ultrasonic wedge bonder. Finally, the electrical contacts were encapsulated with silicone rubber.

3.3.3 Measurement setup

For experiments, the PCB substrate with the combined dissolved H_2 sensor was mounted into a home-made measuring cell as it is schematically shown in Fig. 3.1. The front side of the sensor chip was contacted by the electrolyte and a conventional liquid-junction Ag/AgCl reference electrode (Metrohm). The sidewalls of the combined sensor chip were protected from the electrolyte solution by means of an O-ring, thereby circumventing the need for a complicated encapsulation process. The contact area of the combined sensor with the solution was about 0.4 cm^2 in total. Since the response of the field-effect pH sensor is inversely proportional to the buffer capacity [37], the measurements were performed in a low-capacity buffer solution to obtain a high sensor signal. As electrolyte, a 0.25 mM polymix multi-component buffer solution (pH 7) containing 100 mM sodium chloride (NaCl)

as an ionic-strength adjuster was used [38, 39].

The test chamber was provided with a gas inlet and outlet. Hydrogen gas was dissolved in the electrolyte through a perforated tube. The required gas composition was obtained by mixing hydrogen and nitrogen in various ratios (from 0 to 3 % (v/v) H_2) using commercial mass flow controllers (El-Flow, Bronkhorst High-Tech). The experiments were performed in a dark Faraday cage at room temperature (ca. 22 °C) and at a gas flow rate of 100 sccm.

The combined sensor has been characterized by means of amperometry using a potentiostat (PalmSens handheld potentiostat/galvanostat), and constant-capacitance (ConCap) method using an impedance analyzer (IM6, Zahner Elektrik). For the amperometric detection of dissolved H_2, a standard two-electrode configuration under potential control was used. The potential was set at +0.55 V *vs.* the Ag/AgCl reference electrode and the hydrogen concentration-dependent current was sampled every second. The ConCap mode allows a dynamic characterization of the field-effect EIS sensor. In this mode, the capacitance of the EIS sensor is kept constant (usually within the depletion region of the capacitance-voltage curve at ∼60 % of the maximum capacitance) using a feedback-control circuit, and potential changes at the transducer/electrolyte interface were directly monitored. For operation of the field-effect sensor, a DC (direct current) polarization voltage is applied via the reference electrode to set the working point of the EIS sensor, and a small AC (alternating current) voltage (20 mV) is applied to the system in order to measure the capacitance of the sensor. All field-effect measurements were carried out at a frequency of 120 Hz. A custom-made LabVIEW "virtual instrument" program was developed for experimental control and data acquisition.

3.4 Results and discussion

3.4.1 pH sensitivity of the capacitive EIS sensor

Before the H_2 experiments were performed, the pH sensitivity of the capacitive field-effect p-Si-SiO_2-Ta_2O_5 structure has been characterized. Fig. 3.3 depicts a typical dynamic ConCap response of the EIS sensor recorded in Titrisol buffer solution with different pH values. The EIS sensor shows an average pH sensitivity of 57.4 mV/pH in the linear range from pH 3 to pH 9, which is in good agreement with pH sensitivity values reported in literature for a Ta_2O_5 layer [34, 40, 41].

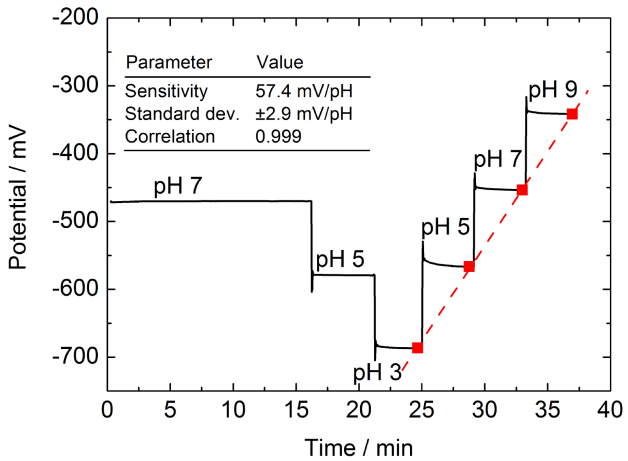

Figure 3.3: Typical dynamic ConCap response of a capacitive p-Si-SiO_2-Ta_2O_5 field-effect EIS structure recorded in Titrisol buffer with different pH values from pH 3 to pH 9 and corresponding calibration curve (inlet, red line).

3.4.2 Validation of independent functioning of the one-chip integrated field-effect and amperometric transducers

The functioning principle of the pH-sensitive field-effect sensor is based on the detection of pH-induced potential changes at the gate-insulator/electrolyte interface, whereas the amperometric detection relies on an electron-transfer reaction (reduction or oxidation) of an electro-active specimen at the working electrode. Since the developed dissolved H_2 sensor combines both transducer principles, in separate experiments, the independent functioning of the field-effect and amperometric transducers integrated on one single chip has been investigated. For this, HCl was added in the measuring solution to stimulate a response of the field-effect sensor and simultaneously, to study the impact of pH changes on the amperometric signal. On the other hand, the well-known electrochemically reversible ferricyanide/ferrocyanide ($[Fe(CN)_6]^{3-}$/$[Fe(CN)_6]^{4-}$) redox couple was used to clarify whether the signal of the field-effect transducer is affected by the electron-transfer reactions (without the proton generation) at the amperometric transducer or not. The results of these experiments are summarized in Fig. 3.4. Here, the time-dependent responses of the combined amperometric/field-effect sensor simultaneously recorded at different measuring conditions are presented. The working electrode of the amperometric transducer was polarized at a potential of +0.4 V *vs.* the Ag/AgCl reference electrode related to the reduction of $[Fe(CN)_6]^{3-}$. A phosphate buffer (0.1 mM, pH 7) adjusted with 100 mM NaCl was used as electrolyte solution and stirred continuously. The pH value of the elec-

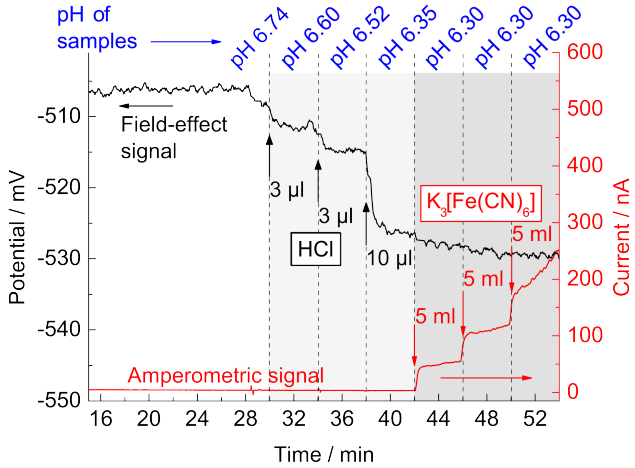

Figure 3.4: Validation of independent functioning of the one-chip integrated field-effect and amperometric transducers. The pH value of samples was controlled with a conventional pH-glass electrode, simultaneously.

trolyte solution was monitored in addition with a conventional pH-glass electrode (Metrohm).

During the start-up period of the experiment (initial 30 min), both transducers show a stable response behavior in phosphate buffer. After 30 min, 3 µL HCl was added to the electrolyte and the titration with HCl was repeated twice with titration volumes of 3 µL (34 min) and 10 µL (38 min) HCl. A total potential shift of 22 mV towards more negative potential values was observed for the field-effect device, which corresponds to a pH decrease of ΔpH$\sim$0.4. An additional analysis with a pH-glass electrode of samples drawn before and after each titration step confirmed this pH shift (see Fig. 3.4). On the contrary, the amperometric transducer shows a stable signal throughout this first part of the experiment and is therefore, not affected by the pH change of the solution.

In the next step, 5 mL of potassium hexacyanoferrate (III) ($K_3[Fe(CN)_6]$) was added to the solution (42 min, 46 min, 50 min) to stimulate redox reactions at the Pt working electrode. As expected, the amperometric transducer responds immediately with an increase of the current of about 45 nA after each addition of $K_3[Fe(CN)_6]$. At the same time, the field-effect sensor signal remains practically stable (some small changes in the ConCap response could be attributed to an intrinsic drift of the field-effect sensor), and thus, was not influenced by the current of the amperometric sensor. The results presented in Fig. 3.4 not only underline the functioning of the one-chip integrated field-effect and amperometric transducers, but also verify their independent functioning that is essential for further experiments on dissolved H_2 detection with the combined sensor chip.

3.4.3 Detection of dissolved H_2 with the combined amperometric/field-effect sensor

Fig. 3.5a demonstrates an example of a simultaneous amperometric/field-effect detection of dissolved H_2 in the concentration range from 0.05 to 3 % (v/v) H_2. The data were collected by exposing the combined sensor chip to the electrolyte

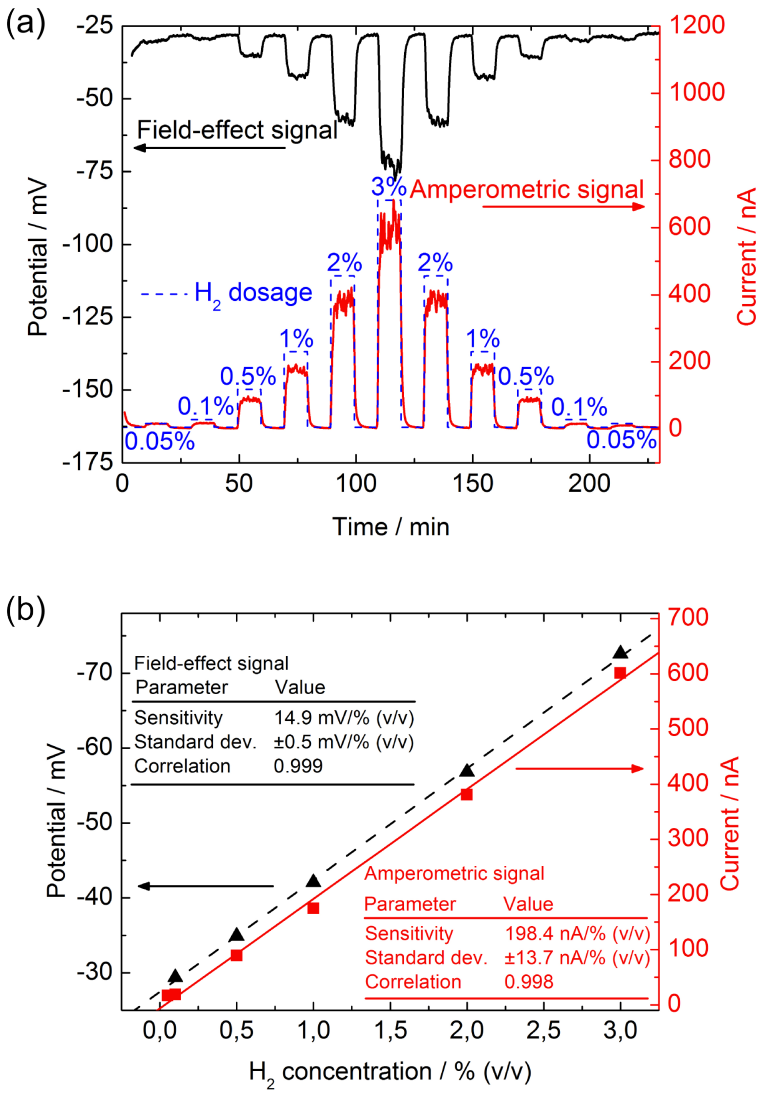

Figure 3.5: Simultaneous amperometric/field-effect detection of dissolved H_2 in the concentration range from 0.05 to 3 % (v/v) H_2 (a) and calibration curves of both the amperometric and field-effect transducer, respectively (b).

with different concentrations of dissolved H_2 for 10 min. Prior to the introduction of a new hydrogen gas mixture, the electrolyte was flushed with nitrogen in order to remove the residual content of dissolved H_2.

The amperometric sensor responded instantaneously to the H_2 dosage with a H_2 concentration-dependent increase of the output current. At the same time, the ConCap signal of the pH-sensitive field-effect sensor shifted towards more negative potentials in response to an increasing hydrogen concentration. The negative signal shift in the ConCap mode corresponds to more positive gate-surface charges as a consequence of proton generation (see Eq. 3.1) at the Pt electrode. The resulting H_2 concentration-dependent local pH decrease near the surface of the pH-sensitive layer modulates the flatband voltage and output signal of the field-effect EIS sensor. For instance, with the 1 % (v/v) H_2 dosage, the output signal of the field-effect sensor shifts about (13.5 ± 0.1) mV. Taking into account that the pH sensitivity of the Ta_2O_5-gate EIS sensor is about 57 mV/pH, this signal shift corresponds to a local pH change near the surface of the pH-sensitive layer of ΔpH$\sim$0.25.

As can be seen from Fig. 3.5a, with ascending and descending H_2 dosages, a good correlation between the ConCap response of the field-effect sensor and the output signal of the amperometric sensor has been observed. The respective calibration curves of the sensors evaluated from Fig. 3.5a are presented in Fig. 3.5b. Both the amperometric and the field-effect transducer show a linear response in the H_2 concentration range from 0.1 to 3 % (v/v) with a H_2 sensitivity of (198.4 ± 13.7) nA/% (v/v) and (14.9 ± 0.5) mV/% (v/v), respectively. The lower detection limit has been estimated to be about 0.05 % (v/v) and 0.1 % (v/v) for the amperometric and field-effect sensor, respectively. Both transducers displayed practically no hysteresis (less than 2 nA for the amperometric transducer and $\sim$0.35 mV for the field-effect device). The noticeable increase of noise in the amperometric sensor signal at high H_2 concentrations might be probably due to the rather random flow conditions at the Pt working electrode during the H_2 gassing.

Fig. 3.6 shows the amperometric and field-effect responses of the combined sensor chip to 3 % (v/v) H_2 dosage over a substantial number of measuring cycles (36 cycles). Almost identical maximum output currents of approximately 580 nA were observed for the amperometric sensor over the whole measuring period, showing the stability and reproducibility of the developed sensor. The output signal of the field-effect EIS sensor changes about 45 mV in the direction corresponding to lower pH values. Whereas the amperometric signal was very stable, a relatively small drift about 2.5 mV/h was observed for the field-effect sensor.

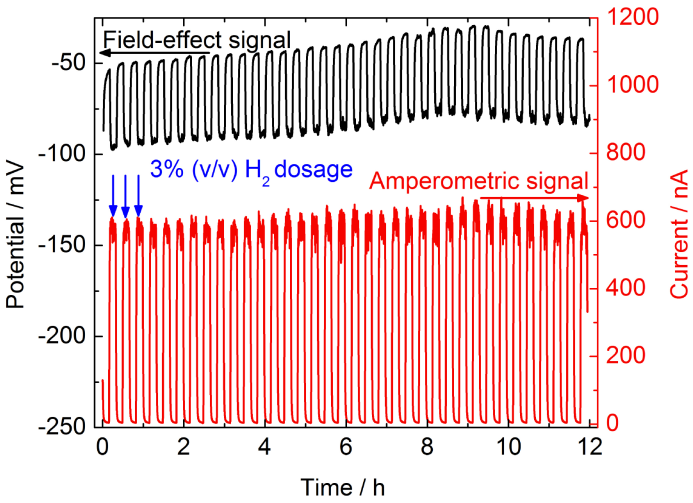

Figure 3.6: Amperometric and field-effect responses of the combined sensor chip to 3 % (v/v) H_2 dosage over a substantial number of measuring cycles (36 cycles).

3.5 Conclusions

In the present work, a one-chip integrated combined amperometric/field-effect H_2 sensor has been developed and tested in electrolyte solutions with different contents of dissolved H_2. Both the amperometric and the field-effect transducer show a linear response in the H_2 concentration range from 0.1 to 3 % (v/v) with a slope of 198.4 nA/% (v/v) and 14.9 mV/% (v/v), respectively. With increasing or decreasing H_2 dosages, a good correlation between the ConCap response of the field-effect transducer and the output signal of the amperometric transducer has been observed.

The obtained results demonstrate the independent functioning of both transducer principles on the same chip as well as the feasibility of the presented approach for a simultaneous amperometric/field-effect detection of dissolved H_2. Such a combination of two transducer principles, namely, the amperometric and field-effect, might allow a more accurate, selective and reliable measurement of dissolved H_2 in biogas reactors and can serve as an early warning indicator of digester failures.

To overcome possible problems related to the functioning of the combined sensor in real biogas broths, future work will be directed to a direct coupling of the sensor setup with a biogas reactor via a bypass system filled with a suitable buffer solution, which will be separated from the biogas medium by a H_2-permeable

membrane (of e.g., polytetrafluoroethylene). In this way, the selectivity, life-time and signal-to-noise ratio of the combined sensor can be improved. Moreover, to achieve a high output signal for the field-effect pH sensor, the bypass system can be filled with an appropriate low-capacity internal buffer solution.

3.6 Acknowledgments

The authors gratefully thank the Bundesministerium für Bildung und Forschung (BMBF, Germany) for financial support of this work (EMSiG).

3.7 Bibliography

[1] Demirbaş, A.: Biomass resource facilities and biomass conversion processing for fuels and chemicals. *Energy Conversion and Management* 42 (2001), No. 11, p. 1357–1378

[2] Cord-Ruwisch, R.; Mercz, T. I.; Hoh, C.-Y.; Strong, G. E.: Dissolved hydrogen concentration as an on-line control parameter for the automated operation and optimization of anaerobic digesters. *Biotechnology and Bioengineering* 56 (1997), No. 6, p. 626–634

[3] Weiland, P.: Biogas production: Current state and perspectives. *Applied Microbiology and Biotechnology* 85 (2010), No. 4, p. 849–860

[4] Ahring, B. K.: Perspectives for anaerobic digestion. Ahring, B. K. (Eds.): *Biomethanation I* 81. Berlin / Heidelberg: Springer, (2003). – ISBN 9783540443223, p. 1–30

[5] Archer, D. B.; Hilton, M. G.; Adams, P.; Wiecko, H.: Hydrogen as a process control index in a pilot scale anaerobic digester. *Biotechnology Letters* 8 (1986), No. 3, p. 197–202

[6] Lloyd, D.; Whitmore, T. N.: Hydrogen-dependent control of the continuous thermophilic anaerobic digestion process using membrane inlet mass spectrometry. *Letters in Applied Microbiology* 6 (1988), No. 1, p. 5–10

[7] Harper, S. R.; Pohland, F. G.: Recent developments in hydrogen management during anaerobic biological wastewater treatment. *Biotechnology and Bioengineering* 28 (1986), No. 4, p. 585–602

[8] Pauss, A.; Andre, G.; Perrier, M.; Guiot, S. R.: Liquid-to-gas mass transfer in anaerobic processes: Inevitable transfer limitations of methane and hydrogen in the biomethanation process. *Applied and Environmental Microbiology* 56 (1990), No. 6, p. 1636–1644

[9] Strong, G. E.; Cord-Ruwisch, R.: An in situ dissolved-hydrogen probe for monitoring anaerobic digesters under overload conditions. *Biotechnology and Bioengineering* 45 (1995), No. 1, p. 63–68

[10] Björnsson, L.; Hörnsten, E. G.; Mattiasson, B.: Utilization of a palladium-metal oxide semiconductor (Pd-MOS) sensor for on-line monitoring of dissolved hydrogen in anaerobic digestion. *Biotechnology and Bioengineering* 73 (2001), No. 1, p. 35–43

[11] Kuroda, K.; Gaiger Silveira, R.; Nishio, N.; Sunahara, H.; Nagai, S.: Measurement of dissolved hydrogen in an anaerobic digestion process by a membrane-covered electrode. *Journal of Fermentation and Bioengineering* 71 (1991), No. 6, p. 418–423

[12] Frigon, J.-C.; Guiot, S. R.: Impact of liquid-to-gas hydrogen mass transfer on substrate conversion efficiency of an upflow anaerobic sludge bed and filter reactor. *Enzyme and Microbial Technology* 17 (1995), No. 12, p. 1080–1086

[13] Hörnsten, E. G.; Lundström, I.; Nordberg, A.; Mathisen, B.: The use of palladium metal oxide semiconductor structures in quantitative studies of H_2 and H_2S in processes related to biogas production. *Bioprocess Engineering* 6 (1991), No. 5, p. 235–240

[14] Lloyd, D.; Scott, R. I.; Williams, T.: Membrane inlet mass spectrometry – measurement of dissolved gases in fermentation liquids. *Trends in Biotechnology* 1 (1983), No. 2, p. 60–63

[15] Sakthivel, M.: A portable limiting current solid-state electrochemical diffusion hole type hydrogen sensor device for biomass fuel reactors: Engineering aspect. *International Journal of Hydrogen Energy* 33 (2008), No. 2, p. 905–911

[16] Pauss, A.; Guiot, S. R.: Hydrogen monitoring in anaerobic sludge bed reactors at various hydraulic regimes and loading rates. *Water Environment Research* 65 (1993), No. 3, p. 276–280

[17] Pauss, A.; Samson, R.; Guiot, S. R.; Beauchemin, C.: Continuous measurement of dissolved H_2 in an anaerobic reactor using a new hydrogen/air fuel cell detector. *Biotechnology and Bioengineering* 35 (1990), No. 5, p. 492–501

[18] Kristjansson, J. K.; Schönheit, P.; Thauer, R. K.: Different K_s values for hydrogen of methanogenic bacteria and sulfate reducing bacteria: An explanation for the apparent inhibition of methanogenesis by sulfate. *Archives of Microbiology* 131 (1982), No. 3, p. 278–282

[19] Nakazato, K.: An integrated ISFET sensor array. *Sensors* 9 (2009), No. 11, p. 8831–8851

[20] Siqueira, J. R.; Abouzar, M. H.; Poghossian, A. S.; Zucolotto, V.; Oliveira, O. N.; Schöning, M. J.: Penicillin biosensor based on a capacitive field-effect structure functionalized with a dendrimer/carbon nanotube multilayer. *Biosensors and Bioelectronics* 25 (2009), No. 2, p. 497–501

[21] Lee, C.-S.; Kim, S. K.; Kim, M.: Ion-sensitive field-effect transistor for biological sensing. *Sensors* 9 (2009), No. 9, p. 7111–7131

[22] Gun, J.; Schöning, M. J.; Abouzar, M. H.; Poghossian, A. S.; Katz, E.: Field-effect nanoparticle-based glucose sensor on a chip: Amplification effect of coimmobilized redox species. *Electroanalysis* 20 (2008), No. 16, p. 1748–1753

[23] Patolsky, F.; Zheng, G.; Lieber, C. M.: Nanowire-based biosensors. *Analytical Chemistry* 78 (2006), No. 13, p. 4260–4269

[24] Poghossian, A. S.; Ingebrandt, S.; Offenhäusser, A.; Schöning, M. J.: Field-effect devices for detecting cellular signals. *Seminars in Cell & Developmental Biology* 20 (2009), No. 1, p. 41–48

[25] Mourzina, Y.; Mai, T.; Poghossian, A. S.; Ermolenko, Y.; Yoshinobu, T.; Vlasov, Y.; Iwasaki, H.; Schöning, M. J.: K^+-selective field-effect sensors as transducers for bioelectronic applications. *Electrochimica Acta* 48 (2003), No. 20-22, p. 3333–3339

[26] Huck, C.; Jolly, P.; Wagner, P.; Poghossian, A. S.; Schöning, M. J.: One-chip integrated dual amperometric/field-effect sensor for the detection of dissolved hydrogen. *Procedia Engineering* 25 (2011), p. 1161–1164

[27] Hübert, T.; Boon-Brett, L.; Black, G.; Banach, U.: Hydrogen sensors – A review. *Sensors and Actuators B: Chemical* 157 (2011), No. 2, p. 329–352

[28] Sakthivel, M.; Weppner, W.: Development of a hydrogen sensor based on solid polymer electrolyte membranes. *Sensors and Actuators B: Chemical* 113 (2006), No. 2, p. 998–1004

[29] Stetter, J. R.; Li, J.: Amperometric gas sensors – A review. *Chemical Reviews* 108 (2008), No. 2, p. 352–366

[30] Chao, Y.; Yao, S.; Buttner, W. J.; Stetter, J. R.: Amperometric sensor for selective and stable hydrogen measurement. *Sensors and Actuators B: Chemical* 106 (2005), No. 2, p. 784–790

[31] Poghossian, A. S.; Berndsen, L.; Schöning, M. J.: Chemical sensor as physical sensor: ISFET-based flow-velocity, flow-direction and diffusion-coefficient sensor. *Sensors and Actuators B: Chemical* 95 (2003), No. 1-3, p. 384–390

[32] Olthuis, W.; Luo, J.; van der Schoot, B.; Bergveld, P.; Bos, M.; van der Linden, W.: Modelling of non-steady-state concentration profiles at ISFET-based coulometric sensor – actuator systems. *Analytica Chimica Acta* 229 (1990), p. 71–81

[33] Poghossian, A. S.: The super-Nernstian pH sensitivity of Ta_2O_5-gate ISFETs. *Sensors and Actuators B: Chemical* 7 (1992), No. 1-3, p. 367–370

[34] Schöning, M. J.; Brinkmann, D.; Rolka, D.; Demuth, C.; Poghossian, A. S.: CIP (cleaning-in-place) suitable "non-glass" pH sensor based on a Ta_2O_5-gate EIS structure. *Sensors and Actuators B: Chemical* 111-112 (2005), p. 423–429

[35] Setoguchi, T.: Effects of anode material and fuel on anodic reaction of solid oxide fuel cells. *Journal of The Electrochemical Society* 139 (1992), No. 10, p. 2875–2880

[36] Jiang, S. P.: Hydrogen oxidation at the nickel and platinum electrodes on yttria-tetragonal zirconia electrolyte. *Journal of the Electrochemical Society* 144 (1997), No. 11, p. 3777–3784

[37] Luo, J.; Olthuis, W.; Bergveld, P.; Bos, M.; van der Linden, W.: Determination of buffer capacity by means of an ISFET-based coulometric sensor-actuator system with a gate-covering porous actuator. *Sensors and Actuators B: Chemical* 20 (1994), No. 1, p. 7–15

[38] Soldatkin, A.; Gorchkov, D. V.; Martelet, C.; Jaffrezic-Renault, N.: Application of charged polymeric materials as additional permselective membranes for modulation of the working characteristics of penicillin sensitive ENFETs. *Materials Science and Engineering: C* 5 (1997), No. 1, p. 35–40

[39] Yoshinobu, T.; Ecken, H.; Poghossian, A. S.; Simonis, A.; Iwasaki, H.; Lüth, H.; Schöning, M. J.: Constant-current-mode LAPS (CLAPS) for the detection of penicillin. *Electroanalysis* 13 (2001), No. 8-9, p. 733–736

[40] Cané, C.; Gràcia, I.; Merlos, A.: Microtechnologies for pH ISFET chemical sensors. *Microelectronics Journal* 28 (1997), No. 4, p. 389–405

[41] Poghossian, A. S.: Determination of the pH_{pzc} of insulators surface from capacitance-voltage characteristics of MIS and EIS structures. *Sensors and Actuators B: Chemical* 44 (1997), No. 1-3, p. 551–553

4 Metabolic responses of *Escherichia coli* upon glucose pulses captured by a capacitive field-effect sensor

Christina Huck[a,b], Johannes Schiffels[a], Cony N. Herrera[a], Maximilian Schelden[a], Thorsten Selmer[a], Arshak Poghossian[a,b], Marcus E.M. Baumann[a], Patrick Wagner[a], Michael J. Schöning[a,b]

[a] *Institute of Nano- and Biotechnologies (INB), FH Aachen, Jülich, Germany*

[b] *Peter Grünberg Institute (PGI-8), Forschungszentrum Jülich GmbH, Jülich, Germany*

[c] *Institute for Materials Research (IMO), Hasselt University, Diepenbeek, Belgium*

Published in: *Physica Status Solidi A: Applications and Materials Science*, Vol. 210, pp. 926–931, 2013, DOI: 10.1002/pssa.201200900

Submitted: 2012-10-25; Accepted: 2013-04-08; Published: 2013-05-06

4.1 Abstract

Living cells are complex biological systems transforming metabolites taken up from the surrounding medium. Monitoring the responses of such cells to certain substrate concentrations is a challenging task and offers possibilities to gain insight into the vitality of a community influenced by the growth environment. Cell-based biosensors represent a promising platform for monitoring the metabolic activity and thus, the "vitality" of relevant organisms. In the present study, metabolic responses of the model bacterium *Escherichia coli* in suspension, layered onto a capacitive field-effect structure, were examined to pulses of glucose in the concentration range between 0.05 and 2 mM. It was found that acidification of the surrounding medium takes place immediately after glucose addition and follows Michaelis-Menten kinetic behavior as a function of the glucose concentration. In future, the presented setup can, therefore, be used to study substrate specificities on the enzymatic level and may as well be used to perform investigations of more complex metabolic responses. Conclusions and perspectives highlighting this system are discussed.

4.2 Introduction

Applications for biosensors employing living cells are widespread in different scientific fields. Such sensors may be used in drug screening, cell-growth observations, environmental monitoring as well as for fundamental research of physiological processes (see e.g., recent review [1] and references there). Considerable research efforts have been devoted to the development of light-addressable potentiometric sensors (LAPS) [2–5] and ion-sensitive field-effect transistors (ISFET) [6] for cellular metabolism and extracellular acidification measurements. In contrast to ISFETs, field-effect capacitive electrolyte-insulator-semiconductor (EIS) sensors are simple in layout, easy and cost-effective in fabrication and usually, no photolithographic process steps or complicated encapsulation procedures are required in case of the capacitive field-effect structure [7–11]. Usually, a simple O-ring is sufficient for the electrical isolation of the sensor chip from the aqueous solution.

In this work, metabolic responses of the model bacterium *Escherichia coli* (*E. coli*) in suspension, layered onto a capacitive field-effect sensor, were examined to pulses of glucose. The gram-negative metabolically versatile model bacterium *E. coli* displays a promising biological system to study cellular responses to substrate pulses or changing environmental conditions. Such responses can be monitored when rapidly convertible molecules such as glucose are added to a suspension culture of vital cells, since their consumption results in an acidification of the surrounding medium [6, 12, 13]. Using a capacitive field-effect sensor, this pH change can be monitored online, allowing detailed metabolic studies or simply the use of the system as a device that measures given glucose concentrations in unknown samples.

Since glucose is the most important carbon and energy source, the genes for the responsible enzyme machinery are constitutively expressed and, consequently, immediately venturous. Before entering glycolysis, glucose is actively transported into the cells by a group-translocating system called phosphotransferase system (PTS) [14, 15]. PTS converts glucose to glucose-6-phosphate (G-6-P) and, thereby, ensures that active transport is possible even towards a concentration gradient. The following glycolysis breaks down G-6-P to pyruvate, which yields two moles of the cell's energy carrier adenosine triphosphate (ATP) per mol glucose. Under aerobic conditions, the Krebs cycle and subsequently, the respiration chain ensures complete oxidation of the carbon to carbon dioxide (CO_2), reoxidizes the reducing equivalents ($NADH/H^+$) and yields the predominant energy fraction for the cell. However, under oxygen limitation *E. coli* switches to fermentation in order to reoxidize the reducing equivalents and partly to regain energy [16–19]. The fastest way for the cell to do so is by reduction of pyruvate to lactate, which is readily excreted. Since *E. coli* is a mixed acid fermenting

bacterium, ethanol, acetate and even formiate may be formed. However, under oxygen limitation and especially under overflow conditions, the acetate branch is the predominant one, since pyruvate is almost completely converted to the acetyl coenzyme A (acetyl-CoA). With oxygen being limited, acetyl-CoA does not enter the Krebs cycle and energy regeneration is only ensured via conversion to acetyl-phosphate and finally, to acetate [20–28]. Under these conditions, acetate and lactate are directly excreted and acidify the surrounding medium. This advantage was exploited in the present study: A cell suspension (unpurged) always runs rapidly out of oxygen, which is poorly soluble in water. Consequently, glucose added to the cells is entirely subjected to fermentation, yielding two moles of acid per mol of glucose. Taking benefit of this correlation, key parameters for a glucose sensor setup were determined. Optimum scopes for the glucose start concentration and the cell number were examined and correlations between the cell number, acidification rate, substrate concentration, surface potential and acidification time were established. It is evident from our data that these parameters correlate with the applied glucose concentration and can, therefore, be used for determination of the compound level in general. In view of the presented results, the setup might as well be exploited in future experiments to gain insight into substrate specificities.

4.3 Experimental

4.3.1 Functioning principle of a cell-based capacitive field-effect sensor

The structure and operation principle of the biosensor is shown in Fig. 4.1a. The developed pH-sensitive field-effect sensor consists of a p-Si-SiO_2-Ta_2O_5 (p-Si,

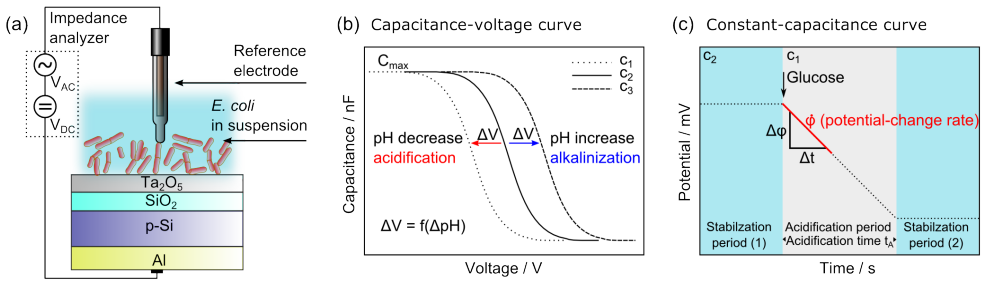

Figure 4.1: Structure and operation principle of the capacitive field-effect sensor setup with *E. coli* suspension on the sensor surface (a), schematic capacitive-voltage curve of the EIS in dependence of different substrate concentrations (b) and constant-capacitance curve (c).

$\rho = 10\,\Omega\,\text{cm}$; 30 nm thermally grown SiO_2, 60 nm Ta_2O_5) structure. Information about the fabrication process can be found elsewhere [29, 30]. A suspension of exponentially grown *E. coli* cells in Tris-buffered saline (TBS, pH 7.2) buffer is layered onto the sensor surface. The operation principle of the cell-based sensor is as follows: The pH-sensitive transducer material (here: Ta_2O_5) detects variations in the H^+-ion concentration. The resulting local pH decrease near the surface of the Ta_2O_5 layer changes the surface potential of Ta_2O_5 and thus, modulates the space-charge capacitance in the Si and consequently, the flat-band voltage and the capacitance of the EIS structure. This results in a pH-dependent shift (ΔV) of the capacitance-voltage (C-V) curve along the voltage axis (see Fig. 4.1b). As stated before, the proton accumulation correlates with the metabolism of *E. coli*, which is a nonlinear biochemical response evaluated in this study using different parameters.

4.3.2 Measurement setup and data acquisition

For sensor operation, a DC polarization voltage (V_{DC}) is applied via a reference electrode (conventional liquid-junction Ag/AgCl electrode, Metrohm) and a rear-side contact. V_{DC} creates a depletion region inside the semiconductor. The width of this depletion region is additionally influenced by the sensor surface potential φ, which depends on the local concentration of H^+ ions. A small AC voltage (V_{AC}) with an amplitude of 20 mV and a frequency of 120 Hz is superimposed in order to measure the capacitance of the sensor. The realized p-Si-SiO_2-Ta_2O_5 capacitive field-effect structure has been characterized using a cell suspension with different glucose concentrations by means of C-V and constant capacitance (ConCap) methods using an impedance analyzer (Zahner Elektrik; see Fig. 4.1a-c). The ConCap mode allows a dynamic characterization of the field-effect EIS sensor. In this mode, the capacitance of the EIS sensor is kept constant (usually within the depletion region of the C-V curve at ∼60 % of the maximum capacitance) using a feedback-control circuit, and potential changes at the transducer/electrolyte interface are directly monitored.

For the measurements, four field-effect sensors from one wafer were mounted into a home-made measuring cell in parallel, contacted on their front sides by electrolyte and a combined reference electrode, and on their rear sides by four gold-plated pins. The side walls and backside contacts of the field-effect sensors were protected from the electrolyte solution by means of an O-ring, thereby circumventing the need for a complex encapsulation process. The contact area of each sensor with the cell suspension amounted to 37.5 mm^2. All measurements were performed in a dark Faraday cage at room temperature. For the measuring procedure, a volume of 2 mL was applied to the four EIS surfaces and the sensor-output signal was recorded in the ConCap mode for several minutes until the

sensor signal stabilized (see stabilization period (1) in Fig. 4.1c). Subsequently, the desired glucose pulse was added to the cell suspension. This leads to an immediate production of extracellular protons and, therefore, to a pH drop over time. This period is referred to as the acidification period (Fig. 4.1c) and is followed by a second stabilization period (2) at the point of glucose consumption or metabolic stagnancy, respectively.

4.3.3 Extracellular acidification rate and data analysis

As introduced *vide supra*, the extracellular acidification rate displays the immediate response of the cell collective to glucose consumption via excretion of acidic waste products. The acidification rate indicates the amount of H^+ ions produced on average per cell and per second. By determining the potential-change rate $\dot{\varphi}$ ($\dot{\varphi} = \Delta\varphi/\Delta t$; see Fig. 4.1c), the acidification rate can be calculated according to Refs. [31, 32]. For determination of the acidification rate α, the potential-change rate $\dot{\varphi}$, the Avogadro constant N_A, the specific pH-buffer capacity β (0.7 mM/pH for TBS), the volume V (2 mL) of the suspension, the pH sensitivity S (58 mV/pH) and the cell number n are required. Eq. 4.1 highlights the relation between the potential-change rate $\dot{\varphi}$ and the acidification rate α.

$$\alpha = \varphi \frac{N_A \beta V}{Sn} \tag{4.1}$$

The potential-change rate $\dot{\varphi}$ within the acidification period was estimated by linear regression during the first 10 min as schematically represented in Fig. 4.1c. This procedure was applied on the basis that the correlation between α and the glucose concentration follows Michaelis-Menten kinetics, which accounts for the measurement of initial maximum velocities. Apart from the acidification rate α, an additional parameter is introduced: The time between stabilization period (1) and stabilization period (2), referred to as acidification period, is termed acidification time t_A (see Fig. 4.1c).

4.3.4 Preparation of cells and buffers

All measurements in this study were performed using *E. coli* strain K12. For cell preparation, 50 mL M9-minimal medium[1] supplemented with 1 mM thiamine, 50 µM $FeSO_4$, 1 mg L^{-1} pantothenate and 20 mM glucose in 500 mL baffled flasks were inoculated 1:100 with an overnight culture in the same medium and grown for 12 – 16 h at 37 °C and 300 rpm. Cells were harvested at the point when the

[1] M9-minimal medium is a culture medium for microorganisms that contains the minimal necessities for growth. It basically contains a carbon source (in this case glucose), inorganic salts, and water.

culture attained an optical density ($OD_{600\,\mathrm{nm}}$) of 0.4 – 0.8 (exponential growth phase). For harvesting, cells were pelleted (16.000 g, 1 min), washed twice with TBS and resuspended in the appropriate volume of TBS to reach the desired OD. During exponential growth, an OD of 1 corresponds to a cell number of 1×10^9 cells mL^{-1}, a correlation used throughout the study. Resuspended cells were either used directly for sensor measurements or stored for up to 8 h in the fridge without loss of activity. A glucose stock solution (200 mM) was prepared with TBS. All buffers and substrates were purged with N_2 before usage to remove dissolved oxygen.

4.4 Results and discussion

Glucose uptake and catabolism in living cells is a biochemical cascade involving a battery of enzymes. Consequently, a response in form of an acidification is a kinetically intricate phenomenon, depending on several factors. As a first approximation, the system can be described as multiple-coupled enzyme catalysis with one or more steps being rate-limiting. The glycolytic enzymes, however, are constitutively produced and capable of converting G-6-P at maximum rate even when trace levels of cytosolic substrate are present. It has been demonstrated, that the rate limiting-step in this cascade is the glucose uptake system, namely the PTS [33]. Evolutionarily justified, this could be mainly due to the fact that organisms have to cope with low substrate concentrations rather than exuberance in their native habitats.

Figure 4.2 exemplarily depicts a typical dynamic ConCap response recorded with a cell-based capacitive field-effect sensor. After a stabilization time of 10 min, glucose was added to the cell suspension on the sensor surface. Upon substrate pulsing indicated by the black arrow, an immediate acidification was observed. Following an initial maximum velocity, the acidification rate decreases and finally disperses at the point of glucose consumption (second stabilization period).

Applying different glucose concentrations in the range between 0.05 – 2 mM, it was found that the initial maximum acidification rate α follows Michaelis-Menten kinetic behavior as a function of the glucose concentration as depicted in Fig. 4.3a. For calculation of the kinetic parameters, data were additionally plotted in the double-reciprocal Lineweaver-Burk plot in Fig. 4.3b. The two characteristic values, which can be obtained, are the maximum acidification rate α_{max} and the Michaelis constant K_{M} that is the substrate concentration at which the reaction rate is half of α_{max}. K_{M} values of 0.22 mM (Hill-Fit; dashed line; Fig. 4.3a) and 0.27 mM (linear fit; dashed line; Fig. 4.3b) were obtained, which is in good agreement with the values previously reported for enzyme II (EII^{Glc}) of the PTS glucose permease of *E. coli* (0.22 mM) [34]. These data are consistent with the earlier presumption

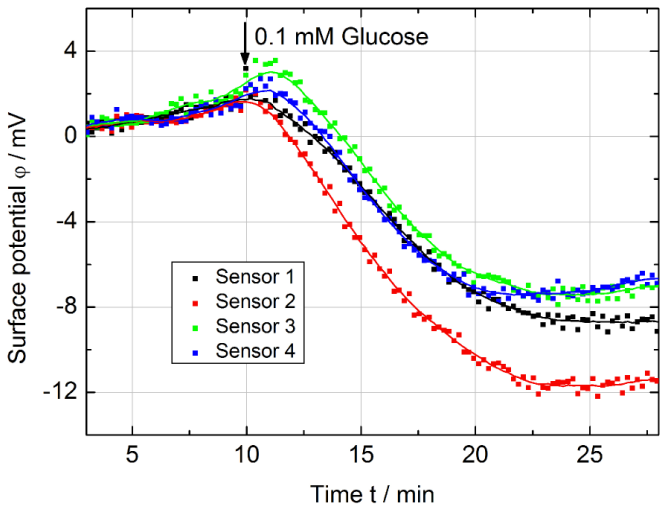

Figure 4.2: Dynamic ConCap response of all four sensors with 1×10^9 cells mL^{-1} in TBS. After a stabilization time of 10 min, 0.1 mM glucose was added to *E. coli* in suspension indicated by the black arrow.

that the PTS is the rate-limiting enzyme in glucose fermentation and that further breakdown of G-6-P after translocation into the cytoplasm proceeds at maximum velocity [33].

A second parameter for possible calibration of the potential glucose sensor is the acidification time t_A (see Fig. 4.1) as a function of the glucose concentration. The acidification time is calculated from the initial point of glucose addition to the point where the slope slabs, determined by using the first derivative of the surface-potential change-rate $\dot{\varphi}$. Using the same experimental data set, the relation between acidification time and glucose concentration is presented in Fig. 4.4. The acidification time prolongs with increasing glucose concentration. This is explainable as follows: While the acidification rate α is calculated from the initial potential-change rate $\dot{\varphi}$ and, consequently, displays the maximum activity of the PTS, the acidification time is a function of the glucose concentration as well as the pH. The pH value drops during the measurement, thereby increasingly inhibiting the biological activity. At the same time, substrate levels subside, which further slows down the uptake rate. This inhibition might be demonstrated on the basis of our data: For a glucose concentration of 2 mM, an acidification rate α of approximately 81×10^4 H$^+$ s^{-1} cell^{-1} was determined (see Fig. 4.3a), which corresponds to 4.86×10^4 H$^+$ min^{-1} cell^{-1}. Hence, for a cell density of 1×10^9 cells mL^{-1} and a volume of 2 mL as usually applied, 9.72×10^{16} H$^+$ min^{-1} are generated. Fur-

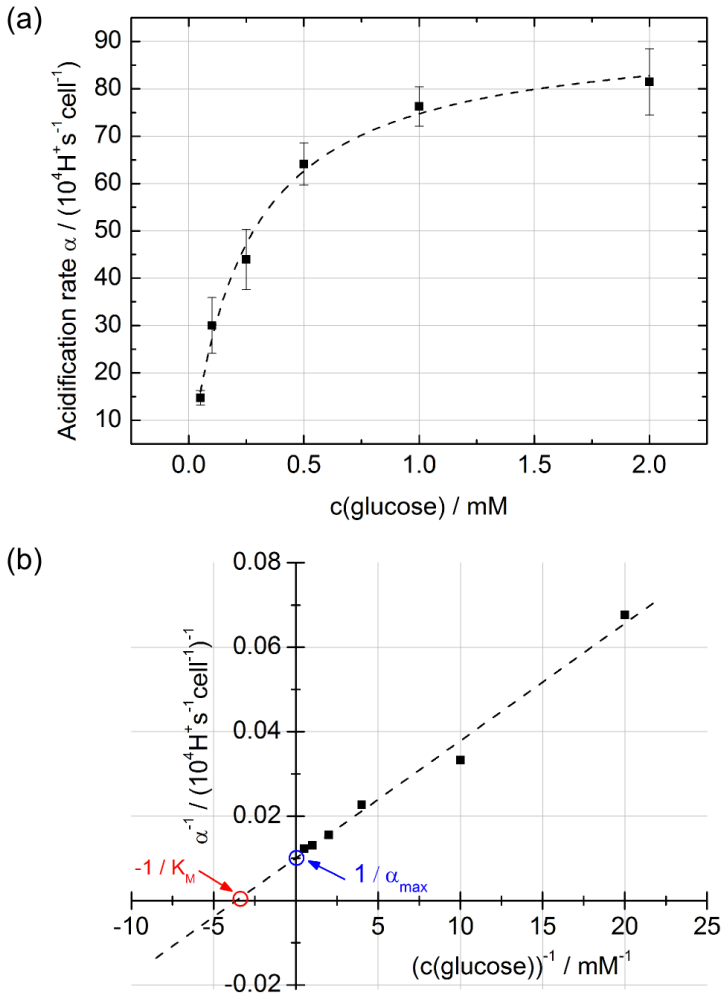

Figure 4.3: Acidification rate α (mean value of all four sensors; calculated by Eq 4.1.) as a function of the glucose concentration follows Michaelis-Menten kinetic model (a), and corresponding double-reciprocal Lineweaver-Burk plot (b). The error bars in (a) specify the standard deviation of the four sensors and the dashed lines indicate the Hill-Fit and the linear fit, respectively. For the experiment, a cell number of 1×10^9 cells mL^{-1} was used.

thermore, a glucose concentration of 2 mM in 2 mL suspension yields 2.41×10^{18} glucose molecules. Assuming a production of two protons for each glucose molecule, 4.82×10^{18} H^+ are theoretically produced. These assumptions allow a comparison between the expected acidification time with the experimental acidification time. For this, 4.82×10^{18} H^+ is divided by 9.72×10^{16} H^+ min^{-1}.

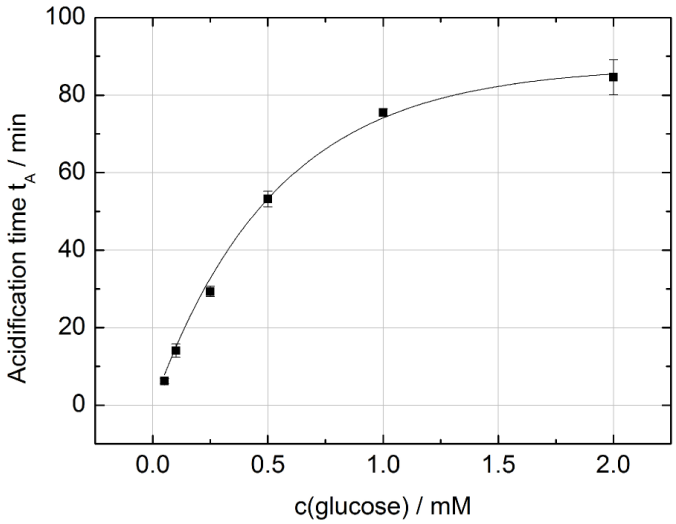

Figure 4.4: Acidification time t_A as a function of the glucose concentration of the data presented in Fig. 4.3. The acidification time increases asymptotically with the glucose concentration. For the experiment a cell number of 1×10^9 cells mL^{-1} was used. The error bars indicate the standard deviation of the four sensors.

Thus, the cells should theoretically consume the glucose within 50 min, while an acidification time t_A of 87 min was determined. This discrepancy demonstrates that the acidification time is a function of α, capturing not only the initial maximum activity but also its decrease over time resulting from a shift towards more unfavorable conditions. Furthermore, as depicted in Fig. 4.2, there is no sharp transition from the acidification period to the stabilization period (2) as introduced in Fig. 4.1c. This could lead to an inaccurate determination of the acidification time. As expected, both acidification rate α and acidification time t_A strongly depend on the number of cells present in the suspension. For convenience, regular determinations of both parameters were performed using 1×10^9 cells mL^{-1} ($OD_{600\,\mathrm{nm}} = 1$). However, we investigated the influence of different cell numbers on both α and t_A and found remarkable correlations in a range of 0.5 cells mL^{-1} to 3×10^9 cells mL^{-1}. The acidification rate follows a saturated fit behavior, while the acidification time values may be correlated using an exponential decay-like fit, which in both cases points to an inhibiting factor. This may be explained by the following two considerations: Higher cell numbers lead to a higher pH change in the surrounding medium. Consequently, the pH value of the medium distinctively differs from physiological conditions. As a result, the enzyme activity is naturally

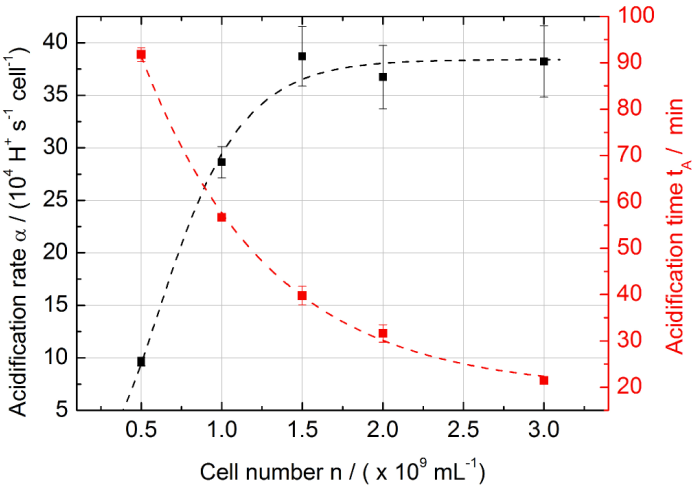

Figure 4.5: Correlation between the acidification rate α as well as the acidification time t_A and the cell number. The error bars indicate the standard deviation of the four sensors.

inhibited affecting the acidification rate as well as the acidification time, which is a function of α. Bearing in mind that the cell suspension is a non-stirred solution, a higher cell number increases the contingency of aggregation, which might affect or disturb the diffusion or substrate molecules to reach the underlying cell layer (directly on the chip surface). This inhibition might as well affect both the maximum acidification rate and the acidification time (Fig. 4.5). Another interesting phenomenon with regard to metabolic control mechanisms by cells was observed when the monitoring of the potential-change rate $\dot{\varphi}$ was prolonged beyond the second stabilization time (stabilization period (2) in Fig. 4.1c). At this stage, glucose is entirely consumed and the waste product acetate is present in significant concentrations. We observed that after a sufficient time period, a realkalinization to almost the original pH took place, although at significantly lower $\dot{\varphi}$ than the acidification (data not shown). This is explainable by the fact that *E. coli* is able to reutilize acetate via a glyoxylate cycle, provided the cells are adapted, which takes minutes to hours depending on the concentration of acetate. This finding is in agreement with earlier publications [35] and clearly opens up the possibility to use the same sensor setup for future experiments regarding the measurement of acetate and a wide range of different substrates utilizable by certain organisms.

4.5 Conclusions and outlook

The present study displays the capabilities of a field-effect sensor applied to basic metabolic studies. This was demonstrated using an on-chip suspension of *E. coli*, a well-studied model bacterium. Upon addition of defined concentrations of glucose in an oxygen-limited setup, immediate acidification of the surrounding buffer occurred, which was monitored by the sensor. Correlations between cell number, glucose concentration, acidification rate and duration of the latter were clearly demonstrated to follow nonlinear complex biochemical behavior. Careful evaluation determined the correlation between initial acidification rate and glucose concentration to mimic enzyme kinetics of highly specific glucose uptake system of *E. coli*.

In future studies, this direct enzymatic correlation might clearly be exploited to adapt this setup to different substrates as well as different organisms. Since substrates such as lactose, which require an additional hydrolytic step, are expected to lead to a more complex response captured by the sensor, the setup employed might open up possibilities to create substrate-, concentration- as well as cell-specific fingerprints in form of an acidification behavior. Examples of other organisms and nutrient combinations are described in Ref. [12]. Cell-based capacitive field-effect sensors in general might as well be applied to cell-growth observations and fermentation processes in the field of food or pharmaceutical industry. Their sensitivity to different nutrients as well as inhibiting substances that are affecting the metabolic activity might serve as an overall indicator to define the status of fermentation processes. Likewise, the vitality of microbial consortia present in highly sensitive syntrophic communities, like biogas fermenters could be monitored with such a setup by simply adding a complex substrate to a portion of withdrawn reactor content. Studies highlighting these issues are currently underway.

4.6 Acknowledgments

The authors thank the Bundesministerium für Bildung und Forschung for financial support of the project "EMSiG".

4.7 Bibliography

[1] Poghossian, A.; Ingebrandt, S.; Offenhäusser, A.; Schöning, M. J.: Field-effect devices for detecting cellular signals. *Seminars in Cell & Developmental Biology* 20 (2009), No. 1, p. 41–48

[2] Owicki, J. C.; Bousse, L. J.; Hafeman, D. G.; Kirk, G. L.; Olson, J. D.; Wada,

H. G.; Parce, J. W.: The light-addressable potentiometric sensor: Principles and biological applications. *Annual Review of Biophysics and Biomolecular Structure* 23 (1994), No. 1, p. 87–114

[3] Hafner, F.: Cytosensor® Microphysiometer: Technology and recent applications. *Biosensors and Bioelectronics* 15 (2000), No. 3-4, p. 149–158

[4] Werner, C. F.; Groebel, S.; Krumbe, C.; Wagner, T.; Selmer, T.; Yoshinobu, T.; Baumann, M. E. M.; Keusgen, M.; Schöning, M. J.: Nutrient concentration-sensitive microorganism-based biosensor. *Physica Status Solidi A* 209 (2012), No. 5, p. 900–904

[5] Wagner, T.; Molina, R.; Yoshinobu, T.; Kloock, J. P.; Biselli, M.; Canzoneri, M.; Schnitzler, T.; Schöning, M. J.: Handheld multi-channel LAPS device as a transducer platform for possible biological and chemical multi-sensor applications. *Electrochimica Acta* 53 (2007), No. 2, p. 305–311

[6] Castellarnau, M.; Zine, N.; Bausells, J.; Madrid, C.; Juárez, A.; Samitier, J.; Errachid, A.: ISFET-based biosensor to monitor sugar metabolism in bacteria. *Materials Science and Engineering C* 28 (2008), No. 5-6, p. 680–685

[7] Mourzina, Y.; Mai, T.; Poghossian, A.; Ermolenko, Y.; Yoshinobu, T.; Vlasov, Y.; Iwasaki, H.; Schöning, M. J.: K^+-selective field-effect sensors as transducers for bioelectronic applications. *Electrochimica Acta* 48 (2003), No. 20-22, p. 3333–3339

[8] Siqueira, J. R.; Abouzar, M. H.; Poghossian, A.; Zucolotto, V.; Oliveira, O. N.; Schöning, M. J.: Penicillin biosensor based on a capacitive field-effect structure functionalized with a dendrimer/carbon nanotube multilayer. *Biosensors and Bioelectronics* 25 (2009), No. 2, p. 497–501

[9] Gun, J.; Schöning, M. J.; Abouzar, M. H.; Poghossian, A.; Katz, E.: Field-effect nanoparticle-based glucose sensor on a chip: Amplification effect of coimmobilized redox species. *Electroanalysis* 20 (2008), No. 16, p. 1748–1753

[10] Poghossian, A.; Ingebrandt, S.; Abouzar, M. H.; Schöning, M.: Label-free detection of charged macromolecules by using a field-effect-based sensor platform: Experiments and possible mechanisms of signal generation. *Appl Phys A (Applied Physics A)* 87 (2007), No. 3, p. 517–524

[11] Poghossian, A.; Abouzar, M. H.; Amberger, F.; Mayer, D.; Han, Y.; Ingebrandt, S.; Offenhäusser, A.; Schöning, M.: Field-effect sensors with charged macromolecules: Characterisation by capacitance–voltage, constant-capacitance,

impedance spectroscopy and atomic-force microscopy methods. *Biosensors and Bioelectronics* 22 (2007), No. 9-10, p. 2100–2107

[12] Solé, M.; Rius, N.; Lorén, J. G.: Rapid extracellular acidification induced by glucose metabolism in non-proliferating cells of *Serratia marcescens*. *International Microbiology* 3 (2000), No. 1, p. 39–43

[13] Yoshinobu, T.; Ecken, H.; Ismail, A. M.; Iwasaki, H.; Lüth, H.; Schöning, M. J.: Chemical imaging sensor and its application to biological systems. *Electrochimica Acta* 47 (2001), No. 1-2, p. 259–263

[14] Deutscher, J.; Francke, C.; Postma, P. W.: How phosphotransferase system-related protein phosphorylation regulates carbohydrate metabolism in bacteria. *Microbiology and Molecular Biology Reviews* 70 (2006), No. 4, p. 939–1031

[15] Tchieu, J.; Norris, V.; Edwards, J.; Saier, M.: The complete phosphotransferase system in *Escherichia coli*. *Journal of Molecular Microbiology and Biotechnology* 3 (2001), No. 3, p. 329–346

[16] Holms, W. H.: Flux analysis and control of the central metabolic pathways in *Escherichia coli*. *FEMS Microbiology Reviews* 19 (1996), No. 2, p. 85–116

[17] Partridge, J. D.: *Escherichia coli* transcriptome dynamics during the transition from anaerobic to aerobic conditions. *Journal of Biological Chemistry* 281 (2006), No. 38, p. 27806–27815

[18] Partridge, J. D.; Sanguinetti, G.; Dibden, D. P.; Roberts, R. E.; Poole, R. K.; Green, J.: Transition of *Escherichia coli* from aerobic to micro-aerobic conditions involves fast and slow reacting regulatory components. *Journal of Biological Chemistry* 282 (2007), No. 15, p. 11230–11237

[19] Stokes, J. L.: Fermentation of glucose by suspensions of *Escherichia coli*. *Journal of Bacteriology* 57 (1949), No. 2, p. 147–158

[20] El-Mansi, E. M. T.; Holms, W. H.: Control of carbon flux to acetate excretion during growth of *Escherichia coli* in batch and continuous cultures. *Journal of General Microbiology* 135 (1989), No. 11, p. 2875–2883

[21] El-Mansi, E. M. T.: Flux to acetate and lactate excretions in industrial fermentations: physiological and biochemical implications. *Journal of Industrial Microbiology & Biotechnology* 31 (2004), No. 7, p. 295–300

[22] Han, K.; Lim, H. C.; Hong, J.: Acetic acid formation in *Escherichia coli* fermentation. *Biotechnology and Bioengineering* 39 (1992), No. 6, p. 663–671

[23] Luli, G.; Strohl, W. R.: Comparison of growth, acetate production, and acetate inhibition of *Escherichia coli* strains in batch and fed-batch fermentations. *Applied and Environmental Microbiology* 56 (1990), No. 4, p. 1004–1011

[24] Veit, A.; Polen, T.; Wendisch, V. F.: Global gene expression analysis of glucose overflow metabolism in *Escherichia coli* and reduction of aerobic acetate formation. *Applied Microbiology and Biotechnology* 74 (2007), No. 2, p. 406–421

[25] Vemuri, G. N.; Altman, E.; Sangurdekar, D. P.; Khodursky, A. B.; Eiteman, M. A.: Overflow metabolism in *Escherichia coli* during steady-state growth: transcriptional regulation and effect of the redox ratio. *Applied and Environmental Microbiology* 72 (2006), No. 5, p. 3653–3661

[26] Xu, B.; Jahic, M.; Blomsten, G.; Enfors, S.-O.: Glucose overflow metabolism and mixed-acid fermentation in aerobic large-scale fed-batch processes with *Escherichia coli*. *Applied Microbiology and Biotechnology* 51 (1999), No. 5, p. 564–571

[27] Xu, B.; Jahic, M.; Enfors, S.-O.: Modeling of overflow metabolism in batch and fed-batch cultures of *Escherichia coli*. *Biotechnology Progress* 15 (1999), No. 1, p. 81–90

[28] Yang, Y.-T.; Bennett, G. N.; San, K.-Y.: The effects of feed and intracellular pyruvate levels on the redistribution of metabolic fluxes in *Escherichia coli*. *Metabolic Engineering* 3 (2001), No. 2, p. 115–123

[29] Schöning, M. J.; Brinkmann, D.; Rolka, D.; Demuth, C.; Poghossian, A.: CIP (cleaning-in-place) suitable “non-glass” pH sensor based on a Ta_2O_5-gate EIS structure. *Sensors and Actuators B* 111-112 (2005), p. 423–429

[30] Poghossian, A.; Malzahn, K.; Abouzar, M. H.; Mehndiratta, P.; Katz, E.; Schöning, M. J.: Integration of biomolecular logic gates with field-effect transducers. *Electrochimica Acta* 56 (2011), No. 26, p. 9661–9665

[31] Owicki, J. C.; Parce, J. W.: Biosensors based on the energy metabolism of living cells: The physical chemistry and cell biology of extracellular acidification. *Biosensors and Bioelectronics* 7 (1992), No. 4, p. 255–272

[32] Werner, C. F.; Krumbe, C.; Schumacher, K.; Groebel, S.; Spelthahn, H.; Stellberg, M.; Wagner, T.; Yoshinobu, T.; Selmer, T.; Keusgen, M.; Baumann, M. E. M.; Schöning, M. J.: Determination of the extracellular acidification of *Escherichia coli* by a light-addressable potentiometric sensor. *Physica Status Solidi A* 208 (2011), No. 6, p. 1340–1344

[33] Herbert, D.; Kornberg, H.: Glucose transport as rate-limiting step in the growth of *Escherichia coli* on glucose. *Biochemical Journal* 156 (1976), No. 2, p. 477–480

[34] García-Alles, L. F.; Zahn, A.; Erni, B.: Sugar recognition by the glucose and mannose permeases of *Escherichia coli*. Steady-state kinetics and inhibition studies. *Biochemistry* 41 (2002), No. 31, p. 10077–10086

[35] Wolfe, A. J.: The acetate switch. *Microbiology and Molecular Biology Reviews* 69 (2005), No. 1, p. 12–50

[36] Fukui, S.; Tanaka, A.: Immobilized microbial cells. *Annual Review of Microbiology* 36 (1982), No. 1, p. 145–172

[37] Yankov, D.: Diffusion of glucose and maltose in polyacrylamide gel. *Enzyme and Microbial Technology* 34 (2004), No. 6, p. 603–610

[38] Eitinger, T.; Fuchs, G.; Schlegel, H. G.: *Allgemeine Mikrobiologie*. Stuttgart: Thieme, (2007). – ISBN 9783134446081

4.8 Supporting information

In the present study, metabolic responses of the model bacterium *E. coli* in suspension, layered onto a capacitive field-effect structure, were examined to pulses of glucose. As mentioned in Section 1.3.2, the monitoring of metabolic activity also involves the identification of relevant organisms of the biogas production process. Within the Institute of Nano- and Biotechnologies at the Aachen University of Applied Sciences research activities were conducted in recent years in the field of quantification of organisms relating to environmental conditions and performance of the biogas production process. Due to the syntrophic and complex interrelation of microorganisms, none of the organisms involved can fulfill its function without the partner of the other group. The versatile model bacterium *E. coli* can be easily cultivated and, more importantly, is able to metabolize selectively acetate, which is a relevant intermediate produced during anaerobic digestion. For further exploitation of the cell-based sensor, *E. coli* was immobilized directly on the Ta_2O_5-sensor surface. For the realization of differential-mode measurements, a measuring cell was designed capable of holding four EIS sensor chips at the same time. The metabolic responses of *E. coli* towards glucose as well as acetate were studied.

4.8.1 Immobilization of microorganisms

In order to determine the acidification rate over time, it is necessary to fix the microbes on the sensor surface. In this study, the performance of *E. coli* immobilized by gel entrapment on the Ta_2O_5 surface was examined. This immobilization technique is widely used if cells are not growing adherently such as many bacteria [36]. The distinct interest in this technique is a result of its undoubted advantages in contrast to other immobilization techniques, such as controllable pore size, no need for reactive groups for the attachment to an insoluble support and high residual cellular activity [37]. Selecting an appropriate gel matrix, the gel thickness, the complete coverage of the gel on the sensor surface, the nutrient transport through the gel as well as the long-term stability of the gel were taken into consideration. As gel matrix a polyacrylamide (PAA) gel with a composition specified in Table 4.1 was chosen. In a test phase, the ratio of acrylamide and bisacrylamide as well as the concentrations of the radical initiators ammonium persulfate (APS) and tetramethylethylenediamine (TEMED) were varied and optimized. The aim of this study was to obtain a layer as thin as possible to ensure a sufficient mass transport of substrates and products. Microscopic observations in Fig. 4.6 affirm that the gel matrix is a survivable habitat for *E. coli*.

Table 4.1: Optimized composition of the polyacrylamide gel for immobilization of microorganisms on the Ta_2O_5 surface of the sensor chip.

Components	Volume (µL)
Mircoorganisms in tris-buffered saline (TBS; pH 7.2)	80.0
Acrylamide : Bisacrylamide (ratio 37.5 : 1.0)	10.0
Ammonium persulfate (APS)	5.6
Tetramethylethylenediamine (TEMED)	4.4

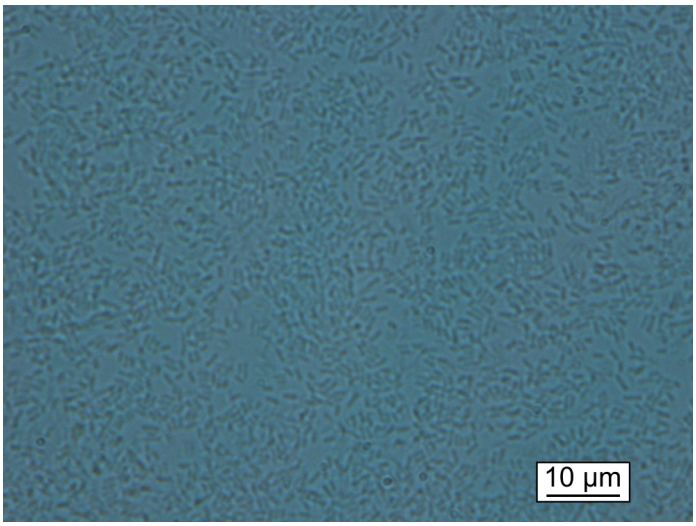

Figure 4.6: Microscopic picture of *E. coli* K-12 in polyacrylamide gel.

4.8.2 Differential measurement setup

For experiments, a measurement cell was designed to perform differential-mode measurements of up to four pH-sensitive field-effect sensors with one reference electrode in parallel. In Fig. 4.7, a schematic cross section of the measurement cell and the differential-mode setup is shown. Thus, differential measurements can be obtained between active sensors with immobilized cells and reference sensors without cells. The aim of obtaining differential signals is to reduce

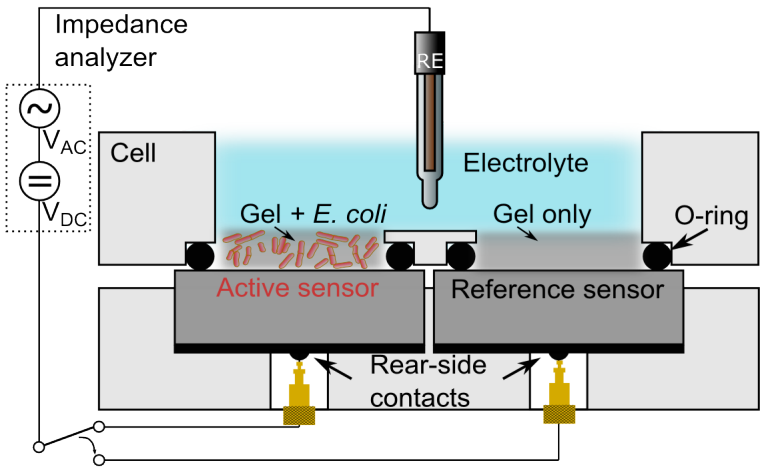

Figure 4.7: Schematic cross section of the measurement cell and the differential-mode setup with one sensor chip with *E. coli* immobilized by gel entrapment and the other without microorganisms as reference sensor.

external influences such as sensor drift, temperature fluctuations and external pH changes that might interfere. For preparation of the active sensor, *E. coli* with an optical density $OD_{600\,\mathrm{nm}} = 10$ (10×10^9 cells mL^{-1}) were cultivated as described in Section 4.3.4[2], diluted after harvesting in TBS buffer and mixed with the other components specified in Table 4.1. For the preparation of the reference sensor, only gel was implemented without *E. coli*. A volume of 20 µL gel was applied to each sensor surface forming a height of approximately 520 µm gel on top of each sensor. It is important to mention that also other gel compositions were utilized to reduce the gel thickness. This was performed by decreasing the volume of APS and TEMED in order to create a less solid gel. In addition, to induce hydrophobicity to the sensor surface a pretreatment was performed by means of an oxygen plasma. However, all these attempts failed due to insufficient

[2] In Section 4.3.4 the cultivation of *E. coli* for a glucose-measuring system is specified. For the cultivation of *E. coli* for an acetate-measuring system, sodium acetate is used as carbon source instead of glucose. Further details are given in Section 4.8.3

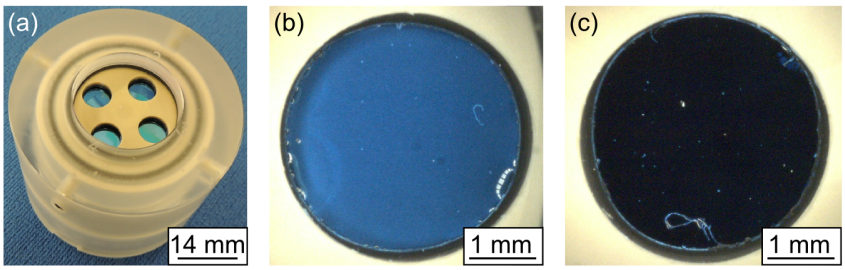

Figure 4.8: Biosensor test system for glucose and acetate measurements: a) photograph of the measuring cell hosting four EIS-sensor chips; b) sensor chip with immobilized microorganisms by gel entrapment (active sensor); c) sensor chip with gel only (reference sensor).

surface coverage. The gel spread to the sides and by doing that, the center of the sensor was left without gel. In Fig. 4.8a, a photograph of the measuring cell including four pH-sensitive field-effect sensors is shown. Fig. 4.8b depicts the sensor surface with immobilized *E. coli* and Fig. 4.8c illustrates the sensor surface with polyacrylamide gel but without bacteria. The sensor with *E. coli* avoids optical transmission, therefore, the surface with bacteria appears white, whereas the normal gel is transparent and the Ta_2O_5-surface is visible. The gel showed good adhesion to the sensor surface and appeared stable over long time of about 48 h in solution.

4.8.3 Differences between an *E. coli*-based glucose- and acetate-measuring system

E. coli employ the "mixed acid" fermentation pathway. The mixed acid pathway makes alternative end products and in variable amounts (e.g., lactate, acetate, formate, ethanol, carbon dioxide) [38]. Thus, *E. coli* are able to metabolize glucose

Table 4.2: Differences between an *E. coli*-based glucose- and acetate-measuring system in terms of the requirements for the cell preparation.

	Glucose-grown cells	Acetate-grown cells
Bacteria	*E. coli* K-12	*E. coli* K-12
Cultivation	M9-minimal medium + 20 µM glucose	M9-minimal medium + 25 – 50 µM sodium acetate
Harvesting	Begin or middle of exponential phase	Begin of exponential phase

Table 4.3: Differences between an *E. coli*-based glucose- and acetate-measuring system in terms of the measuring principle.

	Glucose-grown cells	Acetate-grown cells
Substrate	Glucose	Acetate and glucose
O_2 condition	O_2 not necessary	O_2 mandatory
Response behavior	Acidification	Alkalinization (acetate) / Acidification (glucose)

as well as acetate. However, there are some differences in the cell preparation, which are displayed in Table 4.2 and have to be taken into consideration. The preferred carbon source for *E. coli* is glucose. In order to utilize less preferred carbon sources, such as acetate, the bacterium needs to adapt its metabolism already at the state of cultivation. To understand the experiments in the following, the characteristics of the glucose- and acetate-measuring system in terms of the measuring principle should be mentioned as well. As shown in Table 4.3, glucose-adapted *E. coli* are only able to metabolize glucose, whereas acetate-adapted *E. coli* are capable to metabolize both acetate and glucose, respectively. Oxygen is mandatory for *E. coli* to metabolize acetate, while no oxygen is needed for the metabolism of glucose. The expected sensor response of the *E. coli*-based sensor towards a glucose pulse is an acidification and towards an acetate pulse an alkalinization resulting either in a decrease or increase of the pH value, respectively (see Fig. 4.1b).

4.8.4 Measurement of acetate and glucose

A typical response behavior of the acetate-measuring biosensor system is depicted in Fig. 4.9a. The measurement setup consisted of four pH-sensitive field-effect sensors. Two of them served as reference and two sensors were provided with acetate-adapted *E. coli* immobilized in PAA gel (active sensors). A high concentration of *E. coli* with an $OD_{600\,\mathrm{nm}}$ of 10 was utilized in the case of the active sensors and a total gel volume of 20 µL was applied to each sensor surface. As can be seen from Fig. 4.9a, the two reference sensors (1 and 4) as well as the two active sensors (2 and 3) follow the similar characteristics. The differential signals from Fig 4.9a are shown in Fig. 4.9b, in which the signal from sensor 4 has been chosen to be the reference for the two active sensors 2 and 3. In order to obtain a stable sensor signal, the sensors were conditioned with TBS buffer. Due to the fact that the intended stabilization did not occur even after 65 min, 3 mM acetate was added to the sensors. After approximately 25 min a clear alkalinization due to the microorganisms was observed. This is identified as a positive potential shift of ap-

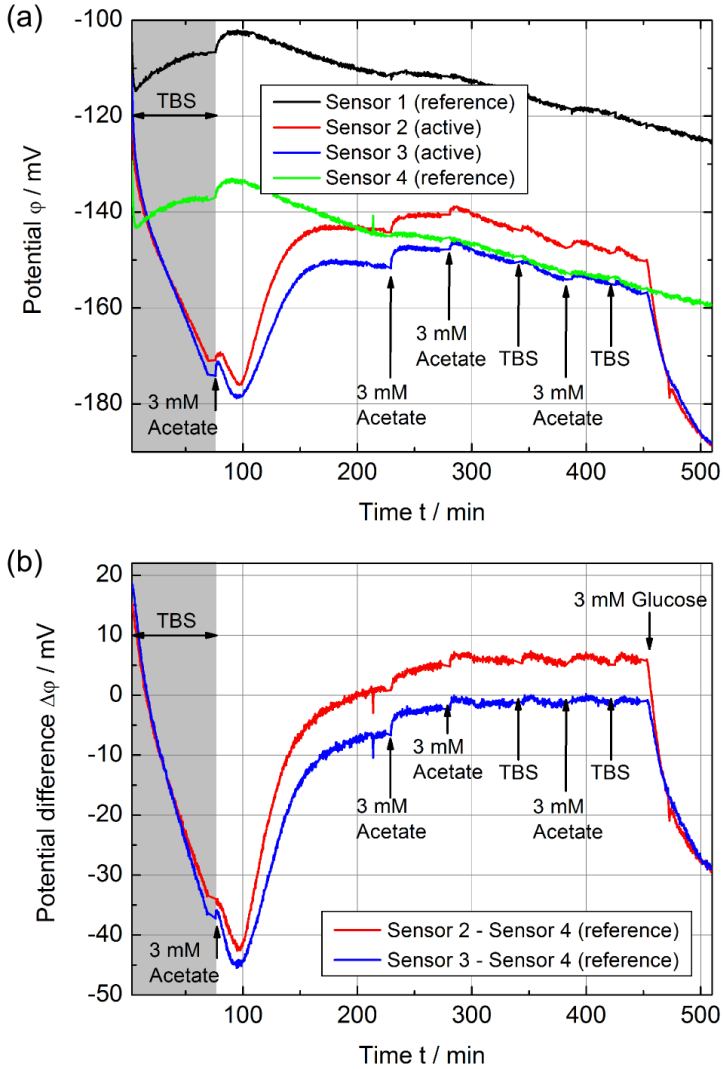

Figure 4.9: (a) Surface potential shifts of all four sensors (with (active; sensor 2 and 3) and without (reference; sensor 1 and 4) *E. coli* immobilized by gel entrapment) obtained by applying repeating acetate and glucose pulses. (b) Potential difference, calculated by the subtraction of reference sensor 4 from the active sensors 2 and 3, at different acetate and glucose concentrations. TBS was used for stabilization. The arrows indicate the time at which the measurement medium was changed. The concentration values imply the acetate and glucose concentrations in TBS buffer.

proximately 45 mV starting at minute 100 followed by a stabilizing sensor signal, which can be attributed to the acetate consumption of *E. coli*. A further increase of 3.2 mV is shown after a second application of 3 mM acetate. Repeatedly and alternately TBS buffer for stabilization and acetate for alkalinization was applied to the sensors. Slight changes were noticeable, however, not comparable to the first alkalinization response. To demonstrate the vitality of the microorganisms, 3 mM glucose was added, which resulted as expected in a significant acidification. A reason for the stagnating alkalinization response may rely on the fact that *E. coli* needs oxygen to degrade acetate. After the first and main alkalinization event, most of the dissolved oxygen in the electrolyte may have been consumed.

In order to use acetate as a carbon source, *E. coli* must adapt its metabolism. In the case of conventionally used "standard media" to cultivate cells (e.g., LB medium or M9-minimal medium with glucose) no alkalinization due to acetate addition will occur. Thus, a specific cultivation strategy with sodium acetate as carbon source as specified in Table 4.2 was used to adapt the cells to acetate already at the state of the cultivation.

The oxygen dependence of the acetate-measuring system represents a difficult task regarding its direct use in a biogas digester (in-line) that is known to presuppose strictly anaerobic conditions. To overcome this problem, this cell-based acetate-measuring system could be coupled with the biogas digester via a bypass system. In this way, the acetate-measuring system could be supplied with additional oxygen. Although, a direct application of the system in a real fermenter requires further optimization steps, the functionality of such an acetate-sensitive biosensor based on *E. coli* was demonstrated.

5 Capacitively coupled electrolyte-conductivity sensor based on high-k material of barium strontium titanate

Christina Huck[a,b], Arshak Poghossian[a,b], Matthias Bäcker[a,b], Shampali Chaudhuri[a], Willi Zander[b], Jürgen Schubert[b], Vardges K. Begoyan[c], Vahe V. Buniatyan[c], Patrick Wagner[d], Michael J. Schöning[a,b]

[a] *Institute of Nano- and Biotechnologies (INB), FH Aachen, Jülich, Germany*

[b] *Peter Grünberg Institute (PGI), Forschungszentrum Jülich GmbH, Jülich, Germany*

[c] *Department of Microelectronics and Biomedical Devices, State Engineering University of Armenia, Yerevan, Armenia*

[d] *Institute for Materials Research (IMO), Hasselt University, Diepenbeek, Belgium*

Published in: *Sensors and Actuators B: Chemical*, Vol. 198, pp. 102–109, 2014, DOI: org/10.1016/j.snb.2014.02.103

Submitted: 2013-11-26; Accepted: 2014-02-27; Published: 2014-03-18

5.1 Abstract

A miniaturized capacitively coupled contactless conductivity detection (C^4D) sensor based on high-k perovskite oxide of barium strontium titanate (BST) has been implemented for the first time. The BST film (∼120 nm thick) of $Ba_{0.25}Sr_{0.75}TiO_3$ composition were prepared on a p-Si-SiO_2-Pt structure by pulsed laser deposition technique using BST targets fabricated by the self-propagating high-temperature synthesis method. The Pt electrodes were buried into the SiO_2 layer to obtain a planar structure. For comparison, contact-mode electrolyte-conductivity (EC) sensors without the protective BST layer were also fabricated. To study the influence of the protective BST layer, both sensors were characterized in electrolyte solutions with various conductivities using two- and four-electrode operation modes. The impedance spectra were recorded in a frequency range from 1 Hz to 1 MHz. An equivalent circuit of the C^4D sensor is discussed as well.

Both, the EC and C^4D sensor, demonstrate nearly identical sensor characteristics. The obtained results clearly show the benefits of the use of the BST-based

C^4D sensor in a four-electrode configuration for contactless conductivity measurements. A linear dependence between the measured conductance and the electrolyte conductivity is obtained in a wide range of electrolyte conductivity from 0.3 mS/cm to 50 mS/cm. Moreover, typical problems associated with contact-mode EC detection such as the effect of possible redox processes, contamination and fouling of electrodes during continuous measurements can be minimized, thus, enhancing the life-time of conductivity sensors considerably.

5.2 Introduction

The measurement of electrolyte conductivity (EC) is nowadays common practice in analytical chemistry, process industry, food analysis and water-quality control [1–3]. In addition, a manifold of applications can be found in pharmacology, blood and urea analysis, and tissue-perfusion measurement as well as in the chemical and biological sensing field for the detection of a wide range of biochemical species, (e.g., amino acids, proteins, peptides, DNA), explosives and chemical warfare agents [4–6]. Usually, EC measurements are performed using nearly ideally polarizable inert metal electrodes (e.g., platinum or gold), which are in direct contact with the electrolyte. Generally found problems of contact-mode EC detection techniques are bubble formation due to electrolysis, the effect of redox processes and double-layer capacitance as well as contamination and fouling of electrodes during continuous use. As a consequence, the life time of the EC sensor can be shortened considerably [7–11]. These problems play a less dominant role in the sensor behavior, when the electrodes are electrically insulated from the electrolyte solution. For this, the electrodes are covered with a thin protective layer and the sensor couples capacitively with the electrolyte (so-called capacitively coupled contactless conductivity detection, abbreviated as C^4D). As a result, the formation of gas bubbles and degradation of electrodes can be prevented, thereby allowing the application of a wide variety of electrode materials. However, this protective layer introduces an additional capacitance, which raises the electrode impedance. As a consequence, C^4D sensors have a lower sensitivity when compared with contact-mode conductivity detection and require an application of higher measuring frequencies because the capacitance of the protective layer is usually much lower than the double-layer capacitances of non-protected electrodes [9, 12, 13]. In order to overcome these drawbacks and improve the C^4D sensitivity, different strategies have been described in literature. These include, for instance, increasing the detection area [14], minimizing the stray capacitance arising from direct capacitive coupling between the electrodes [15, 16] and the application of thin protecting materials having a high dielectric constant (e.g., Ta_2O_5 [8], SiC [17], TiO_2-doped protecting layer [18]). In this

context, due to the multi-functional material properties and high permittivity, perovskite oxides could be very attractive as protective material for those C^4D sensors.

In this paper, a novel C^4D sensor using a high-k perovskite oxide film of barium strontium titanate (BST) as protective layer has been developed. BST belongs to the most popular ferroelectric materials exhibiting unique ferroelectric, pyroelectric, piezoelectric, microwave and electro-optic properties [19–21]. Recently, BST films of various compositions have been used as pH-sensitive material in semiconductor field-effect-based pH sensors [22–24]. The developed C^4D sensors with a thin protective BST layer were tested in a two- and four-electrode configuration in different conductivity standard solutions. For comparison, contact-mode EC sensors (without a protective BST layer) were also fabricated and characterized.

5.3 Experimental

5.3.1 Self-propagating high-temperature synthesis (SHS) of BST

The perovskite oxide of $Ba_{0.25}Sr_{0.75}TiO_3$ composition has been synthesized by means of the SHS method using home-made technological equipment [25]. In comparison to the conventional high-temperature ceramic technique, the SHS method provides a short synthesis time and improved material properties. By variation of the initial mixture components and the combustion conditions, it is possible to produce multi-phase materials with a given chemical and phase composition. In addition, the SHS method is simple, ecologically clean, wasteless, energy-saving, highly productive and cost-effective [22, 26].

Details of the process steps of the BST synthesis are described in [22]. Briefly, the initial materials (Ti, TiO_2, $SrCO_3$ and BaO_2) have been milled to powder with grain sizes of about 5 – 10 µm. Then, the mixture of reactant powders is placed in a quartz-tube reactor and ignited by a heated wire. After initiation, a highly exothermic combustion of the powder mixture proceeds in the mode of self-propagation that converts the initial materials into the final high-quality product with a minimal amount of impurities. To prepare targets for the pulsed laser deposition (PLD) process, the synthesized SHS product has been milled to grains of 0.5 – 5 µm, pressed into cylindrical pellets, and then heated at 1350 °C for 4 – 5 h.

5.3.2 Fabrication of the C^4D sensor chip and physical characterization of the BST film

Planar four-electrode C^4D chips were fabricated by means of conventional silicon and thin-film technologies. The flowchart of the technological process steps

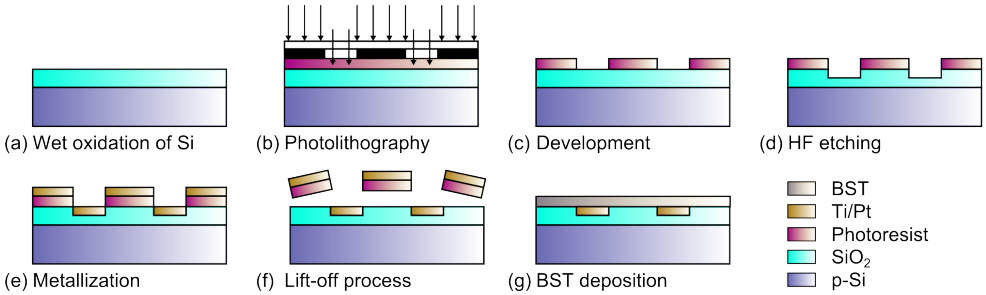

Figure 5.1: Fabrication-process flow of the planar EC sensor (a-f). The final C^4D sensor with a protective BST layer is presented in (g).

is schematically shown in Fig. 5.1. Initially, a 440 nm SiO_2 layer was grown (Fig. 5.1a) by thermal wet oxidation on a silicon substrate (p-Si, $\rho = 1000\,\Omega\,\mathrm{cm}$, Topsil Semiconductor Materials, Denmark). This thick SiO_2 layer was used to reduce the influence of the parasitic capacitance of the SiO_2 and the Si resistance on the electrolyte-conductivity sensor. Then, a photolithography process was done to define a trench area for burying of the metal electrodes (Fig. 5.1b-c). In order to bury the metal electrodes into the SiO_2 layer and thus, to achieve a planar sensor surface, shallow trenches with a depth of ∼175 nm were obtained by etching the SiO_2 with hydrofluoric acid (Fig. 5.1d). In a next step, the Ti/Pt layers were deposited by means of electron-beam evaporation (Fig. 5.1e) followed by a lift-off process (Fig. 5.1f). A thin layer of ∼10 nm Ti served as adhesive layer and ∼165 nm Pt as electrode material. Each of the four electrodes had a length of 4 mm and a width of 1 mm with an inter-electrode spacing of 1.3 mm between the inner electrodes and 0.1 mm between the inner and outer electrodes. The processed wafer was diced into separate chips (chip size: 10 mm × 10 mm). Part of these chips was used for contact-mode EC sensors, while another part was covered with a protecting BST layer to complete the C^4D sensors. The BST films (∼120 nm thick) of $Ba_{0.25}Sr_{0.75}TiO_3$ composition were prepared by PLD technique using targets fabricated by the SHS method (Fig. 5.1g). The main advantages of the PLD technique are the compatibility with silicon technology, the short deposition time, the possibility of deposition of insulators as well as of multi-component materials. To protect the bond pads, the BST films were deposited using a Si-shadow mask. The deposition was performed in an oxygen atmosphere (gas flow 30 ml/min, pressure 2×10^{-3} mbar) using a KrF-excimer laser (wavelength 248 nm, pulse length 20 ns, pulse frequency 10 Hz and an energy density of 2.5 J/cm^2). The photo of the fabricated four-electrode C^4D chip with BST as protective layer is presented in Fig. 5.2.

In a next step, the four-electrode EC and C^4D chips were mounted to custom-

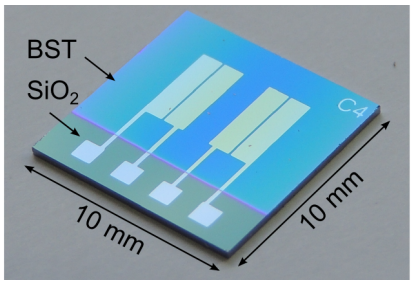

Figure 5.2: Photograph of the fabricated four-electrode C^4D sensor chip with BST as protective layer.

made printed circuits boards. Electrical connection was provided by means of ultrasonic wedge-wedge bonding. Finally, contact pads and bond wires were encapsulated by silicone rubber (RTV 118, Momentive Performance Materials Inc., USA) for electrical isolation from electrolyte solution.

The prepared BST layers have been physically characterized (thickness, stoichiometry and crystal morphology) by means of random Rutherford backscattering spectrometry (RBS), scanning electron microscopy (SEM) and X-ray diffraction analysis (XRD) methods. RBS was performed using 1.4 MeV He^+ ions. Figure 5.3 depicts a typical RBS measurement of a BST film deposited on a Si substrate. The

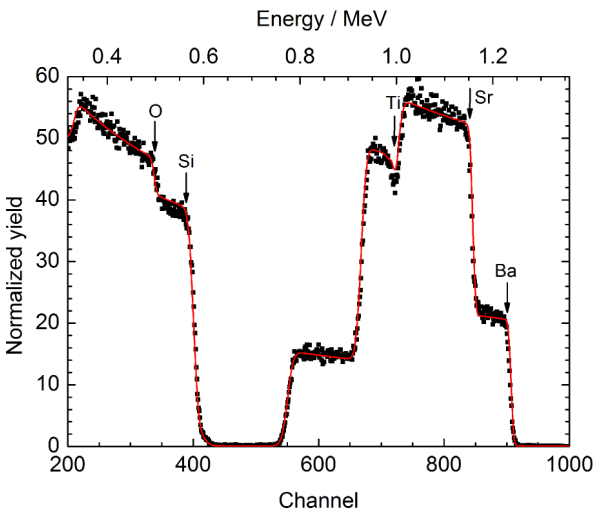

Figure 5.3: RBS measurement of a $Ba_{0.25}Sr_{0.75}TiO_3$ (120 nm) film deposited on a Si substrate. Simulation (solid line) is compared to experimental data (full squares).

measured RBS spectrum is in good agreement with the simulation performed with Rutherford universal manipulation program (RUMP) [27]. Clear steps corresponding to the constituent elements (Ba, Sr, Ti, O) were detected. The energy edges of the respective elements are indicated by arrows. The analysis of the RBS measurement verifies the stoichiometric composition of the deposited $Ba_{0.25}Sr_{0.75}TiO_3$ and gives a layer thickness of 120 nm.

Figure 5.4 shows a cross-sectional SEM picture of the layer stack p-Si-SiO_2-Ti-Pt-BST with a buried Pt electrode. This SEM image was obtained using focused-ion beam for sample preparation resulting in perpendicular profiles. For this procedure an additional, protective Pt film was deposited on top of the BST layer. As can be clearly seen, the Pt electrode is perfectly buried into the trench within the 440 nm thick SiO_2 layer. This becomes obvious when adding up the thicknesses of SiO_2 below the electrode (265 nm) and the Ti/Pt electrode (10 nm/165 nm) and comparing these heights with the SiO_2 thickness next to the electrode (440 nm). The PLD-prepared BST layer with a thickness of 120 nm is in accordance with the RBS analysis and completely closed over the total sensor structure.

The XRD study was carried out using a Bruker D8 diffractometer in the scanning range from 10° to 60° in 2θ. The XRD pattern (data not shown) indicates that the BST film had amorphous nature.

For the determination of the dielectric constant ϵ_i of the BST layer, separate structures were prepared. Capacitance-voltage measurements were performed of BST films in the metal-insulator-metal configuration with BST films sandwiched between bottom and top Pt electrodes. An average dielectric constant ϵ_i for the 120 nm thick BST film was about 186 ± 9.

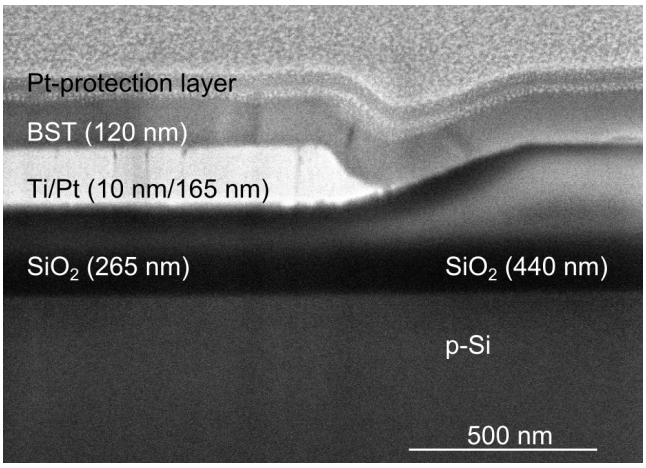

Figure 5.4: Cross-sectional SEM picture of the Si-SiO_2-Ti-Pt-BST layer stack with buried Pt electrodes.

5.3.3 Impedance measurement setup

To analyze the impact of the protective BST layer, the bare and the C^4D sensors were characterized in two- and four-electrode configuration by means of impedance spectroscopy. For the measurements, the sensors were exposed to different electrolyte-conductivity standard solutions from 0.3 mS/cm to 50 mS/cm (Mettler-Toledo AG, Switzerland and Sigma-Aldrich Chemie GmbH, Germany) and impedance spectra were recorded with an impedance analyzer module (Zennium, Zahner Elektrik GmbH, Germany) covering a frequency range from 1 Hz to 1 MHz. Since electrolyte conductivity is strongly dependent on temperature, all measurements were performed at a constant temperature of 25 °C inside a Faraday cage.

As shown in Fig. 5.5a, for the two-electrode configuration only the two inner electrodes of the C^4D sensor were used (two outer electrodes are disconnected). The same electrodes were utilized for applying an alternating voltage V_{in} of 20 mV and measuring the current I_0 through the same electrodes. The electrolyte resistance R_{el} is derived from the ratio V_{in}/I_0. In reality, the voltage V_{in} contains a voltage drop across the electrode impedance (series combination of the protective-layer capacitance C_{i} and the double-layer capacitance C_{dl}). Therefore, the resistance measured in this way is always greater than the bulk electrolyte resistance. This error can be eliminated (in theory) or minimized (in practice)

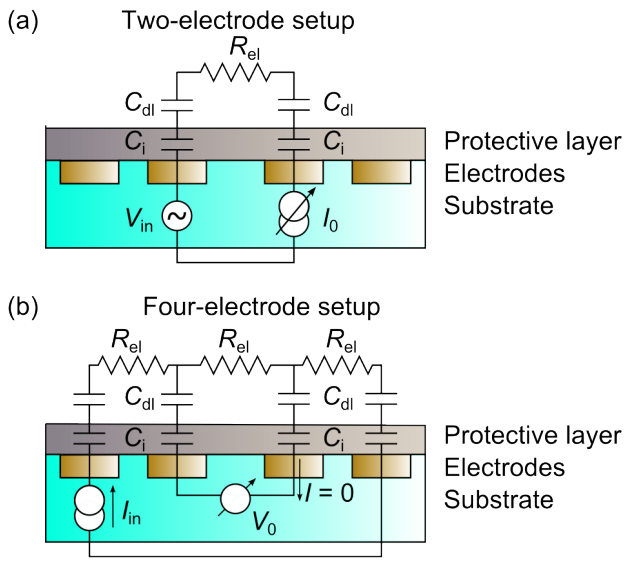

Figure 5.5: Measurement setup for the four-electrode C^4D sensor in a two-electrode (a) and four-electrode setup (b).

applying a four-electrode configuration [28] as presented in Fig. 5.5b. In the four-electrode configuration the two outer electrodes were used as current-driving electrodes (applying an alternating current of I_0 = 20 µA), while the two inner electrodes were used as potential-sensing electrodes. The key assumption by four-electrode measurements is that the potential-sensing electrodes are open circuits. This implies that no current enters the electrodes (in theory), avoiding any polarization effects. In practice, the voltage drop V_0 at the two inner electrodes is measured with negligible current. Thus, the ratio V_0/I_{In} is accurately equal to the bulk electrolyte resistance and does not include the electrode impedance and/or polarization effects. The four-electrode setup increases the linearity, accuracy, and sensitivity of the measurement.

5.4 Equivalent circuit of a C^{4}D sensor

Fig. 5.6a illustrates the equivalent circuit model of the developed C^{4}D sensor chip consisting of the Si-SiO$_2$ structure with Pt electrodes buried into the SiO$_2$ layer and protected from the solution with an insulator layer (in this study, BST film). The capacitance of the BST insulator layer is presented by C_{i}. Its value can be determined by the thickness and permittivity of the protective layer and the area of the covered platinum electrodes. The formation of the electrical-double layer known from metal electrodes also takes place at the protective layer/electrolyte interface [29, 30] and can be denoted by C_{dl}. The conductive and dielectric contribution of the liquid is represented by the electrolyte resistance R_{el} to be measured and a capacitance C_{el} (placed in parallel to R_{el}), respectively. The resistance R_{el} is linked to the conductivity σ by a geometric factor, the cell constant K_{c}, according to Eq. 5.1:

$$R_{el} = \frac{K_c}{\sigma} \tag{5.1}$$

The cell constant is connected to the spacing between the metal electrodes, the area of the electrodes, and the sensor design. The value of C_{el} is determined by the dielectric constant and of the electrolyte (ϵ_{w} = 80) and the cell constant [28]: $C_{\mathrm{el}} = \epsilon_0\epsilon_{\mathrm{w}}/K_{\mathrm{c}}$, where ϵ_0 is the permittivity of vacuum. For a cell-constant value of K_{c} = 1 cm^{-1}, the C_{el} is very small (< 7 pF) and its influence on the conductivity detection can be neglected. Thus, the impedance of the upper branch of the equivalent circuit Z_1 can be described as a series combination of C_{i}, C_{dl} and R_{el} and is given by:

$$Z_1 = R_{el} + \frac{2}{j\omega C_{dl}} + \frac{2}{j\omega C_i} = R_{el} - j\frac{2\left(C_{dl} + C_i\right)}{\omega C_{dl} C_i} \tag{5.2}$$

where j represents the imaginary unit, $\omega = 2\pi f$, and f is the frequency.

The lower half-space of the sensor structure consisting of the silicon substrate and SiO_2 can electrically be considered as a series configuration of two capacitances, C_{SiO_2}, and a resistance R_{sub} through the silicon substrate. With a SiO_2 thickness of approximately 265 nm and a dielectric constant of 3.9 the insulation capacitance per unit area can be calculated to $C_{SiO_2} = 1.3 \times 10^{-10}$ F/mm^2. The capacitance of SiO_2 with a surface area of a single Pt electrode (A = 4 mm^2) is approximately 0.5 nF. The capacitance between the electrodes is represented by C_b. Due to the large electrode distance (~1.3 mm) and the low electrode

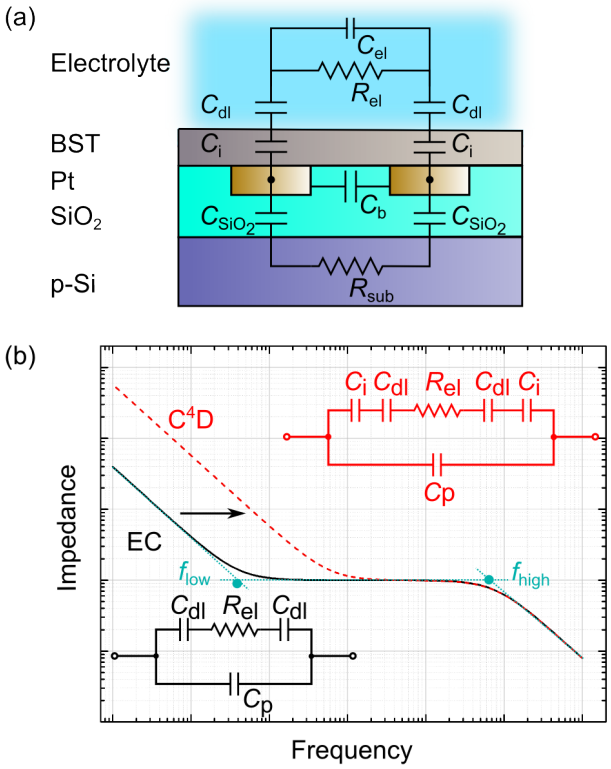

Figure 5.6: Equivalent-circuit model of the C^4D sensor (a) and comparison of a typical frequency response of C^4D and EC sensors using a simplified equivalent circuit (inlets) (b). R_{el}: electrolyte resistance; R_{sub}: silicon resistance; C_{el}, C_{dl}, $C_{BST} = C_i$, C_b and C_{SiO_2} are capacitances of the electrolyte, double layer, protective insulating layer (BST), between electrodes and SiO_2, respectively. An additional capacitance C_p in parallel is associated with all parasitic elements, including stray capacitances of the sensor structure, cables and measurement system.

thickness (180 nm), the value of C_b is very small. Thus, the impedance of the elements of the lower branch of the equivalent circuit is much higher than of the upper branch. As a consequence, these elements can be neglected.

With the above mentioned considerations, the equivalent circuit model in Fig. 5.6a can be simplified to the model presented as inset in the upper right corner of Fig. 5.6b for a two-electrode C^4D sensor. For comparison, a simplified equivalent circuit of the EC sensor (without protective layer) is presented, too (lower left corner). Note, in Fig. 5.6b an additional parasitic stray capacitance C_p is included, which takes into account the influence of all parasitic elements, including the stray capacitance of the sensor structure, electrical cables and input capacitances of the measuring device. The parasitic capacitance, being parallel to the sensor impedance, causes a loss in sensitivity. The impedance of this capacitance is $Z_2 = 1/j\omega C_\mathrm{p}$. Thus, the total impedance $Z(j\omega)$ of the C^4D sensor is retrieved from the parallel combination of Z_1 and Z_2, and is given by the expression:

$$Z(j\omega) = \frac{Z_1 Z_2}{Z_1 + Z_2} = \frac{Z_1}{\left(1 + j\omega C_p Z_i\right)} \tag{5.3}$$

As can be seen from the Eq. 5.3 and typical shape of the log-log scaled impedance-spectroscopy curves in Fig. 5.6b, the total impedance is not only a function of the electrolyte resistance R_el. At different frequencies, the overall impedance is dominated by different circuit elements. At lower frequencies the impedance is dominated by the series combination of the double-layer and protective layer capacitance, C_dl and C_i, respectively. The low cut-off frequency can be expressed as:

$$f_{low} = \frac{C_{dl} + C_i}{\pi R_{el} C_{dl} C_i} \tag{5.4}$$

In contrast, at frequencies higher than a high cut-off frequency of:

$$f_{high} = \frac{1}{2\pi R_{el} C_p} \tag{5.5}$$

the impedance is dominated by the parasitic stray capacitance C_p. Only in an intermediate frequency band, the measured impedance is mainly governed by the electrolyte resistance. This plateau region is of interest in terms of measuring the electrolyte conductivity. The width of this frequency band depends on the ratio $f_\mathrm{high}/f_\mathrm{low}$, which is equal to:

$$\frac{f_{high}}{f_{low}} = \frac{C_{dl}}{2C_p}\left(\frac{C_i}{C_i + C_{dl}}\right) \tag{5.6}$$

The closer the term in parentheses of Eq. 5.6 approaches unity, the wider is the frequency band in which the electrolyte resistance R_el can be measured. As

presented in Fig. 5.6b, it becomes obvious, that an additional protective layer shifts the impedance curve in the low-frequency range to the right (towards higher frequency values) yielding a smaller frequency band compared to a conventional EC sensor. Increasing the measurement frequency, on the other hand, increases the effect of stray capacitance on the signal. Thus, to minimize this effect, a high value for C_i is desired.

Generally, the choice of the insulating material that covers the electrodes in C^4D sensors is of primary importance. Because the capacitance of a protective insulator material used (e.g., Ta_2O_5 [8], SiC [17]) is usually an order of magnitude smaller than the double-layer capacitance ($C_\mathrm{i} \ll C_\mathrm{dl}$) depending on electrolyte composition and concentration, the presence of C_i decreases the influence of the double-layer capacitance. However, very low values of the insulator-layer capacitance will also increase the influence of the parasitic capacitance C_p. On the other hand, in order to obtain sufficient capacitive coupling of the C^4D sensors to the liquid, a very thin insulator layer with a high dielectric constant is required. The use of thin high-permittivity films yields a high value for C_i that makes it possible to work at lower measuring frequencies but, at the same time, increases also the influence of C_dl. Thus, some compromise should be found. As it has been described in [10], for optimal working and accurate measurements of the electrolyte conductivity with the C^4D sensor, the permittivity-to-thickness ratio of the protective layer should be larger than $0.4\,\mathrm{nm}^{-1}$. This requirement can be met very well for the high-k BST films used in this study as protective material. Besides the high permittivity-to-thickness ratio of about $1.55\,\mathrm{nm}^{-1}$, the BST/solution interface has a stable, relatively low impedance, which is, similar to other pH-sensitive materials such as Ta_2O_5, Si_3N_4 or SiO_2 [31–35], almost totally determined by the activity of protons in the solution [22, 23].

5.5 Results and discussion

5.5.1 Two-electrode setup

Figure 5.7 shows typical impedance (modulus) spectra for an EC sensor without a protective layer (a) and a C^4D sensor with a protective layer of 120 nm BST (b). These impedance spectra were recorded in a two-electrode setup in various standard conductivity solutions in the range between 0.3 mS/cm and 50 mS/cm. Both spectra can be divided in three distinct regions.

At low frequencies ($f < 1\,\mathrm{Hz} - 1\,\mathrm{kHz}$ depending on electrolyte conductivity of the solution), the impedance of the EC sensor in Fig. 5.7a is mainly governed by the unfavorable influence of the double-layer capacitance C_dl resulting in a poor sensitivity in that frequency range. The double-layer capacitance (conditioned by the Stern layer [36]) increases with increasing ionic strength of the solution. As

a consequence, the impedance decreases. As expected, this effect of the ionic strength is not observed for the C^4D sensor. The impedance of the C^4D sensor in Fig. 5.7b in the low frequency range is independent of the ionic strength of the solution and approximately two times higher (∼400 kΩ at 1 Hz) compared to the impedance of the EC sensor (∼200 kΩ at 1 Hz). As mentioned above, the low-frequency range of the impedance spectra is determined by the series combination of the double-layer capacitance and the protecting-layer capacitance. The protecting-layer capacitance is smaller compared to the double-layer capacitance and thus, dominates this frequency region.

At high frequencies (e.g., at f > 20 kHz in the solution with a conductivity of

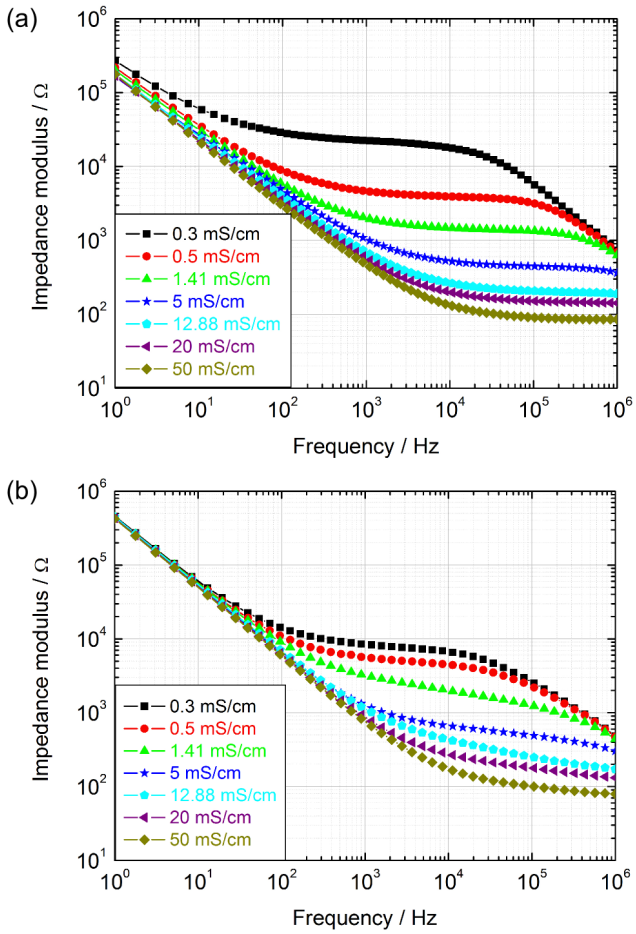

Figure 5.7: The impedance (modulus) as a function of frequency of the EC sensor (a) and the C^4D sensor with 120 nm BST as protective layer (b), recorded in a two-electrode setup in various conductivity standard solutions.

0.3 mS/cm), a second capacitive impedance regime can be identified, that is due to parasitic capacitances C_{p}, which makes the sensor insensitive to conductivity changes. This parasitic capacitance influences the impedance characteristic of the EC and the C^4D sensor in the same manner.

In the frequency range between these cut-off frequencies, the impedance is mostly governed by the resistance of the solution. In this frequency band, the sensors are sensitive to changes in conductivity. However, due to the shift of the resistive plateau towards higher frequencies for higher electrolyte conductivities, an adaption of the measuring frequency is required, in order to get optimal accuracy, linearity, sensitivity, and dynamic range. Comparing the impedance spectra of the EC sensor with the C^4D sensor, it becomes apparent, that the plateau region of the C^4D sensor is slightly narrowed and not purely resistive. The impedance of the protecting BST layer is superimposed to the solution resistance in the intermediate frequency range. Nevertheless, due to the benefits of the high dielectric constant and the thin BST layer, a clear dependency on electrolyte conductivity can be recognized. In addition, the problems associated with contact-mode EC detection techniques, such as bubble formation due to electrolysis, the effect of redox processes, as well as contamination and fouling of electrodes during continuous use, can be eliminated or at least minimized.

5.5.2 Four-electrode setup

In Fig. 5.8, the impedance spectra of the EC and C^4D sensors measured in a four-electrode setup are presented. Exemplarily, the phase as a function of the frequency is presented for the C^4D sensor additionally (see Fig. 5.8c). Both sensors exhibit identical impedance spectra in standard conductivity solutions from 0.3 mS/cm to 50 mS/cm. As expected, the four-electrode setup significantly increases the measuring frequency range up to five decades. The influence of double-layer capacitance C_{dl} and the protection-layer capacitance C_{i} are eliminated. However, at low electrolyte conductivities and above 10 kHz, the impact of the parasitic capacitance C_{p} becomes apparent as in case of the two-electrode setup. In Fig. 5.8c it can be seen that the phase remains to 0°, the impedance exhibits purely resistive behavior. The parasitic capacitance contributes to the impedance at frequencies $f > 1$ kHz and in solutions with low electrolyte conductivity.

For more detailed analysis, Fig. 5.9 shows the conductance as a function of the electrolyte conductivity for the EC sensor and the BST-based C^4D sensor in the two- and four-electrode setup. The data were obtained from the measurements at 10 kHz for the two-electrode setup and at 1 kHz for the four-electrode setup, respectively. A linear dependence between the measured conductance and the electrolyte conductivity is obtained in a wide range of electrolyte conductivity for

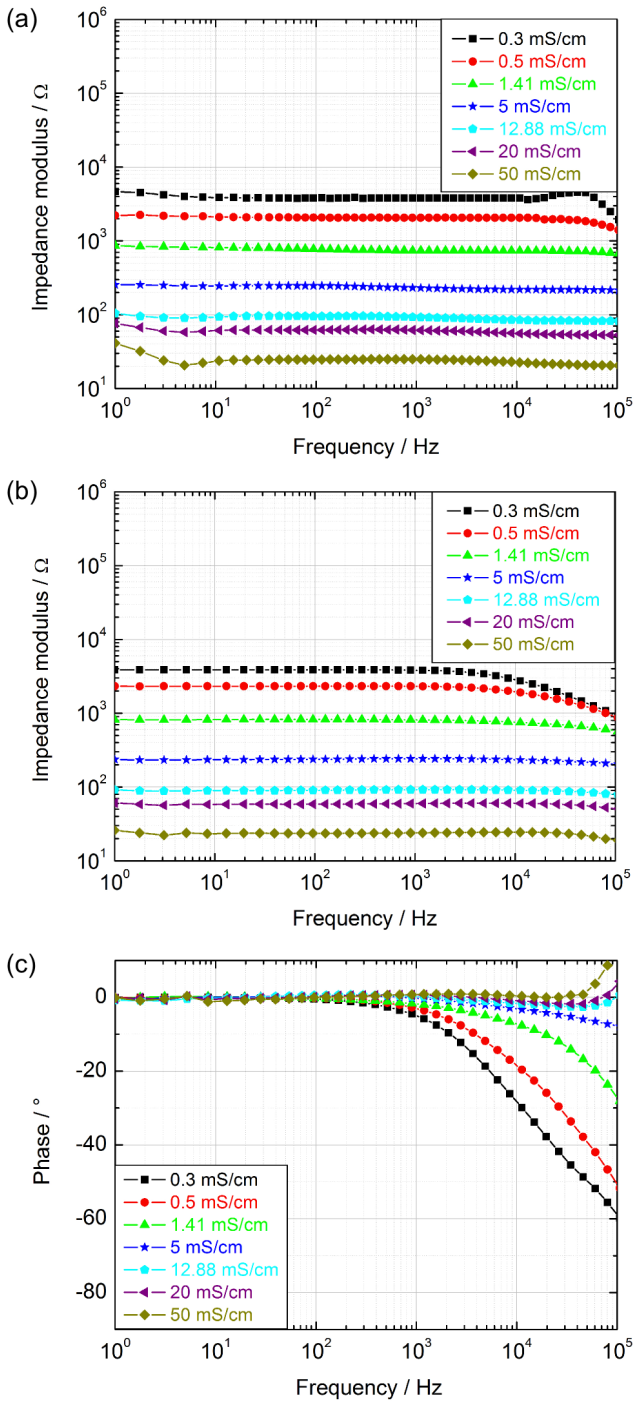

Figure 5.8: The impedance as a function of frequency of the EC sensor (a) and the C^4D sensor with 120 nm BST as protective layer (b) is presented. The phase as a function of frequency of the C^4D sensor is shown in (c). All measurements are performed in a four-electrode setup.

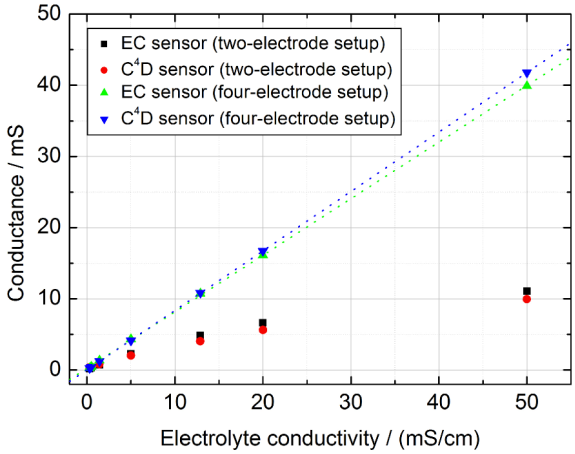

Figure 5.9: Conductance as a function of the electrolyte conductivity for the EC sensor and the C^4D sensor in two- and four-electrode setup, respectively. The curves are obtained from the measurements at 10 kHz for the two-electrode setup and at 1 kHz for the four-electrode setup.

both the EC and the C^4D sensor using a four-electrode setup (dashed lines). This was used to determine the cell constants of the investigated sensor structures. The cell constant is attributed to the geometry of the sensor (i.e., electrode area and spacing) [37]. Note, the cell constant is the inverse of the slope, thus, a higher slope refers to a lower cell constant. The cell constants amounted to 1.26 cm^{-1} and 1.20 cm^{-1} for the EC sensor and the C^4D sensor, respectively.

Such linear sensor behavior was not observed for the measurements in the two-electrode setup. Here, a linear range was observed only up to an electrolyte conductivity of 5 mS/cm. The cell constants for this conductivity range, were estimated to 2.30 cm^{-1} and to 2.86 cm^{-1} for the EC and the C^4D sensor, respectively. Table 5.1 summarizes the estimated cell constants and the linear measurement range at a glance. Generally, the cell constants of the sensors measured in the two-electrode configuration are higher than in the four-electrode configuration, independently of the sensor type. This is in agreement with theoretical considerations and experimental results in [28]. In the four-electrode setup the electrode impedance is eliminated and thus, the measurement is more accurate.

In the two-electrode setup, the cell constant of the C^4D sensor is higher (20%) compared to the cell constant of the EC sensor. In the four-electrode setup, both sensors exhibit practically the same cell constant. Thus, the protecting BST layer has an influence on the sensor performance in a two-electrode configuration, while in a four-electrode configuration the impact is negligibly small showing the

Table 5.1: Cell constant and linear measurement range for the EC sensor and C^4D sensor in the two- and four-electrode setup, respectively.

Sensor type	Number of electrodes	Cell constant / cm^{-1}	Linear range / (mS/cm)
EC sensor	2	2.30	0.3 to 0.5
C^4D sensor	2	2.86	0.3 to 0.5
EC sensor	4	1.26	0.3 to 50
C^4D sensor	4	1.20	0.3 to 50

preference of a four-electrode setup. In addition, the problems associated with contact-mode EC detection techniques can be eliminated or at least minimized.

5.6 Conclusions

A new C^4D sensor with a protective layer based on high-k perovskite oxide of $Ba_{0.25}Sr_{0.75}TiO_3$ has been developed for the first time. For better sensor performance, planar EC and C^4D structures with Pt electrodes buried into the thick SiO_2 layer were fabricated. The influence of the protective BST layer on the sensor characteristics was investigated in both two- and four-electrode operation modes. These results were compared to measurements with an EC sensor without a protective BST layer.

The obtained results clearly demonstrate the benefits of the use of the BST-based C^4D sensor in a four-electrode configuration for contactless conductivity measurements. No negative impact of the protective BST layer on the conductivity sensor performance could be identified. Advantageously, the C^4D sensor might possibly use cheaper electrode materials such as, for instance, Al films instead of noble metals. In addition, the problems associated with contact-mode EC detection techniques, like bubble formation due to electrolysis, the effect of redox processes, as well as contamination and fouling of electrodes during continuous measurements can be eliminated or at least minimized, thus, enhancing the life-time of conductivity sensors considerably.

5.7 Acknowledgments

The authors gratefully thank H. Iken for technical support and Dr. E. Neumann (Forschungszentrum Jülich GmbH) for performing the SEM analysis. C. Huck thanks FH Aachen for the Ph.D. scholarship. V. K. Begoyan thanks the Early Career Support Program (Grant ECP-12-07) and V.V. Buniatyan thanks the State

Committee of Science MES RA (Grant SCS-13-2G032) for financial support. Part of this project is co-financed by the European Union (ERDF). "The Commission, investing in your future".

5.8 Bibliography

[1] Kubáň, P.; Hauser, P. C.: A review of the recent achievements in capacitively coupled contactless conductivity detection. *Analytica Chimica Acta* 607 (2008), No. 1, p. 15–29

[2] Pumera, M.: Contactless conductivity detection for microfluidics: Designs and applications. *Talanta* 74 (2007), No. 3, p. 358–364

[3] Coury, L.: Conductance measurements. Part 1: Theory. *Current Separations* 18 (1999), No. 3, p. 91–96

[4] Daniels, J. S.; Pourmand, N.: Label-free impedance biosensors: Opportunities and challenges. *Electroanalysis* 19 (2007), No. 12, p. 1239–1257

[5] Trutman, E. D.; Newbower, R. S.: A practical analysis of the electrical conductivity of blood. *IEEE Transactions on Biomedical Engineering* BME-30 (1983), No. 3, p. 141–154

[6] Kubáň, P.; Hauser, P. C.: Ten years of axial capacitively coupled contactless conductivity detection for CZE - a review. *Electrophoresis* 30 (2009), No. 1, p. 176–188

[7] Bousse, L.; Bergveld, P.: On the impedance of the silicon dioxide/electrolyte interface. *Journal of Electroanalytical Chemistry* 152 (1983), No. 1-2, p. 25–39

[8] Olthuis, W.; Volanschi, A.; Bomer, J.; Bergveld, P.: A new probe for measuring electrolytic conductance. *Sensors and Actuators B: Chemical* 13 (1993), No. 1-3, p. 230–233

[9] Laugere, F.; Lubking, G.; Berthold, A.; Bastemeijer, J.; Vellekoop, M. J.: Downscaling aspects of a conductivity detector for application in on-chip capillary electrophoresis. *Sensors and Actuators A: Physical* 92 (2001), No. 1-3, p. 109–114

[10] Rana, S.; Page, R. H.; McNeil, C. J.: Impedance spectra analysis to characterize interdigitated electrodes as electrochemical sensors. *Electrochimica Acta* 56 (2011), No. 24, p. 8559–8563

[11] Baltussen, E.; Guijt, R. M.; van der Steen, G.; Laugere, F.; Baltussen, S.; van Dedem, G. W. K.: Considerations on contactless conductivity detection in capillary electrophoresis. *Electrophoresis* 23 (2002), No. 17, p. 2888–2893

[12] Coltro, W. K.; Lima, R. S.; Segato, T. P.; Carrilho, E.; de Jesus, D. P.; do Lago, C. L.; da Silva, J. A. F.: Capacitively coupled contactless conductivity detection on microfluidic systems - ten years of development. *Analytical Methods* 4 (2012), No. 1, p. 25–33

[13] Olthuis, W.; Sprenkels, A.; Bomer, J.; Bergveld, P.: Planar interdigitated electrolyte-conductivity sensors on an insulating substrate covered with Ta_2O_5. *Sensors and Actuators B: Chemical* 43 (1997), No. 1-3, p. 211–216

[14] Lee, C.-Y.; Chen, C. M.; Chang, G.-L.; Lin, C.-H.; Fu, L.-M.: Fabrication and characterization of semicircular detection electrodes for contactless conductivity detector – CE microchips. *Electrophoresis* 27 (2006), No. 24, p. 5043–5050

[15] Huang, Z.; Jiang, W.; Zhou, X.; Wang, B.; Ji, H.; Li, H.: A new method of capacitively coupled contactless conductivity detection based on series resonance. *Sensors and Actuators B: Chemical* 143 (2009), No. 1, p. 239–245

[16] Huang, Z.; Long, J.; Xu, W.; Ji, H.; Wang, B.; Li, H.: Design of capacitively coupled contactless conductivity detection sensor. *Flow Measurement and Instrumentation* 27 (2012), p. 67–70

[17] Laugere, F.; Lubking, G.; Bastemeijer, J.; Vellekoop, M. J.: Design of an electronic interface for capacitively coupled four-electrode conductivity detection in capillary electrophoresis microchip. *Sensors and Actuators B: Chemical* 83 (2002), No. 1-3, p. 104–108

[18] Lima, R. S.; Segato, T. P.; Gobbi, A. L.; Coltro, W. K.; Carrilho, E.: Doping of a dielectric layer as a new alternative for increasing sensitivity of the contactless conductivity detection in microchips. *Lab on a Chip* 11 (2011), No. 24, p. 4148–4151

[19] Setter, N.; Damjanovic, D.; Eng, L.; Fox, G.; Gevorgian, S.; Hong, S.; Kingon, A.; Kohlstedt, H.; Park, N. Y.; Stephenson, G. B.; Stolitchnov, I.; Tagantsev, A. K.; Taylor, D. V.; Yamada, T.; Streiffer, S.: Ferroelectric thin films: Review of materials, properties, and applications. *Journal of Applied Physics* 100 (2006), No. 5, p. 051606(1–46)

[20] Tagantsev, A. K.; Sherman, V. O.; Astafiev, K. F.; Venkatesh, J.; Setter, N.: Ferroelectric materials for microwave tunable applications. *Journal of Electroceramics* 14 (2005), No. 3, p. 199–203

[21] Gevorgian, S.; Vorobiev, A.; Lewin, T.: DC field and temperature dependent acoustic resonances in parallel-plate capacitors based on $SrTiO_3$ and $Ba_{0.25}Sr_{0.75}TiO_3$ films: Experiment and modeling. *Journal of Applied Physics* 99 (2006), No. 12, p. 124112(1–11)

[22] Buniatyan, V. V.; Abouzar, M. H.; Martirosyan, N. W.; Schubert, J.; Gevorgian, S.; Schöning, M. J.; Poghossian, A.: pH-sensitive properties of barium strontium titanate (BST) thin films prepared by pulsed laser deposition technique. *Physica Status Solidi A* 207 (2010), No. 4, p. 824–830

[23] Chen, C.-Y.; Chou, J.-C.; Chou, H.-T.: pH sensing of $Ba_{0.7}Sr_{0.3}TiO_3$ film for metal-oxide-semiconductor and ion-sensitive field-effect transistor devices. *Journal of The Electrochemical Society* 156 (2009), No. 6, p. G59–G64

[24] Chen, C.-Y.; Chou, J.-C.; Chou, H.-T.: Modeling of drift and hysteretic sensing phenomena of the $Ba_{0.7}Sr_{0.3}TiO_3$ pH-ion-sensitive field-effect transistor. *Japanese Journal of Applied Physics* 47 (2008), No. 11, p. 8525–8529

[25] Martirosyan, N. W.; Avagyan, P.; Buniatyan, V. V.; Andreev, V.; Vandunts, T. V.: Self-propagating high-temperature synthesis apparatus. Patent of Republic of Armenia, N.2102 (2008)

[26] Poghossian, A.; Abovian, H. V.; Avakian, P. B.; Mkrtchian, S. H.; Haroutunian, V. M.: Bismuth ferrites: New materials for semiconductor gas sensors. *Sensors and Actuators B: Chemical* 4 (1991), No. 3-4, p. 545–549

[27] Doolittle, L. R.: A semiautomatic algorithm for Rutherford backscattering analysis. *Nuclear Instruments and Methods in Physics Research Section B: Beam Interactions with Materials and Atoms* 15 (1986), No. 1–6, p. 227–231

[28] He, D.; Shannon, M. A.; Miller, N. R.: Micromachined silicon electrolytic conductivity probes with integrated temperature sensor. *IEEE Sensors Journal* 5 (2005), No. 6, p. 1185–1196

[29] Bockris, J. O.; Conway, B. E.; Yeager, E.: *Comprehensive Treatise of Electrochemistry, Volume 1: The Double Layer*. New York: Plenum Press, (1980). – ISBN 9780306402753

[30] Morrison, S. R.: *Electrochemistry at Semiconductor and Oxidized Metal Electrodes*. New York: Plenum Press, (1980). – ISBN 9780306405242

[31] Poghossian, A.; Baade, A.; Emons, H.; Schöning, M. J.: Application of ISFETs for pH measurement in rain droplets. *Sensors and Actuators B: Chemical* 76 (2001), No. 1-3, p. 634–638

[32] Schöning, M. J.; Näther, N.; Auger, V.; Poghossian, A.; Koudelka-Hep, M.: Miniaturised flow-through cell with integrated capacitive EIS sensor fabricated at wafer level using Si and SU-8 technologies. *Sensors and Actuators B: Chemical* 108 (2005), No. 1-2, p. 986–992

[33] Poghossian, A.: Determination of the pH_{pzc} of insulators surface from capacitance–voltage characteristics of MIS and EIS structures. *Sensors and Actuators B: Chemical* 44 (1997), No. 1-3, p. 551–553

[34] Poghossian, A.: The super-Nernstian pH sensitivity of Ta_2O_5-gate ISFETs. *Sensors and Actuators B: Chemical* 7 (1992), No. 1-3, p. 367–370

[35] Siqueira Jr., J. R.; Bäcker, M.; Poghossian, A.; Zucolotto, V.; Oliveira Jr., O. N.; Schöning, M. J.: Associating biosensing properties with the morphological structure of multilayers containing carbon nanotubes on field-effect devices. *Physica Status Solidi A* 207 (2010), No. 4, p. 781–786

[36] Wang, J.: *Analytical Electrochemistry*. Hoboken / N.J: Wiley, (2006). – ISBN 9780471678793

[37] Olthuis, W.; Streekstra, W.; Bergveld, P.: Theoretical and experimental determination of cell constants of planar-interdigitated electrolyte conductivity sensors. *Sensors and Actuators B: Chemical* 24 (1995), No. 1-3, p. 252–256

5.9 Supporting information

5.9.1 Study on the protective properties of BST

In Subsection 5.3.2, the protective BST layer has been physically characterized in terms of its thickness, stoichiometry and crystal morphology. An important requirement of the protective BST layer in terms of the C^4D sensor is its electrical isolation of the underlaying Pt electrodes from the electrolyte solution. Therefore, a comparative electrochemical characterization of the EC and the C^4D sensor was performed by cyclic voltammetry (CV) to study the protective properties of BST.

CV is a versatile electro-analytical method for acquiring qualitative information about electro-active reactions. The power of cyclic voltammetry results from its ability to rapidly provide considerable information on the thermodynamics of redox processes, on kinetics of heterogeneous electron-transfer reactions, and on coupled chemical reactions or adsorption processes. A comprehensive description of CV can be found elsewhere [36].

Figure 5.10 illustrates the CV performed with the EC and the C^4D sensor, respectively. This CV experiment has been conducted with a three-electrode setup using the EC sensor and consecutively the C^4D sensor as working electrode, a

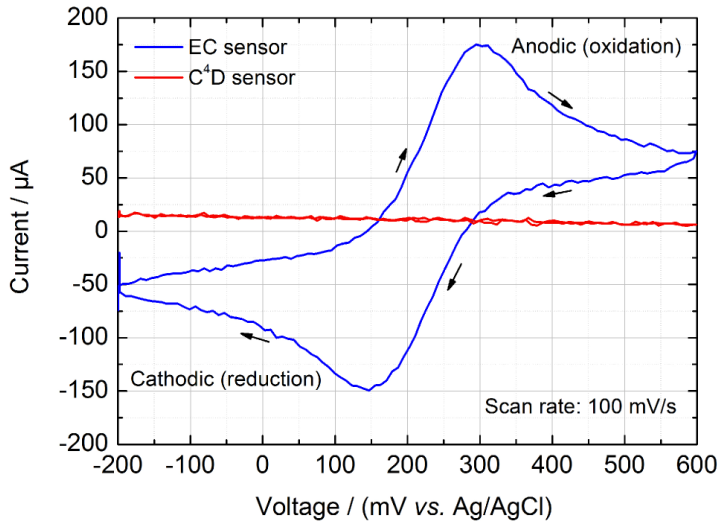

Figure 5.10: Cyclic voltammetry for the reduction of 10 mM ferricyanide in 150 mM PBS performed with the EC sensor and the C^4D sensor, respectively. A scan rate of 100 mV/s was used. The peak shape of the oxidative and reverse reductive current vs. electrode potential is apparent for the EC sensor, but not for the C^4D sensor demonstrating the protective properties of BST.

conventional liquid-junction Ag/AgCl electrode (Metrohm) as reference electrode and a commercial Pt electrode (Metrohm) as counter electrode. All three electrodes were immersed into 10 mM potassium hexacyanoferrate (III) ($K_3[Fe(CN)_6]$) in 150 mM phosphate buffer solution (PBS) with a pH value of 7.4. The working electrode potential was ramped linearly versus time with a scan rate of 100 mV/s. The well-known ferricyanide/ferrocyanide couple was used as an example of an electrochemically reversible redox couple to clarify whether the BST layer galvanically isolates the Pt electrodes from the electrolyte or not. If the BST layer is closed and protecting the electrodes, no oxidation or reduction peaks should be apparent in the voltammogram performed with the C^4D sensor. As can be clearly seen in Fig. 5.10, the EC sensor shows the expected peak shape response of the redox couple during a single potential cycle, whereas no peaks are visible for the C^4D sensor. Thus, the protective properties of BST are demonstrated.

6 Multi-parameter sensor chip with barium strontium titanate as multi-purpose material

Christina Huck[a,b], Arshak Poghossian[a,b], Sebastian Schusser[a,b], Matthias Bäcker[a,b], Iman Kerroumi[a], Willi Zander[b], Jürgen Schubert[b], Norayr W. Martirosyan[c], Vahe V. Buniatyan[c], Patrick Wagner[d], Michael J. Schöning[a,b]

[a] *Institute of Nano- and Biotechnologies (INB), FH Aachen, Jülich, Germany*

[b] *Peter Grünberg Institute (PGI), Forschungszentrum Jülich GmbH, Jülich, Germany*

[c] *Department of Microelectronics and Biomedical Devices, State Engineering University of Armenia, Yerevan, Armenia*

[d] *Institute for Materials Research (IMO), Hasselt University, Diepenbeek, Belgium*

Published in: *Electroanalysis*, Vol. 26, pp. 980–987, 2014, DOI: 10.1002/elan.201400076

Submitted: 2014-02-11; Accepted: 2014-02-17; Published: 2014-04-01

6.1 Abstract

It is well known that biochemical and biotechnological processes are strongly dependent and affected by a variety of physico-chemical parameters such as pH value, temperature, pressure and electrolyte conductivity. Therefore, these quantities have to be monitored or controlled in order to guarantee a stable process operation, optimization and high yield. In this work, a sensor chip for the multi-parameter detection of three physico-chemical parameters such as electrolyte conductivity, pH and temperature is realized using barium strontium titanate (BST) as multi-purpose material. The chip integrates a capacitively coupled four-electrode electrolyte-conductivity sensor, a capacitive field-effect pH sensor and a thin-film Pt-temperature sensor. Due to the multi-functional properties of BST, it is utilized as final outermost coating layer of the processed sensor chip and serves as passivation and protection layer as well as pH-sensitive transducer material at the same time. The results of testing of the individual sensors of the developed multi-parameter sensor chip are presented. In addition, a quasi-simultaneous multi-parameter characterization of the sensor chip in buffer solutions with different pH value and electrolyte conductivity is performed. To

study the sensor behavior and the suitability of BST as multi-functional material under harsh environmental conditions, the sensor chip was exemplarily tested in a biogas digestate.

6.2 Introduction

The development of miniaturized sensor systems and monolithic sensor arrays for (bio-)chemical analysis has been in the focus of scientific and commercial interests in the field of analytical chemistry [1], biotechnology, medicine [2–4], environmental monitoring and industrial process control in the last decades. A review of recent advances in miniaturized sensor systems can be found in [5]. Such monolithic sensor arrays integrate several sensors on one chip configured for the detection and control of various combinations of (bio-)chemical and physical parameters such as pH value, analyte concentration, electrolyte conductivity, temperature, pressure, flow rate and many more. Often, these systems are based on different transducer principles and require a wide variety of sensitive materials and processes. The production of such integrated sensor systems necessitates complex manufacturing processes including a restriction in materials and the limited choice in fabrication processes and steps. On the other hand, monolithic sensor arrays offer unprecedented advantages over discrete sensors with regard to increased functionality and flexibility as well as reduced sizes and costs [5–7].

Perovskite oxides have been known for their outstanding, multi-functional properties (ferroelectric, dielectric, electro-optic and piezoelectric) providing a manifold of applications including dynamic access memories, decoupling capacitors and tunable devices [8]. Even though these perovskites exhibit a number of important device applications, their full potential needs to be further exploited. Recently, perovskite oxides have aroused increasing attention as catalytically active multi-functional materials in the field of (bio-)chemical sensors. Some of such virgin application frontiers for perovskite oxides of different compositions include, for instance, pH sensing [9–13], hydrogen peroxide [14–16] and hydrocarbon detection [17]. One of the most popular and intensively studied multi-functional perovskite-oxide materials is barium strontium titanate [18]. In previous experiments, the BST films have been applied for the detection of humidity [19, 20], for the detection of hydrogen [21] and ammonia gas [22] or for the development of single sensors sensitive to pH [23, 24].

In the present work, a Si-based sensor chip covered with a high-k BST layer has been developed for a quasi-simultaneous multi-parameter detection of pH, electrolyte conductivity and temperature. The chip combines a four-electrode capacitively-coupled contactless electrolyte-conductivity detection (so-called C^4D) sensor, a capacitive field-effect electrolyte-insulator-semiconductor (EIS) pH

sensor and a thin-film Pt temperature sensor. All sensors were covered with the same BST film prepared by means of pulsed laser deposition (PLD). The role of the BST layer is of multi-purpose: It serves as a pH-sensitive transducer material for the field-effect pH sensor, as an insulator layer for developing the contactless conductivity sensor, and as passivation layer, which protects the metal electrodes of the conductivity and temperature sensors from corrosion, contamination and fouling.

The results of testing of the individual sensors of the developed multi-parameter sensor chip are presented. In addition, a combined characterization of the sensor chip in buffer solutions with different pH value and electrolyte conductivity is performed. To study the sensor behavior and the suitability of BST as multi-functional material under harsh environmental conditions, the sensor was exemplarily tested in a biogas digestate.

6.3 Fabrication of the multi-parameter sensor chip

Figure 6.1 shows the schematic cross section (a) and the top view (b) of the

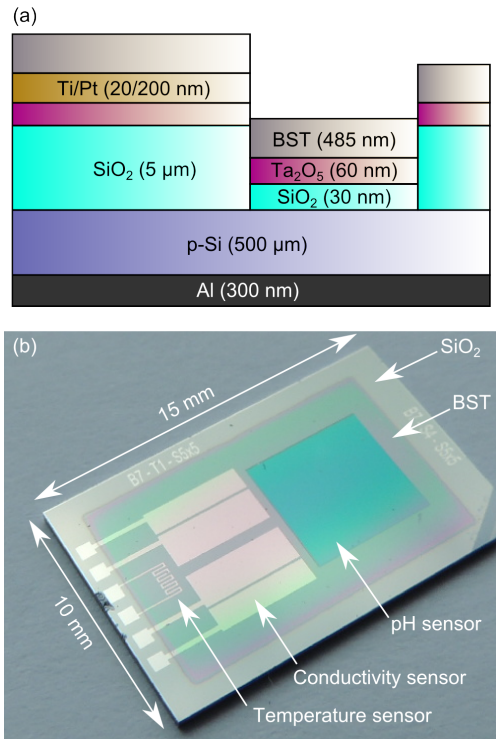

Figure 6.1: Schematic cross section (a) and top view (b) of the prepared multi-parameter sensor chip coated with BST layer as multi-purpose material.

fabricated multi-parameter sensor chip. The developed multi-parameter sensor chip combines three sensors for measuring the conductivity, the pH value and the temperature, thus, integrating different transducer principles on one single chip. Four thin-film Pt electrodes were used as an electrolyte-conductivity sensor. Each of the four electrodes had a length of 4 mm and a width of 1.5 mm and 1.0 mm for the inner and outer electrodes, respectively. The inter-electrode spacing between the inner electrodes was 0.5 mm and the gap between the inner and outer electrodes was 0.1 mm. As pH sensor served a field-effect capacitive EIS sensor consisting of an Al-p-Si-SiO_2-Ta_2O_5-BST structure with a BST layer as pH-sensitive material. The temperature sensor was designed as meander-shaped Pt electrode with a length of 1450 µm, a width of 600 µm, a finger gap of 90 µm and a finger width of 60 µm.

All three sensors were fabricated on a commercially available four-inch Si-SiO_2 wafer (525 µm thick p-Si, resistivity 1 Ω cm to 5 Ω cm, 5 µm thick SiO_2, from Siegert Wafer GmbH, Germany). A thick SiO_2 layer was used for the following two reasons: (i) to reduce the influence of the parasitic capacitance of the SiO_2 and the Si resistance on the electrolyte-conductivity sensor and, (ii) to eliminate possible cross-effects on the pH sensor caused from the electrolyte-conductivity or temperature sensor. For these reasons, the pH sensor was buried in this thick SiO_2 layer.

Initially, a photolithographic step was performed to define the gate area of the field-effect pH sensor. The 5 µm thick SiO_2 layer was etched in hydrofluoric acid for about 60 min for opening the gate area with dimensions of 5 mm × 5 mm. In a next step, a double-layer gate insulator of SiO_2-Ta_2O_5 was fabricated. The high-quality 30 nm SiO_2 was thermally grown by dry oxidation of Si at 1000 °C in O_2 atmosphere for 30 min. The Ta_2O_5 films were prepared by means of thermal oxidation of an electron-beam evaporated 30 nm thick tantalum layer in dry oxygen atmosphere at 520 °C for about 45 min, resulting in a ∼ 60 nm thick Ta_2O_5 layer. To complete the fabrication of the pH sensor, the rear side of the SiO_2 wafer was etched and then, a 300 nm Al film was deposited as a contact layer. A second photolithographic step was performed for preparation of the conductivity and the temperature sensor. A thin layer of ∼20 nm Ti served as adhesion layer and ∼200 nm Pt as electrode material were deposited by means of electron-beam evaporation followed by a lift-off-process.

The processed wafer was diced into separate chips (chip size: 10 mm × 15 mm). These chips were covered with the BST layer to complete the fabrication process of the multi-parameter sensor chip. The BST films (∼485 nm) of $Ba_{0.25}Sr_{0.75}TiO_3$ composition were prepared by PLD technique by using targets fabricated via the self-propagating high-temperature synthesis (SHS) method. The process steps of the BST synthesis are described in detail in [24]. To protect the bond pads of the

conductivity and temperature sensor, the BST films were deposited using a Si-shadow mask. The deposition was performed in an oxygen atmosphere (gas flow 30 ml/min, pressure 2×10^{-3} mbar) using a KrF-excimer laser (Lambda LPX305) with a pulse width of 20 ns and a pulse energy of approximately 1 J per pulse. When using a deposition time of 300 s, an energy density of 2.5 J/cm^2 and a repetition rate of 10 Hz, the BST layer thickness amounted approximately to 485 nm. Finally, the multi-parameter sensor chip coated with BST was mounted on a printed circuit board (PCB), followed by ultrasonic wire bonding and encapsulation processes.

For electrochemical characterization, the PCB substrate was mounted in a home-made measuring cell and the sensor chip was sealed by an O-ring. The pH sensor was contacted on its front side by the electrolyte and a reference electrode (conventional liquid-junction Ag/AgCl electrode, Metrohm), and on its rear side by a gold-plated pin.

6.4 Physical characterization of the BST layer

Physical properties (stoichiometry, thickness and surface morphology) of the BST layer have been investigated by Rutherford backscattering spectrometry (RBS), scanning electron microscopy (SEM) and atomic force microscopy (AFM). For this, separate chips consisting of p-Si-SiO_2-Ti-Pt structure covered with BST layer were fabricated. RBS measurements were performed using 1.4 MeV H^+ ions. Figure 6.2 depicts a typical RBS energy spectrum of a BST layer deposited on a Si

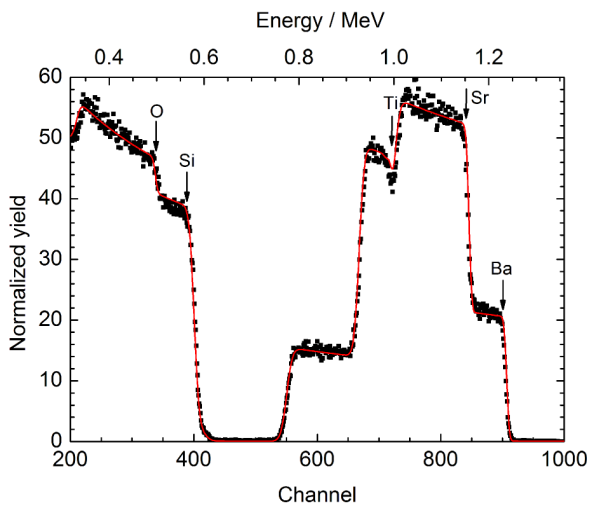

Figure 6.2: RBS measurement of a $Ba_{0.25}Sr_{0.75}TiO_3$ film deposited on a Si substrate. Simulation (solid line) is compared to experimental data (full squares).

substrate. The measured RBS spectrum is in good agreement with the simulation performed with Rutherford Universal Manipulation Program (RUMP) [25]. Clear steps corresponding to the constituent elements (Ba, Sr, Ti, O) were detected. The energy edges of the particular elements are indicated by arrows. The analysis of the RBS measurement verifies the stoichiometric composition to the deposited $Ba_{0.25}Sr_{0.75}TiO_3$.

To explore whether the BST film completely covers the Pt electrodes of the conductivity and temperature sensor, a cross-sectional SEM analysis of the Si-SiO_2-Ti-Pt-BST layer stack at the electrode transition region was conducted, which is presented in Fig. 6.3. This SEM image was obtained using focus-ion beam (FIB

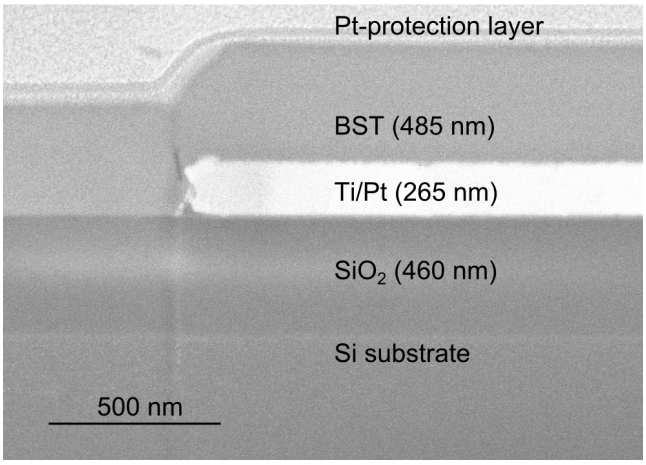

Figure 6.3: Cross-sectional SEM picture of a Si-SiO_2-Ti-Pt-BST layer stack at the electrode transition region.

Helios 600, FEI) for sample preparation resulting in perpendicular profiles. For this procedure, an additional protective Pt film was deposited on top of the BST layer. The image shows the layer stack p-Si-SiO_2-Ti-Pt-BST and the transition region between electrode edge and the substrate material. As can be clearly seen, the BST layer is completely closed over the sensor structure.

Figure 6.4 illustrates AFM height (a) and phase (b) micrographs of the surface of the prepared BST film with a scan area of 2 µm × 2 µm. They were recorded in the tapping mode using a BioMat Workstation (JPK Instruments, Germany). The micrographs show a closed BST-thin film without micro-cracks or pores. The thin film has a smooth surface with an average surface roughness of 1.3 nm. The BST surface possesses a grainy texture with a typical grain size of ∼50 nm.

For the determination of the dielectric constant of the BST layer, separate capacitive metal-insulator-metal structures with BST films sandwiched between bottom and top Pt electrodes were prepared. A dielectric constant for the 485 nm

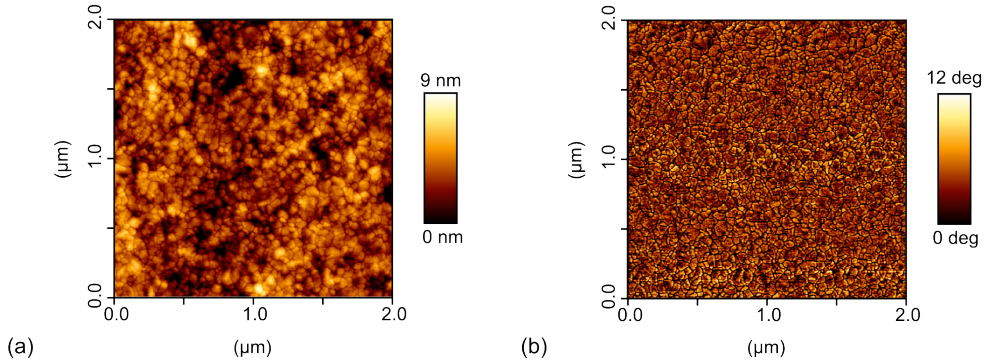

Figure 6.4: AFM height (a) and phase (b) image with a scan size of 2 µm × 2 µm recorded in the tapping mode. The BST image reveals a smooth and homogeneous surface.

thick BST film was found to be around 260 ± 8 that is in good agreement with results reported for a PLD-deposited 450 nm thick BST layer [26].

6.5 Results and discussion

Before the quasi-simultaneous measurement with the BST-based multi-parameter sensor chip was performed, each sensor was characterized individually. The sensors' functioning principle and measuring procedure will be briefly described in the corresponding sections.

6.5.1 Characterization of the conductivity sensor

Electrolyte-conductivity measurements are usually conducted using nearly ideally polarized, inert metal electrodes such as platinum or gold, which are in direct contact with the electrolyte. Especially in harsh and aggressive environments, the effect of redox processes, bubble formation due to electrolysis, as well as contamination and fouling of electrodes during continuous use are frequent problems [27–30]. These problems can be overcome, when the electrodes are electrically insulated from the electrolyte solution by covering them with a protective layer. The sensor couples capacitively with the electrolyte, which is known as capacitively coupled contactless conductivity detection (C^4D). However, due to the additional capacitance of the protective layer that is usually much lower than the double-layer capacitance of non-protected electrodes, the electrode impedance is increased [29, 31]. As a consequence, C^4D sensors usually exhibit a lower sensitivity when compared to conventional contact-mode conductivity detection. To find a compromise, the protective material should exhibit a high permittivity in

order to reduce the electrode impedance. These requirements are met by the high-k BST thin film.

The electrolyte-conductivity sensor with the protective BST layer was characterized in a four-electrode configuration. In the four-electrode configuration, the two outer electrodes were used as current-driving electrodes (applying an alternating current of 20 µA), while the two inner electrodes were used as potential-sensing electrodes. For characterization, the sensor was exposed to different commercially available electrolyte-conductivity standard solutions ranging from 0.084 mS/cm to 50 mS/cm. Impedance spectra were recorded with an impedance analyzer module (Zennium, Zahner Elektrik GmbH, Germany) covering a frequency range from 1 Hz to 100 kHz. Since electrolyte conductivity is strongly dependent on temperature, all measurements were performed at a constant temperature of 25 °C in a Faraday cage.

In Fig. 6.5, the impedance spectra of the BST-based C^4D sensor measured in a four-electrode configuration are presented. The sensor exhibits a wide resistive plateau over more than four frequency decades. This is advantageous because the electrolyte resistance R_{el} can be determined at a wide frequency range. In Fig. 6.6, the electrolyte conductance is plotted as a function of the electrolyte conductivity. The calibration curve is obtained from the Bode plot in Fig. 6.5 at a frequency of 500 Hz. As can be seen, the developed four-electrode C^4D based on BST shows an excellent linearity (dashed line) with a correlation coefficient of 0.999 over a wide range of electrolyte conductivities. From the inverse of the

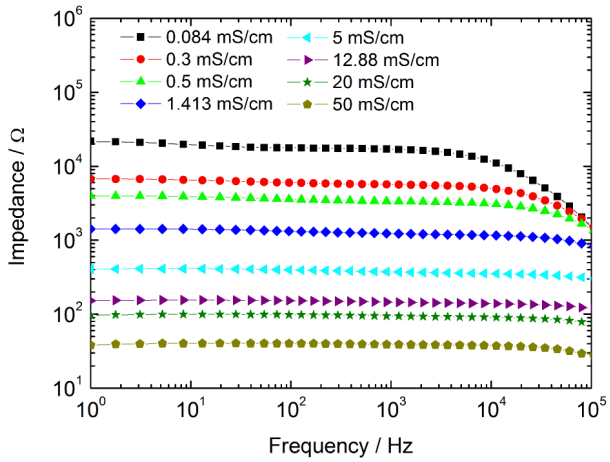

Figure 6.5: Bode plot of the modulus of impedance as a function of frequency of the C^4D sensor with 485 nm BST as protective layer recorded in a four-electrode setup in various conductivity standard solutions.

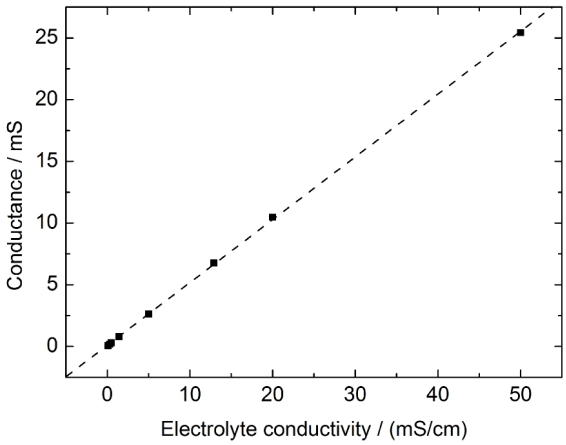

Figure 6.6: Conductance as a function of the electrolyte conductivity measured with the C^4D sensor. The calibration curve is obtained from the Bode plot in Fig. 6.5 at 500 Hz.

slope of this curve the cell constant has been calculated to be 1.99 cm^{-1}.

6.5.2 Characterization of the pH sensor

In [24], it has been demonstrated that BST exhibits excellent pH-sensitive characteristics. Thus, the BST coating is used as an alternative gate material for the capacitive field-effect pH sensor.

The field-effect capacitive electrolyte-BST-insulator-semiconductor structure was characterized in different pH buffer solutions (from pH 3 to pH 11) in terms of its intrinsic sensor characteristics such as pH sensitivity and hysteresis. For operation, a DC (direct current) polarization voltage is applied via a conventional Ag/AgCl reference electrode and the rear-side Al contact of the chip to set the working point of the sensor. A small AC (alternating current) voltage (20 mV) is applied to the system in order to measure the capacitance of the sensor. The sensor output signal was read out in the constant-capacitance (ConCap) mode using an impedance analyzer (Zennium, Zahner Elektrik GmbH, Germany). The ConCap mode allows the dynamic characterization of the sensor.

Figure 6.7 exemplarily demonstrates the dynamic pH response of the capacitive field-effect sensor recorded in different pH Titrisol buffer solutions at a frequency of 120 Hz. The sensor signal depicts a clear dependence of the pH value of the solution within the pH-loop cycle. In the range from pH 3 to pH 11 the field-effect sensor exhibits a high pH sensitivity of 57.4 mV/pH with a small hysteresis of less than 2 mV. That is comparable with values reported for Si_3N_4 (54 mV/pH [32, 33]),

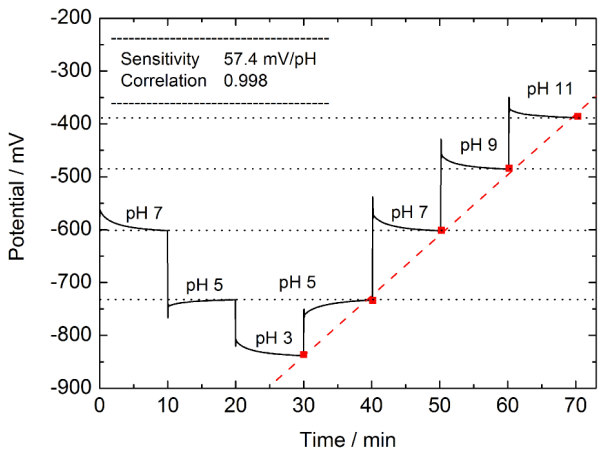

Figure 6.7: Typical ConCap response of the BST-based capacitive field-effect pH sensor.

Al_2O_3 (49 – 57 mV/pH [34]) and Ta_2O_5 (55 – 59 mV/pH [35–37]) films, which have often been utilized as pH-sensitive transducer material in ion-sensitive field-effect transistors or capacitive field-effect sensors. The hysteresis was less than 2 mV (or 0.035 pH).

6.5.3 Characterization of the temperature sensor

A stable passivation is also needed for the temperature sensor to avoid corrosion of the electrodes. Electrode corrosion leads to an increase in the specific resistivity and loss of the Ohmic characteristics of the temperature sensor.

The temperature sensor was characterized at various temperatures using a temperature-controlled water bath (RCS 6, Lauda Dr. R. Wobser GmbH & Co KG, Germany) filled with distilled water. The resistance of the meander-shaped Pt structure was determined with a multimeter (2700 Multimeter, Keithley Instruments) in the temperature range between 20 °C and 40 °C increasing the temperature in 5 °C steps.

In Fig. 6.8, the calibration curve of the temperature sensor passivated with BST is presented. The sensor exhibits a linear calibration curve with a temperature coefficient of 0.0034 $°C^{-1}$. The nominal resistance R_0 at 0 °C was 98.3 Ω.

6.5.4 Combined measurement in buffer solution and biogas digestate

To investigate the proper independent functioning of the individual sensors, the developed multi-parameter sensor chip was characterized in three buffer solutions

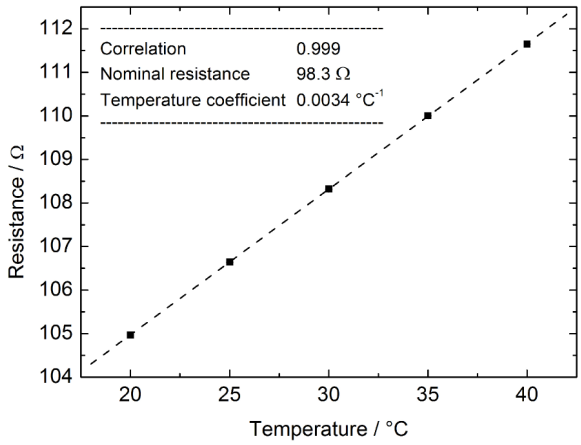

Figure 6.8: Calibration curve of the meander-shaped Pt temperature sensor coated with BST.

with different electrolyte conductivities and pH values. Finally, the sensor was immersed to digestate to test its feasibility under real conditions.

The digestion process is usually performed at constant temperature, as temperature changes or fluctuations effect the biogas production negatively. To create comparable conditions, the entire measurement was conducted in a thermostated oven to maintain a constant temperature of 37 °C during the experiment. Table 6.1 gives an overview of the different solutions used and their conductivity and pH value at a temperature of 37 °C. The first three solutions (A to C) are commercially available Titrisol buffer solutions (Merck, Germany) whose conductivity and pH value were adjusted if necessary with KCl and NaOH, respectively. The digestate was gathered from a laboratory-scale anaerobic digester. The plant is working under mesophilic temperature conditions (37 °C) containing solely manure from

Table 6.1: Overview of the used solutions and their conductivity and pH value at a temperature of 37 °C. These values were determined before and after each measurement with commercial electrodes as a reference.

Solution	Conductivity / (mS/cm)	pH value
A	14.0 ± 0.1	7.31 ± 0.02
B	20.3 ± 0.1	6.98 ± 0.02
C	20.3 ± 0.1	8.87 ± 0.02
Digestate	8.0 ± 0.1	7.08 ± 0.02

dairy cows. In order to turn down the metabolism of the organisms in the digestate, it was collected from the plant and then stored at room temperature until use. Thus, the organisms were fully fermented and no fluctuations in conductivity and pH value were expected to be measured when applied to the sensor. The conductivity and pH values of the three solutions and of the digestate sample were determined with a commercial conductivity (Mettler Toledo, InLab@731) and pH-glass electrode (Hamilton, Double Pore) before exposing the multi-parameter sensor chip to the solutions and after measurements.

Afore performing the quasi-simultaneous measurement, the conductivity, pH and temperature sensors of the multi-parameter sensor chip coated with BST were calibrated by means of a two-point calibration. The conductivity sensor was calibrated using 12.88 mS/cm and 20 mS/cm conductivity standards, respectively. Standard buffer solutions of pH 7 and pH 9 were used to calibrate the pH sensor at 37 °C. The temperature sensor was calibrated by means of a heating ramp ranging from 37 °C up to 50 °C. The obtained calibration data were utilized to convert the raw signals into the physical quantities.

During experiment, the multi-parameter sensor chip was first exposed to three different buffer solutions to demonstrate the general functioning of the sensor chip and finally to digestate. The output signals of the three sensors were readout sequentially (quasi-simultaneously). All devices were triggered in a multiplexed manner using a custom-developed software in LabVIEW.

In Fig. 6.9, the quasi-simultaneous measurement of conductivity, pH value and temperature conducted with the multi-parameter sensor chip coated with BST over a time span of 20 hours is presented. The measuring curves were obtained by converting the data into physical quantities using the calibration results for each particular sensor. As can be seen, there is no cross-talk between the sensors on the chip. All three sensor parts exhibit a very stable sensor signal for each sample solution over a time span of 5 hours. Besides the temperature drops due to door opening other deviations from the target temperature are mainly attributed to the unsteadiness of the control loop of the thermostated oven, which is specified as steady within ±0.2 °C.

6.6 Conclusions

The multi-parameter sensor chip combining electrolyte conductivity, pH and temperature sensor and using BST as multi-purpose material has been developed. The individual sensors on the chip have been tested in terms of their intrinsic sensor properties. The four-electrode electrolyte-conductivity sensor exhibits excellent linearity in a wide range of electrolyte conductivities from 0.084 mS/cm to 50 mS/cm. The pH sensor shows a nearly-Nernstian pH sensitivity

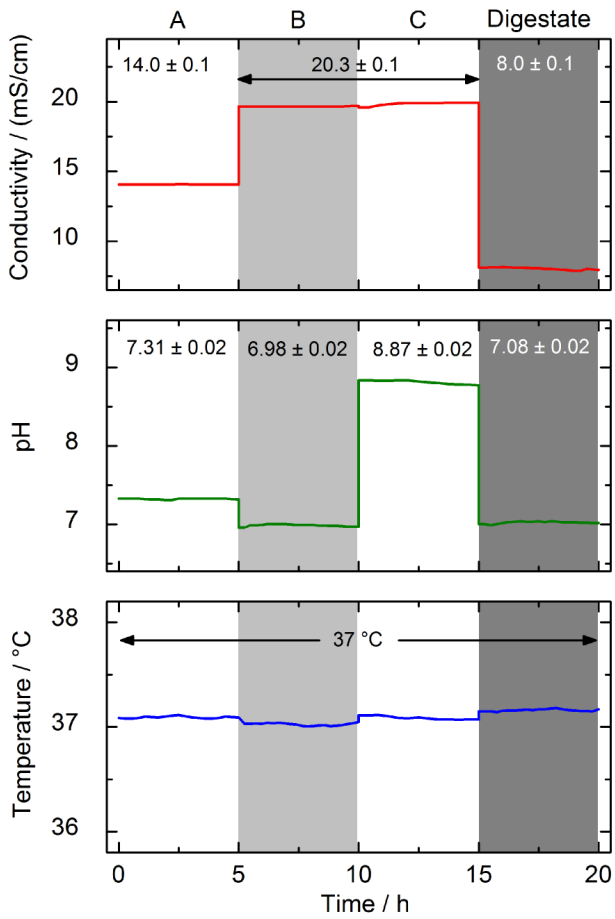

Figure 6.9: Measurement of conductivity (top), pH value (middle) and temperature (bottom) with the multi-parameter sensor chip coated with BST as multi-purpose material.

of S = 57.4 mV/pH in the range from pH 3 to pH 11. The temperature sensor possesses a linear temperature calibration curve in the temperature range of 20 – 40 °C with a temperature coefficient of $\alpha = 0.0034\,^{\circ}\mathrm{C}^{-1}$.

In addition, the developed chip with three combined sensors was quasi-simultaneously characterized in a sequentially scheduling manner in buffer solutions with different electrolyte conductivity and pH values as well as in biogas digestate.

Advantageously, the BST-protected C^4D sensor allows the use of cheaper electrode materials such as, for instance, Al films instead of noble metals. Furthermore, the problems associated with contact-mode EC detection techniques, can be eliminated or at least minimized. This enhances the life-time of conductivity

sensors considerably.

The obtained results demonstrate the feasibility of the developed sensor chip with BST layer as multi-functional material. A potential application of this kind of sensor could be in the field of process control for biogas fermentation. Biogas production by anaerobic digestion has gained increased importance for reducing the volume of agricultural waste and supplying carbon neutral fuel for energy generation. The anaerobic degradation of organic materials is known to be a highly complex multi-step process, which is influenced by various microbiological, chemical and physical factors [38]. The process control therefore requires the acquisition of various metrics such as fatty acid concentration, pH, temperature and buffer capacity in order to gain information about the process flow. Further applications could be in the field of water-quality control or cell-culture fermentation.

6.7 Acknowledgments

The authors gratefully thank H.-P. Bochem for performing the SEM analysis and H. Iken and M. Leinhos for chip fabrication. Furthermore, the authors thank the Institute NOWUM-energy for providing digestate from their laboratory-scale reactors. C. Huck thanks FH Aachen for the Ph.D. scholarship. V. V. Buniatyan thanks the State Committee of Science MES RA (Grant SCS-13-2G032) for financial support. Part of this project is co-financed by the European Union (ERDF), "The Commission investing in your future".

6.8 Bibliography

[1] Norlin, P.; Öhman, O.; Ekström, B.; Forssén, L.: A chemical micro analysis system for the measurement of pressure, flow rate, temperature, conductivity, UV-absorption and fluorescence. *Sensors and Actuators B: Chemical* 49 (1998), No. 1-2, p. 34–39

[2] Lauwers, E.; Suls, J.; Gumbrecht, W.; Maes, D.; Gielen, G.; Sansen, W.: A CMOS multiparameter biochemical microsensor with temperature control and signal interfacing. *IEEE Journal of Solid-State Circuits* 36 (2001), No. 12, p. 2030–2038

[3] Gumbrecht, W.; Peters, D.; Schelter, W.; Erhardt, W.; Henke, J.; Steil, J.; Sykora, U.: Integrated pO_2, pCO_2, pH sensor system for online blood monitoring. *Sensors and Actuators B: Chemical* 19 (1994), No. 1-3, p. 704–708

[4] Schelter, W.; Gumbrecht, W.; Montag, B.; Sykora, U.; Erhardt, W.: Combination of amperometric and potentiometric sensor principles for on-line blood monitoring. *Sensors and Actuators B: Chemical* 6 (1992), No. 1-3, p. 91–95

[5] Hierlemann, A.; Gutierrez-Osuna, R.: Higher-order chemical sensing. *Chemical Reviews* 108 (2008), No. 2, p. 563–613

[6] Poghossian, A.; Schultze, J. W.; Schöning, M. J.: Multi-parameter detection of (bio-)chemical and physical quantities using an identical transducer principle. *Sensors and Actuators B: Chemical* 91 (2003), No. 1-3, p. 83–91

[7] Kloock, J. P.; Moreno, L.; Bratov, A.; Huachupoma, S.; Xu, J.; Wagner, T.; Yoshinobu, T.; Ermolenko, Y.; Vlasov, Y. G.; Schöning, M. J.: PLD-prepared cadmium sensors based on chalcogenide glasses – ISFET, LAPS and μISE semiconductor structures. *Sensors and Actuators B: Chemical* 118 (2006), No. 1-2, p. 149–155

[8] Gevorgian, S.; Vorobiev, A.; Lewin, T.: DC field and temperature dependent acoustic resonances in parallel-plate capacitors based on $SrTiO_3$ and $Ba_{0.25}Sr_{0.75}TiO_3$ films: Experiment and modeling. *Journal of Applied Physics* 99 (2006), No. 12, p. 124112(1–11)

[9] Jan, S.-S.; Chen, Y.-C.; Chou, J.-C.: Effect of Mg_2^+-dopant on the characteristics of lead titanate sensing membrane for ion-sensitive field-effect transistors. *Sensors and Actuators B: Chemical* 108 (2005), No. 1–2, p. 883–887

[10] Jhan, S.-S.; Chiang, J.-L.; Chen, Y.-C.; Chou, J.-C.; Su, J.-F.: Design and fabrication of pH fetecting system using lead titanate series gate ion-sensitive field effect transistors. *Ferroelectrics* 383 (2009), No. 1, p. 111–118

[11] Pan, T.-M.; Liao, K.-M.: Comparison of structural and sensing characteristics of Pr_2O_3 and $PrTiO_3$ sensing membrane for pH-ISFET application. *Sensors and Actuators B: Chemical* 133 (2008), No. 1, p. 97–104

[12] Pham, Q. N.; Bohnke, C.; Emery, J.; Bohnke, O.; Le Berre, F.; Crosnier-Lopez, M.-P.; Fourquet, J.-L.; Florian, P.: A new perovskite phase LiCaTaO: Li ion conductivity and use as pH sensor. *Solid State Ionics* 176 (2005), No. 5-6, p. 495–504

[13] Roffat, M.; Noël, O.; Soppera, O.; Bohnke, O.: Investigation of the perovskite ceramic $Li_{0.30}La_{0.56}TiO_3$ by pulsed force mode AFM for pH sensor application. *Sensors and Actuators B: Chemical* 138 (2009), No. 1, p. 193–200

[14] Wang, G.; Bao, Y.; Tian, Y.; Xia, J.; Cao, D.: Electrocatalytic activity of perovskite $La_{1-x}Sr_xMnO_3$ towards hydrogen peroxide reduction in alkaline medium. *Journal of Power Sources* 195 (2010), No. 19, p. 6463–6467

[15] He, X.; Hu, C.; Xi, Y.; Wan, B.; Xia, C.: Electroless deposition of $BaTiO_3$ nanocubes for electrochemical sensing. *Sensors and Actuators B: Chemical* 137 (2009), No. 1, p. 62–66

[16] Luque, G. L.; Ferreyra, N. F.; Leyva, A. G.; Rivas, G. A.: Characterization of carbon paste electrodes modified with manganese based perovskites-type oxides from the amperometric determination of hydrogen peroxide. *Sensors and Actuators B: Chemical* 142 (2009), No. 1, p. 331–336

[17] Sahner, K.; Moos, R.: Modeling of hydrocarbon sensors based on p-type semiconducting perovskites. *Physical Chemistry Chemical Physics* 9 (2007), No. 5, p. 635–642

[18] Zhu, W.; Tan, O. K.; Yao, X.: Amorphous ferroelectric ($Ba_{0.67}Sr_{0.33}Ti_{1.02}O_3$ thin films with enhanced H_2 induced interfacial polarization potential. *Journal of Applied Physics* 84 (1998), No. 9, p. 5134–5139

[19] Agarwal, S.; Sharma, G. L.; Manchanda, R.: Electrical conduction in (Ba, Sr)TiO_3 thin film MIS capacitor under humid conditions. *Solid State Communications* 119 (2001), No. 12, p. 681–686

[20] Agarwal, S.; Sharma, G. L.: Humidity sensing properties of (Ba, Sr) TiO_3 thin films grown by hydrothermal–electrochemical method. *Sensors and Actuators B: Chemical* 85 (2002), No. 3, p. 205–211

[21] Zhu, W.; Tan, O. K.; Yan, Q.; Oh, J. T.: Microstructure and hydrogen gas sensitivity of amorphous (Ba,Sr)TiO_3 thin film sensors. *Sensors and Actuators B: Chemical* 65 (2000), No. 1-3, p. 366–370

[22] Roy, S. C.; Sharma, G. L.; Bhatnagar, M. C.; Samanta, S. B.: Novel ammonia-sensing phenomena in sol–gel derived $Ba_{0.5}Sr_{0.5}TiO_3$ thin films. *Sensors and Actuators B: Chemical* 110 (2005), No. 2, p. 299–303

[23] Chen, C.-Y.; Chou, J.-C.; Chou, H.-T.: pH sensing of $Ba_{0.7}Sr_{0.3}TiO_3/SiO_2$ film for metal-oxide-semiconductor and ion-sensitive field-effect transistor devices. *Journal of The Electrochemical Society* 156 (2009), No. 6, p. G59–G64

[24] Buniatyan, V. V.; Abouzar, M. H.; Martirosyan, N. W.; Schubert, J.; Gevorgian, S.; Schöning, M. J.; Poghossian, A.: pH-sensitive properties of barium strontium titanate (BST) thin films prepared by pulsed laser deposition technique. *Physica Status Solidi A* 207 (2010), No. 4, p. 824–830

[25] Doolittle, L. R.: A semiautomatic algorithm for Rutherford backscattering analysis. *Nuclear Instruments and Methods in Physics Research Section B: Beam Interactions with Materials and Atoms* 15 (1986), No. 1–6, p. 227–231

[26] Kim, S.-G.; Mah, S.-B.; Jang, N.-W.; Paik, D.-S.; Park, C.-Y.: Post-annealing in oxygen ambient for (Ba,Sr)TiO_3 thin films prepared by pulsed laser deposition. *Materials Letters* 43 (2000), No. 5-6, p. 254–258

[27] Bousse, L.; Bergveld, P.: On the impedance of the silicon dioxide/electrolyte interface. *Journal of Electroanalytical Chemistry* 152 (1983), No. 1-2, p. 25–39

[28] Rana, S.; Page, R. H.; McNeil, C. J.: Impedance spectra analysis to characterize interdigitated electrodes as electrochemical sensors. *Electrochimica Acta* 56 (2011), No. 24, p. 8559–8563

[29] Laugere, F.; Lubking, G.; Berthold, A.; Bastemeijer, J.; Vellekoop, M. J.: Downscaling aspects of a conductivity detector for application in on-chip capillary electrophoresis. *Sensors and Actuators A: Physical* 92 (2001), No. 1-3, p. 109–114

[30] Olthuis, W.; Volanschi, A.; Bomer, J.; Bergveld, P.: A new probe for measuring electrolytic conductance. *Sensors and Actuators B: Chemical* 13 (1993), No. 1-3, p. 230–233

[31] Olthuis, W.; Sprenkels, A.; Bomer, J.; Bergveld, P.: Planar interdigitated electrolyte-conductivity sensors on an insulating substrate covered with Ta_2O_5. *Sensors and Actuators B: Chemical* 43 (1997), No. 1-3, p. 211–216

[32] Orozco, J.; Baldi, A.; Baena, R.; Cadarso, A.; Bratov, A.; Jimenez, C.: Portable system based on microsensors for environmental monitoring applications. *Measurement Science and Technology* 18 (2007), No. 3, p. 935–940

[33] Poghossian, A.; Thust, M.; Schöning, M. J.; Müller-Veggian, M.; Kordos, P.; Lüth, H.: Cross-sensitivity of a capacitive penicillin sensor combined with a diffusion barrier. *Sensors and Actuators B: Chemical* 68 (2000), No. 1-3, p. 260–265

[34] Cané, C.; Gràcia, I.; Merlos, A.: Microtechnologies for pH ISFET chemical sensors. *Microelectronics Journal* 28 (1997), No. 4, p. 389–405

[35] Poghossian, A.: The super-Nernstian pH sensitivity of Ta_2O_5-gate ISFETs. *Sensors and Actuators B: Chemical* 7 (1992), No. 1-3, p. 367–370

[36] Schöning, M. J.; Näther, N.; Auger, V.; Poghossian, A.; Koudelka-Hep, M.: Miniaturised flow-through cell with integrated capacitive EIS sensor fabricated at wafer level using Si and SU-8 technologies. *Sensors and Actuators B: Chemical* 108 (2005), No. 1-2, p. 986–992

[37] Poghossian, A.; Baade, A.; Emons, H.; Schöning, M. J.: Application of ISFETs for pH measurement in rain droplets. *Sensors and Actuators B: Chemical* 76 (2001), No. 1-3, p. 634–638

[38] Weiland, P.: Biogas production: Current state and perspectives. *Applied Microbiology and Biotechnology* 85 (2010), No. 4, p. 849–860

7 Concluding remarks and perspectives

The anaerobic digestion process is complex and sensitive to changes in environmental conditions. Understanding the process behavior is essential for proper reactor operation, diagnosis as well as problem-solving of the process. In this context, reliable monitoring of the biogas production process has risen great attention, as it is a necessary requirement for process control and consequently, improves process performance and economy of the biogas plant. This work aimed at the design and development of miniaturized solid-state transducers and their use as physico-chemical sensors to be applied for the measurement and monitoring of several parameters in biogas digesters. The parameters of interest were early warning parameters such as the dissolved hydrogen concentration and the metabolic activity as well as state variables including electrolyte conductivity, pH value and temperature. For this, sensor structures based on different transducer principles, namely amperometry, potentiometry and conductometry have been designed and fabricated by means of standard silicon technology.

A combined amperometric/field-effect H_2 sensor for the detection of the dissolved hydrogen has been studied for the first time. The independent functioning of both transducer principles of the combined sensor as well as the feasibility of the presented approach for the simultaneous detection of dissolved H_2 concentrations in electrolyte solutions have been demonstrated. Both, the amperometric and the field-effect transducer showed a linear response behavior in the H_2 concentration range from 0.1 to 3 % (v/v) with a slope of (198.4 ± 13.7) nA/% (v/v) and (14.9 ± 0.5) mV/% (v/v), respectively. Such a combination of two transducer principles might allow a more accurate, selective and reliable measurement of dissolved H_2 in biogas reactors as the sensors signal is considered as H_2 signal only if the field-effect transducer responds as well.

To overcome possible problems related to the functioning of the combined sensor in real biogas broths, future work should be directed to a direct coupling of the sensor setup with a biogas reactor via a bypass system filled with a suitable buffer solution, which will be separated from the biogas medium by a H_2-permeable membrane. In this way, the selectivity, life-time and signal-to-noise ratio of the combined sensor can be improved. Moreover, to achieve a high output signal for the field-effect pH sensor, the bypass system can be filled with an appropriate inner electrolyte solution with low pH buffer capacity. For a relatively small response time of this device, the H_2-permeable membrane should be as close as

possible to the working electrode of the amperometric-sensing part. In order to do this, further development of miniaturized reference electrodes with long-term stability should be in the focus of future research activities.

The capacitive field-effect sensor has been proven to be a versatile platform for monitoring the metabolic activity of organisms. Metabolic responses of the model bacterium *E. coli* in suspension layered onto the field-effect structure have been successfully studied to pulses of glucose as nutrient. It was found that acidification of the surrounding medium took place immediately after glucose addition and followed a Michaelis-Menten-like kinetic behavior as a function of the glucose concentration. A new protocol to immobilize *E. coli* bacteria by gel entrapment directly onto the chip was developed. The immobilization as well as the construction of a measuring cell allowed to operate four sensors at the same time in a differential-mode measurement setup and thereby, circumventing external influences such as sensor drift, temperature fluctuations and external pH changes. This biosensor was further exploited towards glucose and acetate pulses with *E. coli* bacteria grown by a specific cultivation strategy. Alkalinization and acidification events due to respective acetate and glucose pulses have been demonstrated.

The oxygen dependence of the acetate metabolism of *E. coli* restricted a repeatable response behavior of the sensor system. Thus, this sensor system should be further optimized in terms of a reduction of the gel thickness, which would be advantageously for the diffusion rate of substrates, products and oxygen supply. Furthermore, additional oxygen flushing of the sensor system could be beneficial. In general, the capabilities of this approach could be extended to other organisms and strains that are able to metabolize relevant products of the anaerobic digestion process. This is currently subject of a continuing research project at the Institute of Nano- and Biotechnologies at the Aachen University of Applied Sciences.

The potential of high-k BST has been examined as protective layer for a miniaturized electrolyte conductivity sensor for the first time. The BST thins films were prepared by PLD technique using the targets fabricated by the SHS method. The main advantages of the PLD technique are the compatibility with silicon technology, the controlled deposition of multi-component materials in a defined stoichiometry as well as short deposition time. The SHS method is simple, energy-saving, high productive and cost-effective. For better sensor performance, planar EC and C^4D structures with Pt electrodes buried into the sensor substrate were successfully fabricated. The influence of the BST layer on the sensor characteristics was theoretically considered by means of an electrically equivalent circuit.

The impact was studied in two- and four-electrode operation modes and compared to measurements with an EC sensor without a protective BST layer in standard conductivity solutions. Both, the EC and C^4D sensor exhibited nearly identical sensor characteristics. The obtained results clearly showed the benefits of the use of the BST-based C^4D sensor in a four-electrode configuration for contactless conductivity measurements. Due to the high-k dielectric constant ($\sim$ 200) of BST and thus, the low impedance of BST, no negative impact of the protective BST layer on the conductivity sensor performance was identified. A linear dependence between the measured conductance and the electrolyte conductivity was obtained in a wide range of electrolyte conductivity from 0.3 mS/cm to 50 mS/cm. Problems associated with contact-mode EC detection techniques such as bubble formation due to electrolysis, the effect of redox processes as well as contamination and fouling of electrodes during continuous measurements can be eliminated. The minimization of these effects enhances the life-time of conductivity sensors considerably.

Bubble formation, the effect of redox processes and fouling of electrodes can only be avoided, if the BST layer is completely closed and electrically isolates the electrodes. To demonstrate the protective properties of the fabricated BST layer, the C^4D sensor has been exemplarily tested in a redox-active hexacyanoferrate solution. This should be further exploited in future in terms of long-term stability and robustness of the protective BST layer. The fabrication process of the BST layer strongly influences its micro-structural properties (e.g., morphology, high-k, leakage current). Thus, the fabrication process itself including the deposition method (e.g., PLD, RF sputtering, sol-gel method) and post-annealing treatment (e.g., time, temperature, atmosphere) of the BST layer could be another field of more applied research. For instance, a post-annealing treatment in oxygen ambient has been shown beneficial in terms of increasing the dielectric constant of BST thin films as this procedure eliminates oxygen vacancies in the as-deposited films by PLD (not published results).

In a continuing study the C^4D sensor was combined with a temperature and a pH sensor on a single chip likewise covered with BST and thus, BST has been applied for the creation of a multi-parameter sensor for liquid media for the first time. The BST layer served here as pH-sensitive transducer material for a field-effect pH sensor, as an insulation layer due to the high-k of BST for developing the contactless-conductivity sensor, and as passivation layer, which protects the metal electrodes of the conductivity and temperature sensors from corrosion, contamination and fouling. The developed chip was quasi-simultaneously characterized both in a sequentially scheduling manner in buffer solutions and in biogas digestate to test the sensor and the suitability of BST as multi-purpose material.

The multi-sensor chip was able to withstand this environment as a prerequisite for online monitoring without loss of sensor performance.

The area of application of this BST-type sensor should be further expanded to water-quality control and cell-culture or bacteria-fermentation processes. With respect to these fields, the resistance of the sensor in sterilizing- and cleaning-in-place procedures should be evaluated. Especially, due to the linking of several silicon-based sensors in a confined space, this chip opens opportunities for small-scale reactor systems.

In this work, EIS-based sensing has been largely demonstrated for many applications such as the combined amperometric/field-effect sensor for the detection of dissolved hydrogen, the cell-based sensor for the detection of the metabolic activity and the measurement of the pH value itself with the BST-modified EIS structure. In this study, Ta_2O_5 and BST have been used as pH-sensitive materials. Both materials combine practically ideal Nernstian pH sensitivity (57.4 mV/pH) and small hysteresis (less than 2 mV). In addition, these materials exhibit high corrosion-resistant properties in a wide pH range. Especially in the context of on-line monitoring, drift of these devices, which was beyond the scope of this work, is a serious issue and should still be in the focus of future research activities. Differential-mode measurements to reduce the impact of temperature influences, drift, hysteresis and other parasitic effects could be applied. Some leading companies producing ISFET-based pH electrodes (e.g., EndressHausser (Germany), Mettler-Toledo (Switzerland), Honeywell (USA)) have been achieved the fabrication of ISFETs to such a level that they exhibit performances, which are comparable with pH-glass electrodes.

List of figures

List of tables

List of abbreviations

AC	Alternating current
Acetyl-CoA	Acetyl coenzyme A
AFM	Atomic force microscopy
APS	Ammonium persulfate
ATP	Adenosine triphosphate
BST	Barium strontium titanate
C^4D	Capacitively coupled contactless conductivity detection
ConCap	Constant capacitance mode
CV	Cyclic voltammetry
DC	Direct current
DGGE	Denaturing gradient gel electrophoresis
EC	Electrolyte conductivity
EIS	Electrolyte-insulator-semiconductor
FISH	Fluorescence in-situ hybridization
G-6-P	Glucose-6-phosphate
ISE	Ion-selective electrode
ISFET	Ion-sensitive field-effect transistor
LAPS	Light-addressable potentiometric sensor
MIS	Metal-insulator-semiconductor
MOH	Amphoteric hydroxyl groups
NADH	Nicotinamide adenine dinucleotide hybrid
NIR	Near-infrared spectroscopy
PAA	Polyacrylamide
PBS	Phosphate buffer solution
PCB	Printed circuit board
PLD	Pulsed laser deposition
PTFE	Polytetrafluoroethylene
PTS	Phosphotransferase system

RBS	Rutherford backscattering spectrometry
RUMP	Rutherford universal manipulation program
SEM	Scanning electron microscopy
SHS	Self-propagating high-temperature synthesis
SMA	Specific methanogenic activity
T-RFLP	Terminal restriction fragment length polymorphism
TBS	Tris-buffered saline
TEMED	Tetramethylethylenediamine
TGGE	Temperature gradient gel electrophoresis
VFA	Volatile fatty acids
XRD	X-ray diffraction

List of symbols

α	Acidification rate
α_{max}	Maximum acidification rate
α_{S}	Dimensionless sensitivity parameter
α_{T}	Temperature coefficient
α_{t}	Transfer coefficient
β	pH-buffer capacity
β_{int}	Intrinsic surface-buffer capacity
δ	Thickness of membrane or diffusion layer in solution
$\dot{\varphi}$	Potential-change rate
ϵ_0	Dielectric constant of the vacuum
ϵ_{i}	Dielectric constant of the protective layer
ϵ_{w}	Dielectric constant of the electrolyte
Λ_{m}	Molar conductivity
Λ_{m}^0	Limiting molar conductivity
λ_+^0, λ_-^0	Limiting ionic conductivity of cations and anions
ω_{d}	Width of depletion region
ϕ_{BS}	Potential of the bulk solution

ϕ_{B}	Potential difference between the Fermi level in the bulk solution
ϕ_{M}	Potential of the metal
ϕ_{S}	Semiconductor-surface potential
σ	Electrolyte conductivity
σ_{Ref}	Specific conductivity at reference temperature
A	Effective area of the electrode or membrane
c	Concentration
$C_{\mathrm{SiO_2}}$	Capacitance of the silicon substrate
C_{b}	Capacitance between the electrodes
C_{dl}	Double-layer capacitance
C_{el}	Electrolyte capacitance
C_{FB}	Flat-band capacitance
C_{HFmin}	High-frequency minimum capacitance
C_{i}	Insulation capacitance
C_{i}	Protective layer capacitance
C_{LFmin}	Low-frequency minimum capacitance
C_{p}	Parasitic capacitance
CO_2	Carbon dioxide
D	Diffusion constant
d	Distance between the electrodes
E	Overpotential
e	Elementary charge
e^-	Electron
E_{i}	Intrinsic Fermi level
F	Faraday constant
f	Frequency
f_{high}	High cut-off frequency
f_{low}	Low cut-off frequency
G	Electrical conductance

H^+	Proton
H_2	Hydrogen
I	Current
i_{lim}	Limited current
k	Standard rate constant
k_{B}	Boltzmann constant
K_{c}	Cell constant
K_{M}	Michaelis constant
n	Number of cells
N_{A}	Avogadro constant
n_{e}	Number of electrons per molecule
O_2	Oxygen
OD	Optical density
pH_{pzc}	Point of zero charge
R	Universal gas constant
R_0	Nominal resistance
R_{el}	Electrolyte resistance
R_{sub}	Resistance of the silicon substrate
S	pH sensitivity
T	Absolute temperature
t_{A}	Acidification time
T_{Ref}	Reference temperature
V	Volume
V_{AC}	AC polarization voltage
V_{DC}	DC polarization voltage
V_{FB}	Flat-band voltage
V_{G}	Gate voltage
V_{T}	Threshold voltage
z_i	Valency of ions

Publications and conference contributions

Publications in peer-reviewed journals

- **Huck, C.**; Poghossian, A.; Kerroumi, I.; Schusser, S.; Bäcker, M.; Zander, W.; Schubert, J.; Buniatyan, V. V.; Martirosyan, N. W.; Wagner, P.; Schöning, M. J.: Multi-parameter sensor chip with barium strontium titanate as multi-purpose material. *Electroanalysis* 26 (2014) pp. 980–987

- **Huck, C.**; Poghossian, A.; Bäcker, M.; Chaudhuri, S.; Zander, W.; Schubert, J.; Begoyan, V. K.; Buniatyan, V. V.; Wagner, P.; Schöning, M. J.: Capacitively coupled electrolyte-conductivity sensor based on high-k material of barium strontium titanate. *Sensors and Actuators B: Chemical* 198 (2014) pp. 102–109

- Bäcker, M.; Kramer, F.; **Huck, C.**; Poghossian, A.; Bratov, A.; Abramova, N.; Schöning, M. J.: Planar and 3D interdigitated electrodes for biosensing applications: The impact of a dielectric barrier on the sensor properties. *Physica Status Solidi A* 211 (2014) pp. 1357–1363

- Buniatyan, V. V.; **Huck, C.**; Poghossian, A.; Aroutiouninan, A. M.; Schöning, M. J.: $Ba_xSr_{1-x}TiO_3$/pc-Si heterojunction capacitance. *Armenian Journal of Physics* 6 (2013) pp. 177–187

- Buniatyan, V. V.; **Huck, C.**; Poghossian, A.; Aroutiouninan, A. M.; Schöning, M. J.: $Ba_xSr_{1-x}TiO_3$/pc-Si heterojunction capacitance. *Armenian Journal of Physics* 6 (2013) pp. 188–197

- **Huck, C.**; Schiffels, J.; Herrera, C. N.; Schelden, M.; Selmer, T.; Poghossian, A.; Baumann, M. E. M.; Wagner, P.; Schöning, M. J.: Metabolic responses of *Escherichia coli* upon glucose pulses captured by a capacitive field-effect sensor. *Physica Status Solidi A* 210 (2013) pp. 926–931

- **Huck, C.**; Poghossian, A.; Wagner, P.; Schöning, M. J.: Combined amperometric/ field-effect sensor for the detection of dissolved hydrogen. *Sensors and Actuators B: Chemical* 187 (2013) pp. 168–173

- **Huck, C.**; Jolly, P.; Wagner, P.; Poghossian, A.; Schöning, M. J.: One-chip integrated dual amperometric/field-effect sensor for the detection of dissolved hydrogen. *Procedia Engineering* 25 (2011) pp. 1161–1164

Proceedings

- **Huck, C.**; Poghossian, A.; Buniatyan, V. V.; Wagner, P.; Schöning, M. J.: Multi-parameter detection for supporting monitoring and control of biogas

processes in agriculture. VDE Verlag GmbH (Eds.): *Sensoren und Messsysteme 2014: Beiträge der 17. ITG/GMA-Fachtagung* (2014) pp. 1–5, ISBN 9783800736225

- Buniatyan, V. V.; **Huck, C.**; Poghossian, A.; Schöning, M. J.; Rustamyan, L.; Hovnikyan, H.: Equivalent circuit and optimization of impedance characteristics of electrolyte conductivity sensor. *Proceedings of SEUA, Information, Technologies, Electronics, Radio, Engineering* V17, N1 (2014) pp. 69-77

- **Huck, C.**; Poghossian, A.; Bäcker, M.; Zander, W.; Schubert, J.; Sukoyan, L. H.; Begoyan,V.; Buniatyan, V. V.; Wagner, P.; Schöning, M. J.: Chemische Sensoren mit Bariumstrontiumtitanat als funktionale Schicht zur Multiparameterdetektion. AMA Service GmbH (Eds.): *Dresdner Beiträge zur Sensorik* (2013) pp. 368–372

- **Huck, C.**; Poghossian, A.; Wagner, P.; Schöning, M. J.: Combined amperometric/ field-effect sensor for the detection of dissolved hydrogen in biogas reactors. IMCS 2012 – The 14th Internationals Meeting on Chemical Sensors. R. Moos (Ed.) Wunstorf AMA Service GmbH (2012) pp. 1028–1031

- **Huck, C.**; Bäcker, M.; Poghossian, A.; Wagner, P.; Schöning, M. J.: Bifunktionaler Sensorchip für den Nachweis von Gelöstwasserstoff. Gerlach, G.; Schütze, A. (Eds.): *Dresdner Beiträge zur Sensorik* 43 (2011) pp. 325–328

Oral presentations

- **Huck, C.**; Poghossian, A.; Buniatyan, V. V.; Wagner, P.; Schöning, M. J.: Multiparameterbestimmung zur unterstützenden Überwachung und Steuerung von Biogasprozessen in der Landwirtschaft. Sensoren und Messsysteme 2014: Beiträge der 17. ITG/GMA Fachtagung, 04.06.2014, Nürnberg (Germany)

- **Huck, C.**; Poghossian, A.; Wagner, P.; Schöning, M. J.: Development of silicon-based sensors for biogas process monitoring. 6th Graduate Symposium FH Aachen, 20.11.2013, Aachen (Germany)

- **Huck, C.**; Bäcker, M.; Kramer, F.; Poghossian, A.; Zander, W.; Schubert, J.; Buniatyan, V. V.; Wagner, P.; Schöning, M. J.: Capacitively-coupled electrolyte-conductivity sensor based on high-k materials. Engineering of Functional Interfaces, 08.–09.07.2013, Hasselt (Belgium)

- **Huck, C.**; Herrera, C. N.; Schiffels, J.; Schelden, M.; Selmer, T.; Wagner, P.; Poghossian, A; Schöning, M. J.: Gaining insight into the metabolic activity of *Escherichia coli* using a capacitive field-effect sensor. Engineering of Functional Interfaces, 16.–17.07.2012, Zweibrücken (Germany)

- **Huck, C.**; Wagner, P.; Poghossian, A.; Schöning, M. J.: Investigation of an one-chip integrated dual amperometric/field-effect sensor for the detection of dissolved hydrogen. Engineering of Functional Interfaces, 19.–20.07.2011, Linz (Austria)

- **Huck, C.**: Entwicklung eines chipbasierten Wasserstoffsensors für die Flüssigphase. Seminarreihe des Instituts für Nano- und Biotechnologien, 25.01.2011, Jülich (Germany)

- **Huck, C.**; Poghossian, A.; Selmer, T.; Wagner, P.; Schöning, M. J.: Investigation of a dissolved hydrogen chip sensor for applications for anaerobic biogas monitoring. Engineering of Functional Interfaces, 15.–16.07.2010, Rauischholzhausen/Marburg a. d. Lahn (Germany)

Poster presentations

- Delle, L. E.; **Huck, C.**; Bäcker, Vu, X. T.; M.; Schöning, M. J.; Wagner, P.; Ingebrandt, S.; Weil, M: Reduced graphene oxide based biosensor for the impedimetric detection of histamine. Biosensors 2014, 27.–30.05.2014 Melbourne (Australia)

- **Huck, C.**; Poghossian, A.; Bäcker, M.; Zander, W.; Schubert, J.; Sukoyan, L.H.; Begoyan,V.; Buniatyan, V. V.; Wagner, P.; Schöning, M. J.: Chemische Sensoren mit Bariumstrontiumtitant als funktionale Schicht zur Multiparameterdetektion. 11. Dresdner Sensor Symposium, 09.–11.12.2013, Dresden (Germany)

- **Huck, C.**; Poghossian, A.; Wagner, P.; Schöning, M. J.: Membranbedeckter kombinierter amperometrischer feldeffektbasierter Sensor für die Detektion von Gelöstwasserstoff. 11. Dresdner Sensor Symposium, 09.–11.12.2013, Dresden (Germany)

- **Huck, C.**; Herrera, C. N.; Schiffels, J.; Schelden, M.; Selmer, T.; Poghossian, A.; Wagner, P.; Schöning, M. J.: Bestimmung methanogener Substrate zur Überwachung biologischer Prozesse im Biogasfermenter. 8. Deutsches BioSensor Symposium, 10.–13.03.2013, Wildau (Germany)

- **Huck, C.**; Poghossian, A.; Wagner, P.; Schöning, M. J.: Investigation of a bi-functional sensor chip for the detection of dissolved hydrogen in biogas reactors. 5th Graduate Symposium FH Aachen, 15.11.2012, Jülich (Germany)

- **Huck, C.**; Bäcker, M.; Poghossian, A.; Wagner, P.; Schöning, M. J.: Bifunktionaler Sensorchip für den Nachweis von Gelöstwasserstoff. 10. Dresdner Sensor Symposium, 05.–07.12.2011, Dresden (Germany)

- **Huck, C.**; Kerroumi, I.; Poghossian, A.; Wagner, P.; Schöning, M. J.: Measurement of dissolved hydrogen in a liquid-to-gas transfer setup utilizing PTFE membranes. 4th Graduate Symposium FH Aachen, 24.11.2011, Aachen (Germany)

- **Huck, C.**; Jolly, P.; Wagner, P.; Poghossian, A.; Schöning, M. J.: One-chip integrated dual amperometric/field-effect sensor for the detection of dissolved hydrogen. Eurosensors 2011, 04.–07.09.2011, Athen (Greece)

- **Huck, C.**; Poghossian, A.; Wagner, P.; Schöning, M. J.: Entwicklung eines Sensors zur Messung von gelöstem Wasserstoff für die anaerobe Biogasüberwachung. 7. Deutsches BioSensor Symposium, 03.–06.04.2011, Heilbad Heiligenstadt (Germany)

- **Huck, C.**; Poghossian, A.; Wagner, P.; Schöning, M. J.: Investigation of a dissolved H_2 sensor for applications for anaerobic biogas monitoring. 3rd Graduate Symposium FH Aachen, 04.11.2010, Jülich (Germany)

Acknowledgment

Although a 'doctorate' is the undertaking of an individual, a number of people contribute to the development of that person. I am fortunate to have had the persistent guidance and friendship of some wonderful people during my years as a doctoral student.

- Above all, I would like to express my sincere gratitude to my supervisor and co-promoter Prof. Dr. Michael J. Schöning, who gave me the opportunity to be a part of the team at the Institute of Nano- and Biotechnologies. Thank you for your support and trust, your time investing in many hours of proof-reading and last-minute corrections. Furthermore, I would like to thank you for providing the opportunity to attend national and international conferences, the freedom to constantly improve my soft skills and last but not least your extraordinary tolerance.

- In the same way, I would like to thank Prof. Dr. Patrick Wagner, who gave me the opportunity to do a PhD in cooperation with his research group and agreed to be my promoter at Hasselt University. I would like to thank you for the perusal with a vast amount of valuable remarks and suggestions, your uncomplicated and friendly manner, whenever questions and issues rose.

- I am very grateful to Prof. Dr. Arshak Poghossian for the supervision of my thesis. Your experience, broad vision and scientific energy has always been a source of inspiration for me and has greatly influenced the makeup of the research outcomes presented in this thesis. I would like to express my sincere thanks for your continuous interest, your support, numerous suggestions and proof-readings which kept me always motivated.

- My special thanks belong to Prof. Dr. Karin Coninx (Hasselt University), Prof. Dr. Carmen Bartic (K.U. Leuven), Prof. Dr. Hans-Gerd Boyen (Hasselt University), Prof. Dr. Arshak Poghossian (FH Aachen), Prof. Dr. Ronald Thoelen (Hasselt University) and Dr. Torsten Wagner (FH Aachen) for your attendance in the examination committee as well as your evaluation and constructive advice of this work.

- My gratitude is also extended to Prof. Vahe V. Buniatyan. Thank you for sharing your knowledge, experience and for great discussions. It was a pleasure for me to work with you. Furthermore, I thank Dr. Jürgen Schubert and Willi Zander of the Peter Grünberg Institute (PGI-9) at the Forschungszentrum Jülich GmbH for the preparation of numerous BST thin films and RBS analyses. My sincere thanks go to Prof. Dr. Jan D'Haen from Hasselt University for the assistance in XRD characterization.

- Particularly, I am grateful for the valuable help and collaboration of Prof. Dr. Thorsten Selmer, Dr. Johannes Schiffels and Maximilian Schelden with the cultivation of *E. coli*. Special thanks to all members of the Institute NOWUM-energy, in particular to Katharina Kasper and Marcus Dahmen, for their willingness to answer all my questions concerning the biogas process and for providing digestate from their laboratory-scale reactors.

- I am further deeply grateful to Dr. Jens Zosel, Prof. Dr. Claus Schierbaum, Prof. Dr. Werner Moritz and Prof. Dr. Claus-Dieter Kohl who provided me with useful information concerning gas-analyzing systems at the beginning of my PhD time.

- Moreover, I would like to thank Alfred Steffen representative for the whole clean-room team of the Peter Grünberg Institute (PGI-8) at Forschungszentrum Jülich GmbH for their excellent work and support. In particular, I would like to thank Hans Peter Bochem and Dr. Elmar Neumann for performing several SEM characterizations.

- I take this as an opportunity to thank the people from the mechanical workshop of FH Aachen, especially Willi Ziesmann, Walburga Hüllenkremer, Hans-Michael Bergrath and Hartmut Berner, for their uncomplicated way, fast processing of orders, maintenance and repairs of numerous measuring cells. My thanks are extended to Prof. Dr. Hans-Josef Ackermann and Heinrich-Gerd Römer for supplying me with electronic parts.

- Moreover, I like to thank Dr. Bart van Grinsven, Dr. Marloes Peeters, Dr. Kasper Eersels, Andreas Gaulke and Stijn Duchateau from Hasselt University for their support during the final stages of this thesis.

- A special thanks goes out to Jörg Hennemann and colleagues from Justus-Liebig-Universität Gießen for many helpful discussions, nice evenings in Aachen and various conferences.

- I had the pleasure to work with four students who contributed to this work in the context of their research projects. In particular, I would like to thank Cony N. Herrera, Iman Kerroumi, Shampali Chaudhuri and Pawan Jolly. Most of the results presented here would not have been possible without your efforts.

- I would like to show my greatest appreciation to all my colleagues at the INB, in particular to Dr. Elke Börmann-El-Kholy, Dr. Torsten Wagner, Dr. Shoko Takenaga, Dr. Chunsheng Wu and our lab engineers David Rolka, Heiko Iken, Stefan Beging, Marcel Leinhos and Benno Schneider. Special thanks to Heiko for assistance with chip fabrication and to David for all kind of issues. I received generous support from all of you in the daily (lab) routine. Furthermore, I would like to express my appreciation to all other students partaking and contributing to the relaxed atmosphere in the lab - Special thanks to Christoph Krumbe, Lotta Delle, Friederike Kramer and Max Krischer.

- I am deeply grateful to all former and present fellow PhD students at the INB: Dr. Monika Blank, Dr. Maryam Weil, Dr. Matthias Bäcker, Dr. Patrick Kirchner, Dr. Steffen Reisert, Dr. Frederik Werner, Sebastian Schusser, Jan Oberländer, Lars Breuer, Thomas Bronder, Johanna Pilas and Denise Molinnus. First and foremost to Matthias - You helped me during my research work in so many ways, that I cannot begin to thank you enough. You supported me in times of severe stress, tolerated my idiosyncrasies and always brought a frequent smile to my face. To Patrick - Thanks for initiating so many events such as sailing trips, tennis and barbecue. You are a cheerful person which makes life happy. To Steffen - Thank you for having coffee together and your even-tempered nature. To Frederik - I am thankful for helping me with LaTeX in the last stages of my PhD and your immense willingness to answer all my questions concerning the BioLAPS project. To Sebastian - You are an incredibly sincere and empathetic person. Your thirst to solve problems and your meticulous manner to study, prove or organize things is amazing. Thanks for supporting me when the mood was down. To Jan - I could always rely on you. Thank you. To Lars - Thanks for sharing your coruscating humor with us. To Thomas - You reminded me that life does not have to be so serious and that there are tons of interesting things to do with our time. To Johanna - Thank you for being a pleasant officemate lately. Thank you for chocolate, "Capri Sonne", words of encouragement and direction. To Denise - I enjoyed our chats. I truly missed these in the past years. It was a pleasure to work with all of you. You brought fun to the work environment through events, sports and joking around. Thank you for being my colleagues, but most of all for becoming my friends.

- The present thesis would not have been possible without financial support. Hence, I would like to express my gratitude to the Federal Ministry of Education and Research (BMBF) for financial support of the project "EMSiG". Moreover, I take this opportunity to thank Andrea Stühn representative for the "Gleichstellungskommission" of FH Aachen for the PhD scholarship.

- Last but not least, I would like to thank my family and friends not namely mentioned here for their friendship, love, encouragement and support throughout the years.

Each of you contributed to this work in your own way. Thank you!